Sonosensitive emulsions for therapeutic applications

Chloë Thimonier

Chloë Thimonier. Sonosensitive emulsions for therapeutic applications. Human health and pathology. Université Paris Cité, 2022. English. NNT : 2022UNIP7247 . tel-04421301v2

HAL Id: tel-04421301
https://theses.hal.science/tel-04421301v2

Submitted on 27 Jan 2024

Université Paris Cité

Ecole doctorale 474 Frontières de l'Innovation en Recherche et Education

Laboratoire de Physique de l'Ecole Normale Supérieure

&

Laboratoire d'Imagerie Biomédicale de Sorbonne Université

Sonosentive emulsions for therapeutic applications

Par Chloë Thimonier

Thèse de doctorat de Technologies d'Application Médicale, Diagnostiques, Thérapies et Santé Publique

Dirigée par Nicolas Taulier Et Christophe Tribet

Présentée et soutenue publiquement le 22 septembre 2022

Devant un jury composé de :

Anne-Virginie Salsac, Directrice de Recherche, UTC Compiègne	Présidente du Jury
Laurence Navailles, Directrice de Recherche, Université de Bordeaux	Rapporteur
Claude Inserra, Maître de Conférence, Université Claude Bernard Lyon 1	Rapporteur
Jacques Fattaccioli, Maître de Conférence, Sorbonne Université	Examinateur

Myriam Reffay-Beugnon, Maître de Conférence, Université Paris Cité	Examinatrice
Nicolas Taulier, Directeur de Recherche, Sorbonne Université	Directeur de Thèse
Christophe Tribet, Directeur de Recherche, Ecole Normale Supérieure	Directeur de Thèse
Wladimir Ubrach, Professeur Emérite, Ecole Normale Supérieure	Membre Invité

À Paul, sans qui ces années de thèse n'auraient pas eu le même goût.

Abstract

Sonosensitive emulsions for therapeutic applications

Current treatments for diseases such as cancer, neurodegenerative disorders or inflammation often come with side effects. This is because when a drug is administered systemically, it is free to interact with any physiological components in its path, including cells, hormones, or enzymes necessary for the body to function properly. For example, chemotherapy inhibits the proliferation of all cells, which can lead to hair loss, infertility, myelosuppression or even cause other types of cancer. To avoid such effects, one solution is to have the drug act selectively on a target site. To do this, the drug can be encapsulated in an object that will be brought to the site of interest, to release the drug only there. This delivery system serves to increase the bioavailability, efficacy and safety of a drug. The release can be triggered using an external stimulus such as ultrasound. In this context, emulsions have been produced to serve as drug carriers that can be destabilized in a controlled manner using an acoustic stimulus. Perfluorocarbon (PFC) oil emulsions have the ability to undergo a phase change from liquid droplets to gas bubbles, triggered by an acoustic stimulus above a pressure threshold. The mechanism is called acoustic droplet vaporization (ADV) and is thought to occur by superharmonic focusing of the acoustic wave inside the droplet, creating a homogeneous nucleation event. Additionally, ADV is believed to be required to release the molecules from the PFC droplets to achieve drug release. In this thesis, we have produced monodisperse emulsion systems that are produced in microfluidic devices and contain either a PFC core or a water core surrounded by a PFC shell. We demonstrate evidence of heterogeneous nucleation at the interface of the two types of PFC droplets as the mechanism of ADV. Additionally, we show that acoustically triggered release of molecules from such systems can occur by diffusion at pressures below the ADV threshold.

Overall, the three submitted papers demonstrate the possibility of using these emulsion systems for focused ultrasound-controlled delivery of hydrophilic and hydrophobic molecules without vaporization or cavitation, thus without risk of content or tissue degradation in biomedical applications.

Keywords: Emulsions, perfluorocarbon, microfluidic, acoustic, drug delivery

Résumé

Emulsions sonosensibles pour applications thérapeutiques

Les traitements actuels de maladies telles que le cancer, les troubles neurodégénératifs ou l'inflammation s'accompagnent souvent d'effets secondaires. Cela est dû au fait que lorsqu'un médicament est administré par voie systémique, il est libre d'interagir avec tous les composants physiologiques sur son chemin, y compris les cellules, les hormones ou les enzymes nécessaires au bon fonctionnement de l'organisme. Par exemple, la chimiothérapie entrave la prolifération de toutes les cellules, ce qui peut entraîner la chute des cheveux, l'infertilité, la myélosuppression ou même provoquer d'autres types de cancer. Pour éviter de tels effets, une solution consiste à faire agir le médicament de manière sélective sur un site cible. Pour ce faire, le médicament peut être encapsulé dans un objet qui sera amené au site d'intérêt, pour ne libérer le médicament qu'à cet endroit. Ce système d'administration sert à augmenter la biodisponibilité, l'efficacité et l'innocuité d'un médicament. La libération du médicament peut être déclenchée à l'aide d'un stimulus externe tel que les ultrasons. Dans ce contexte, des émulsions ont été produites pour servir de vecteurs de médicaments pouvant être déstabilisés de manière contrôlée à l'aide d'un stimulus acoustique. Les émulsions d'huile de perfluorocarbone (PFC) ont la capacité de subir un changement de phase de gouttelettes liquides en bulles de gaz, déclenché par un stimulus acoustique au-dessus d'un seuil de pression. Le mécanisme est appelé vaporisation de gouttelettes acoustiques (ADV) et on pense qu'il se produit par une focalisation superharmonique de l'onde acoustique à l'intérieur de la gouttelette, créant ainsi un événement de nucléation homogène. En outre, on pense que l'ADV est nécessaire pour libérer les molécules des gouttelettes de PFC afin d'obtenir la libération du médicament. Dans cette thèse, nous avons produit des systèmes d'émulsions monodisperses qui sont produits dans des dispositifs microfluidiques et contiennent soit un noyau PFC, soit un noyau d'eau entouré d'une coque PFC. Nous démontrons des preuves de nucléation hétérogène, à l'interface des deux types de gouttelettes de PFC comme mécanisme de l'ADV. De plus, nous montrons que la libération déclenchée acoustiquement de molécules à partir de tels systèmes peut se produire par une diffusion à une pression inférieure au seuil d'ADV.

Dans l'ensemble, les trois articles soumis démontrent la possibilité d'utiliser ces systèmes d'émulsion pour la délivrance contrôlée par ultrasons focalisés, de molécules hydrophiles et hydrophobes, sans vaporisation ni cavitation, donc sans risque de dégradation du contenu ou des tissus environnants dans les applications biomédicales.

Mots-clés: Emulsions, perfluorocarbone, microfluidique, acoustique, relargage

Remerciements

Je tiens tout d'abord à remercier les membres du jury, Anne-Virginie Salsac, pour avoir accepté de présider mon jury, Claude Inserra et Laurence Navailles pour avoir accepté de rapporter ce travail, ainsi que Jacques Fattaccioli et Myriam Reffay pour avoir lu en tant qu'examinateurs.
Je remercie tous les membres du Laboratoire de Physique de l'ENS, ainsi que tous les membres du Laboratoire d'Imagerie Biomédicale pour m'avoir accueillie pendant ces années dans des environements agréables et scientifiquement si riches.
Je souhaite remercier mon directeur de thèse, Nicolas Taulier, pour les nombreuses discussions, ainsi que pour sa patience, sa bonne humeur et son optimisme, même pendant les moments de flou. Je tiens ensuite à remercier mon co-directeur de thèse, Christophe Tribet, pour sa confiance et son soutien scientifique. Je remercie chaleureusement Wladimir Urbach, directeur de thèse officieux, pour son humour sans faille, les innombrables discussions, les cafés, et pour m'avoir autant aidé pendant toutes les périodes de ma thèse, calmes (il n'y en a pas eu beaucoup) et moins calmes (il y en a eu plus). Je remercie également Rachid Thiam et Charles Baroud pour avoir suivi mon travail et m'avoir conseillé tout au long de cette thèse.
Je tiens ensuite à remercier deux Vincent. Le premier est Vincent Faugeras, pour les discussions footballistiques et culinaires, souvent autour d'une bière (préférablement agrémentée de Picon), et pour avoir accepté mon obsession du Super Moscato Show. Ce qui m'amène à remercier Vincent Moscato pour avoir égayé les deux années de COVID passées à maniper isolée au premier sous sol du département de physique de l'ENS ou au dernier étage du LIB. Je tiens également à remercier Alexandre Santinho pour les débriefs matinaux post-ligue des champions, et pour les verres post-labo. Je tiens particulièrement à remercier Mathis Martin pour son aide précieuse pendant ces derniers mois de thèse. Je remercie aussi tous les autres doctorants que j'ai cotoyé, précédents et actuels: Yaëlle Dubois, Maxime Charpentier, Calvin Duménil, Nathan Fournier, Delphine Mion, bon courage pour la fin de vos thèses.
Merci à Julie, Fanny, Izel et Laurence, pour les rires et moments de détentes nécessaires durant ces années.
Je tiens à remercier mes parents et Elliott pour leur soutien inconditionnel.
Enfin, je remercie Paul et Salem, encore et toujours. Agus a-nis, Alba!

Contents

List of Figures

List of Tables

Abbreviations

ADV : Acoustic Droplet Vaporization
ATBC : Tributyl O-acetylcitrate
AuNP : Gold nanoparticle
CMC : Critical micellar concentration
DLS : Dynamic light scattering
DMEM : Dulbecco/Vogt modified Eagle's minimal essential medium
EIP : Emulsion inversion point
EPR : Enhanced permeability and retention
FDA : Food and drug administration
F_8TAC_{13} : F-TAC surfactant
$H_{12}TAC_7$: H-TAC surfactant
HIFU : High intensity focused ultrasound
HPH : High pressure homogenization
MI : Mechanical index
ND : Nanodroplet
NP : Nanoparticle
OOC : Organ-on-chip
O / W : Oil-in-water
O / W / O : Oil-in-water-in-Oil
PEG : Polyethylene glycol
PDI : Polydispersity Index
PDMS : Polydimetylsiloxane PFC : Perfluorocarbon
PFC / W : Perfluorocarbon-in-water
PFH : Perfluorohexane
PFH / W : Perfluorohexane-in-water
PFOB : Perfluorooctyl bromide
PFP : Perfluoropentane
PIT : Phase inversion temperature
PLGA : Poly(lactic-co-glycolic acid)
PRF : Pulse repetition frequency
US : Ultrasound

W / O : Water-in-oil
W / O / W : Water-in-oil-in-water
W / PFH : Water-in-perfluorohexane

Chapter 1

Introduction

Current treatments for diseases such as cancer, neurodegenerative disorders or inflammation are often accompanied by side effects. This is due to the fact that when a drug is administered systemically, it is free to interact with every physiological component on its path, including cells, hormones, or enzymes required for healthy functioning of the body. For example, chemotherapy hinders the proliferation of all cells, which can cause hair loss, infertility, myelosupression or can even cause other types of cancer [3, 4]. To avoid such effects, one way is to make the drug act selectively at a target site. To do this, the drug can be trapped in an object that will be brought to the site of interest, to release the drug only at this location. This delivery system serves to increase the bioavailability, efficacy and safety of a drug [5].

A widely researched type of stimulus used to induce drug release is ultrasound. Indeed, particles in the form of emulsions, made of perfluorocarbon oils can be vaporized with ultrasound, through a mechanism that is poorly understood.

The main goal of this thesis was to understand the mechanism of ultrasound-triggered vaporization of perfluorocarbon emulsion droplets, as a strategy to locally induce the delivery of a drug for biomedical applications.

1.1 Targeted drug delivery

The concept of targeted drug delivery originates from Paul Erlich's idea of the "magic bullet" which dates back to the 1950's, and yet only a small number of such systems have been commercialized since then [6].

When a drug enters the body, orally, through injection or through other modes of administration, it faces different threats of degradation. Various physical and biochemical barriers exist in the body which hinder the arrival

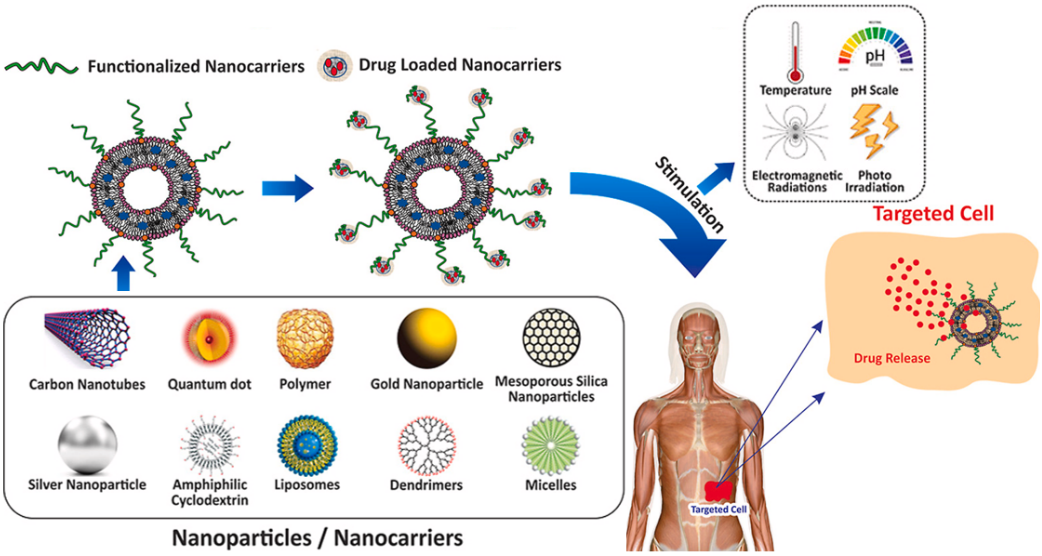

Figure 1.1.1 – *Scheme of commonly used targeted drug delivery carriers and stimuli used to destabilize them ([7]).*

of the drug to a target site. Among these challenges, there is the low pH of the stomach and various gastric enzymes, microvilli of the intestine, drug degradation in the liver and spleen, among others. The drug therefore has to be protected from these barriers. Multiple ways of protecting a drug have been studied in the form of various objects, shells and capsules, usually made of lipids, oils, or polymers [8, 6].

However, there have been major issues in the development of these carriers, due to the strict requirements regarding the material, size and properties of objects that can circulate in the body without deleterious or aspecific interactions.

1.1.1 Carriers

A successful drug vector is biocompatible, provides an environment in which the drug can be solubilized, should circulate long enough to deliver the drug but should not stay in the body afterwards, should overcome physical and physiological barriers, and be able to exhibit a controlled spatio-temporal release mechanism. The size and charge of particles have to be taken into consideration during formulation because they will affect the circulation time in the body and the biodistribution. Various mechanisms can cause the uptake of particles, depending on their size. Nanoparticles (NPs) that are smaller than 10 nm will be taken up by the kidneys or opsonized, which

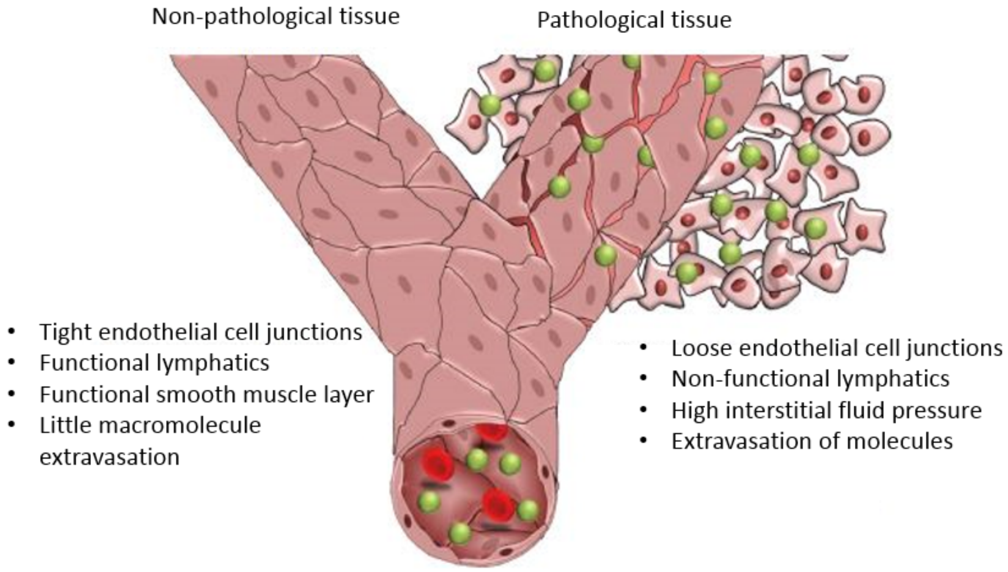

Figure 1.1.2 – *Scheme of EPR effect in vasculature of solid tumor (copied from Greish et al 2014) [9]*

is a process through which proteins (opsonins) will tag a foreign object, so that it can be eliminated by phagocytes [10, 11]. NPs that are smaller than 50 nm can go through the endothelium of the liver and be trapped. The protein clathrin will cause the endocytosis of 120-150 nm NPs, while caveolae, which are folds in the plasma membrane, will cause the endocytosis of 50-120 nm NPs. Particles that are a few 100's of nm cannot circulate for long periods of time as they will be taken up by macrophages; also, they cannot go through the pores of blood vessels to reach some target sites. The ideal size of a NP depends on the application. For example, in the case of cancer the consensus seems to be that the NPs size should range from 70-200 nm to reduce the clearance rate while taking advantage of the enhanced permeability and retention effect [12, 13] (fig.1.1.2). Cationic particles have higher opsonization rates and therefore a lower circulation time than neutral or anionic particles. In such cases, surface modification can be used to lower the visibility of the vectors by the immune system [11]. An example of surface modification is pegylation. It is the covalent bonding of FDA approved polymer, polyethylene glycol (PEG), to the surface of particles [14]. PEG is biocompatible, inert, and highly soluble in water, so the pegylated particle is more soluble in blood. This surface modification protects the particle from clearance by the kidneys because the molecular weight and size of the particle is increased [15]. It also provides protection from degradation enzymes and proteins through steric hindrance. Overall, pegylation has been shown to increase the circulation time and half-life of particles. However, a major disadvantage is hypersensitivity reactions, often caused by repeated exposure to PEG's. They are present in foods, cosmetics, and everyday products, which causes frequent exposure and increases the presence of anti-PEG antibodies [16]. Associated with this is a higher clearance rate of particles in patients with anti-PEG antibodies [17]. Also, the size increase caused by pegylation can make it difficult to stay within size requirements [16].

The way in which a specific site is targeted can be either active or passive. Active targeting consists in tagging the drug carrier with a ligand, a protein or an antibody that will cause binding to and uptake by the targeted cells. Passive targeting consists in taking advantage of the local environment to cause the local accumulation of particles. In the case of tumor cells, the tumor microenvironment properties are used to induce the accumulation. Indeed, the tumor microenvironment can be characterised by the Enhanced Permeability and Retention (EPR) effect. The vasculature surrounding solid tumors is leaky, due to the increased spaces between the cells composing the blood vessels of this area. Particles that are smaller than these pores can therefore passively diffuse into the tumor microenvironment and accumulate locally (fig. 1.1.2). Once the particles have accumulated at the target site, an external stimulus can be applied (e.g. light, ultrasound) to trigger the release of their content.

The first therapeutic NP dates back to the 50's. It was a drug-polymer conjugate developed by Horst Jatzkewitz, who demonstrated that the attachment of poly(vinyl-pyrrolidone) to mescaline (a psychoactive drug) increased its circulation time in the body [19, 20, 16, 10]. In the 60's, the idea arose of surrounding the drug with a hydophobic capsule, to create a barrier from the blood. Liposomes were formulated and these types of drug delivery systems have been the most widely studied nanocarriers. Since then, in parallel to new drug development, the goal has been to use already available drugs and deliver them in a more efficient way through controlled targeting and achieve precise spatio-temporal release. Many types of vectors have been studied since that time, including micelles, polymeric NPs, nanoshells, dendrimers, silica-based NPs, and more (fig. 1.1.1).

1.1.2 Liposomes

Liposomes are vesicles formed by a phospholipid bilayer and an aqueous core. They can encapsulate actives that are hydrophobic (in their lipid layer) or hydrophilic (in the aqueous cavity) [21, 22]. The first successful liposomal

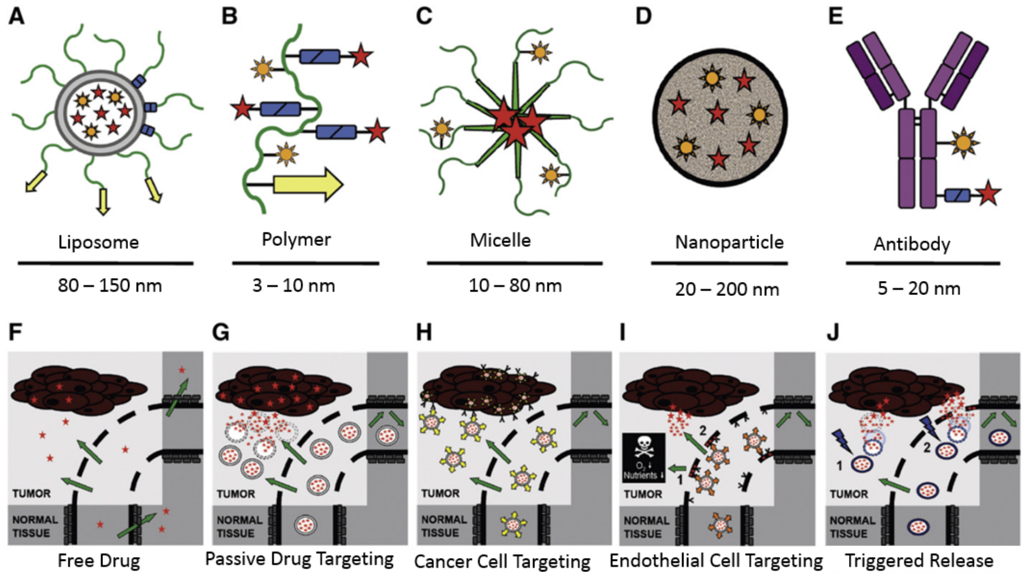

Figure 1.1.3 – *Scheme of common drug delivery systems and targeting strategies. A–E: Drug targeting systems. Liposomes and liposomal bilayers are depicted in gray, polymers and polymer-coatings in green, targeting ligands in yellow (arrows), antibodies and antibody fragments in purple, imaging agents to monitor biodistribution and target site accumulation in orange (suns), and conjugated or entrapped (chemo-) therapeutic agents in red (stars). F–J: Drug targeting strategies. F: Upon the i.v. injection of a low-molecular-weight chemotherapeutic agent, which is often rapidly cleared from the blood, only low levels of the drug accumulate in tumors and in tumor cells, while its localization to normal organs and tissues can be relatively high. G: Upon the implementation of a passively targeted drug delivery system, by means of the EPR effect, the accumulation of the active agent in tumors and in tumor cells can be increased substantially, while its localization to healthy tissues can be attenuated. H: Active drug targeting to internalization-prone cell surface receptors (over-) expressed by cancer cells generally intends to improve the cellular uptake of nanomedicine formulations, and is particularly useful for the intracellular delivery of otherwise poorly internalized macromolecular drugs, such as DNA. I: Active drug targeting to receptors (over-) expressed by angiogenic endothelial cells on the one hand aims to increase drug delivery to tumor endothelium, thereby eradicating tumor blood vessels and depriving tumor cells of oxygen and nutrients (I-1). On the other hand, reasoning that tumor endothelial cells are continuously exposed to long-circulating nanomedicines, endothelial cell targeting can likely also be employed to improve the overal accumulation of chemotherapeutic agents in tumors (I-2). J: Stimuli-sensitive nanomedicines, can be activated (i.e. induced to release their contents) by externally applied physical triggers, like hyperthermia, ultrasound, magnetic fields and light. This can be done either after accumulation at the target site (J-1), or while circulating in the tumor vasculature (J-2).(copied from Lammers et al 2021) [18]*

system, and the first drug delivery system to be approved by the FDA is Doxil, which is encapsulated doxorubicin [23]. This chemotherapeutic agent in its non-encapsulated form has a high cardiotoxicity, which causes cardiomyopathy. This major side effect was considerably reduced with Doxil. The main issues with these vehicles are that they are leaky, and therefore some of the drug is lost before it even reaches the target site [8]. Also, only a small quantity of hydrophobic drug can be carried in the bilayer. Finally, they usually cannot evade the immune system without surface modification, which is challenging to achieve [24].

1.1.3 Micelles

Micelles are spherical aggregates of amphiphilic molecules. The hydrophobic tails are organized toward the center of the carrier, while the hydrophilic heads turn to the outer aqueous environment. Micelles therefore encapsulate hydrophobic actives. They can be formed using surfactants, which spontaneously assemble above a critical concentration (Critical Micellar Concentration, or CMC). Polymeric micelles can be formed in the same way, but with polymers. They tend to be more stable than surfactant micelles and form at a lower CMC. Micelles generally range from 10-100 nm in diameter, which makes them good candidates to take advantage of the EPR effect. They need to be pegylated to render them stealth to increase their circulation time. Kataoka et al successfully loaded doxorubicin into poly(ethylene glycol)-poly(beta-benzyl-L-aspartate) block copolymer (PEG-PBLA) based micelles [25]. The circulation time was increased (by a factor 5) due to the steric repulsion induced by the hydrophilic heads conformation. Some micelles are currently undergoing clinical trials for use in cancer therapy [26]. The main disadvantages are their low stability *in vivo*, their limited loading capacity [27] and their ability to only encapsulate hydrophobic compounds.

1.1.4 Polymeric nanoparticles

Polymeric NPs are made of assemblies of responsive polymers, and molecules can be trapped in their core, matrix or bind on their surface, depending on their shape [28]. Examples of polymeric NPs include polymersomes, polymeric micelles and dendrimers. Their sizes range between 5 nm and 1 µm. The polymers used to make these particles can be natural or synthetic. Polymersomes are made of amphiphilic block copolymers surrounding an aqueous core. They are similar in structure to liposomes but are more stable and less leaky. Dendrimers are assemblies of hyperbranched polymers with functional groups on the outside, which allow the binding of molecules (e.g. contrast agents), and cavities in the interior in which drugs can be carried [29]. Some dendrimers are currently undergoing clinical trials, but none have been clinically approved so far [30, 31].

Polymeric NPs are interesting candidates for drug delivery as they can be triggered using various stimuli (such as heat or light), they are water soluble and stable. The major downside is that they can leave residual material (e.g. aggregates of monomers) in the body which can have undesirable effects (e.g. increase local pH, induce inflammation) [8]. Due to this, only a few have been clinically approved, but an increasing number have started to undergo clinical trials in the last few years (e.g. RadProtect, Genexol-PM, AZD2811) [32].

1.2 Emulsions

Emulsions are multiple-phase systems between immiscible fluids. One of the phases is dispersed in the other in the form of droplets (fig.1.2.1). The internal phase is the dispersed phase, and the outer phase is the continuous phase. Emulsions made of two phases, such as Oil-in-Water (O/W) or Water-in-Oil (W/O), are called single emulsions. Emulsions made of three phase, such as Water-in-Oil-in-Water (W/O/W) or Oil-in-Water-in-Oil (O/W/O), are termed double emulsions. They consist of a core inside a shell, surrounded by the bulk [33]. They are attractive drug delivery systems due to their versatility. Depending on the composition of the core, a hydrophilic or hydrophobic payload can be encapsulated. However, these systems are thermodynamically unstable and need to be stabilized by surfactants.

1.3 Stabilization of emulsions

Emulsions are unstable and can be further destabilized through different ageing mechanisms. Coalescence occurs when two droplets merge to reduce the interfacial energy. Creaming occurs when the density of the droplets is lower than the density of the bulk. Sedimentation is the opposite, it occurs when the density of the droplets is higher than the density of the bulk. Flocculation is a process through which droplets form aggregates (flocks) causing them to either sediment or cream faster. Ostwald ripening is a diffusion phenomenon which occurs between droplets of different sizes in solution [34]. Larger droplets are more energetically favored than smaller droplets. The solubility of the dispersed phase of an emulsion droplet into the bulk increases with decreasing droplet radius. Ostwald ripening is the process through which the dispersed phase of smaller droplets in an emulsion solubilizes into

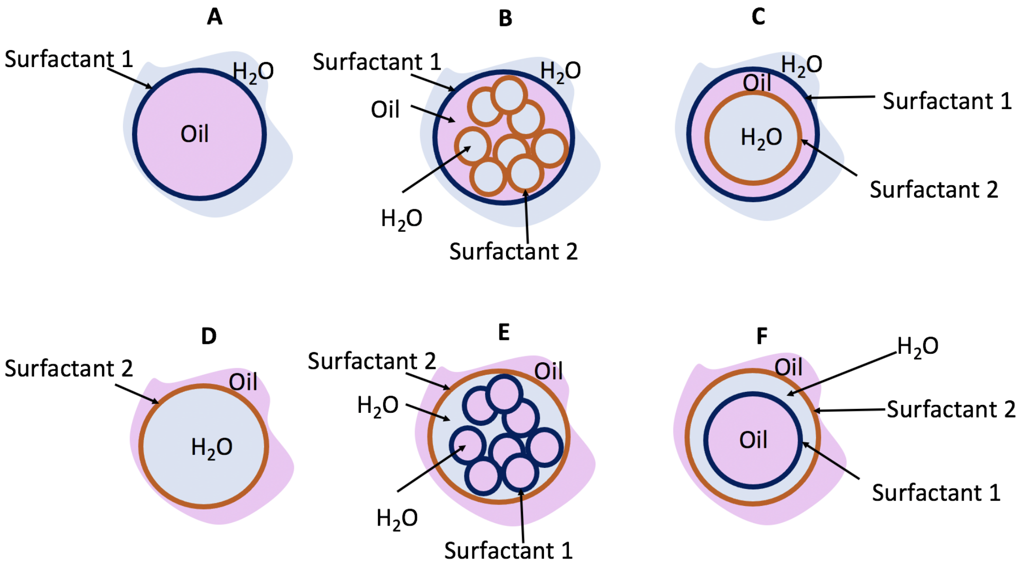

Figure 1.2.1 – *Types of emulsions: A: Single emulsion of Oil-in-Water (O/W) stabilized by surfactant 1. B: Double emulsion of Water-in-Oil-in-Water (W/O/W), with multiple water droplets stabilized by surfactant 2 and the larger oil droplet stabilized by surfactant 1. C: Double emulsion of Water-in-Oil-in-Water (W/O/W), with a single water droplet stabilized by surfactant 2 and the larger oil droplet stabilized by surfactant 1. D: Single emulsion of Water-in-Oil (W/O) stabilized by surfactant 2. E: Double emulsion of Oil-in-Water-in-Oil (O/W/O), with multiple oil droplets stabilized by surfactant 1 and the larger water droplet stabilized by surfactant 2. F: Double emulsion of Oil-in-Water-in-Oil (O/W/O), with a single oil droplet stabilized by surfactant 1 and the larger water droplet stabilized by surfactant 2.*

the bulk, and the molecules redeposit onto the larger droplets, to minimize surface to area ratio and create a more thermodynamically stable system. Through this mechanism, the diameter of the larger droplets increases while the diameter of the smaller droplets decreases, resulting in demixing [35].

1.3.1 Surfactants

To avoid, or at least slow down demixing mechanisms, the stabilization of emulsions requires the use of surfactants. These molecules lower the surface tension energy between the dispersed phase and the continuous phase. The system therefore no longer tries to minimize Gibb's free energy through these demixing mechanisms [18]. Surfactants are amphiphilic compounds, with a hydrophilic head and hydrophobic tail. Due to this, they preferentially arrange at the interface between a hydrophobic and a hydrophilic phase. In a case where there is no interface available, the surfactants will spontaneously arrange together to lower the free energy between themselves and the phase that they are in (and thus form micelles)[36].

1.4 Production of emulsions

1.4.1 Batch techniques

Since emulsions are not thermodynamically favorable, energy is required to create the dispersion of one phase in another. These techniques can be high or low energy (fig. 1.4.1), and the type of energy can vary (e.g. mechnical, sonic, electrical).

However, they lead to a wide range of droplet sizes (high polydispersity).

1.4.2 The Ouzo effect

The Ouzo effect refers to a spontaneous emulsion production mechanism which, surprisingly, does not require energy nor surfactant to obtain stable emulsion droplets [38]. It can be observed with various beverages such as Ouzo, Pastis, or Raki. It consists of a ternary system of an oil (or other solute), a solvent (e.g. alcohol) and water. First, there needs to be the formation of a primary nanoemulsion which consists of a low amount of dispersed oil in a water-miscible solvent (such as an alcohol). When water is added above a certain threshold to this emulsion, the oil droplets separate from the solvent. The end product is an O/W emulsion [23]. The sizes obtained range from 100 nm to 1 µm and the stability can last for months [38]. The size and stability of the produced emulsion can be altered by changing the relative proportions and solubilites of the three components. The fact that the Ouzo effect allows the formation of stable monodisperse (same diameter) droplets independently of the use of a surfactant or mechanical agitation [39] is not well understood.

1.4.3 Droplet microfluidics

Microfluidics is an adequate method of production when monodispersity is required. Various geometries exist, but the idea is always the same: the fluids are brought in contact inside a chip at the level of a junction (or a nozzle), where the continuous phase ”pinches” the dispersed phase to create a droplet, as seen on fig. 1.4.2 (more details will be given on droplet production in

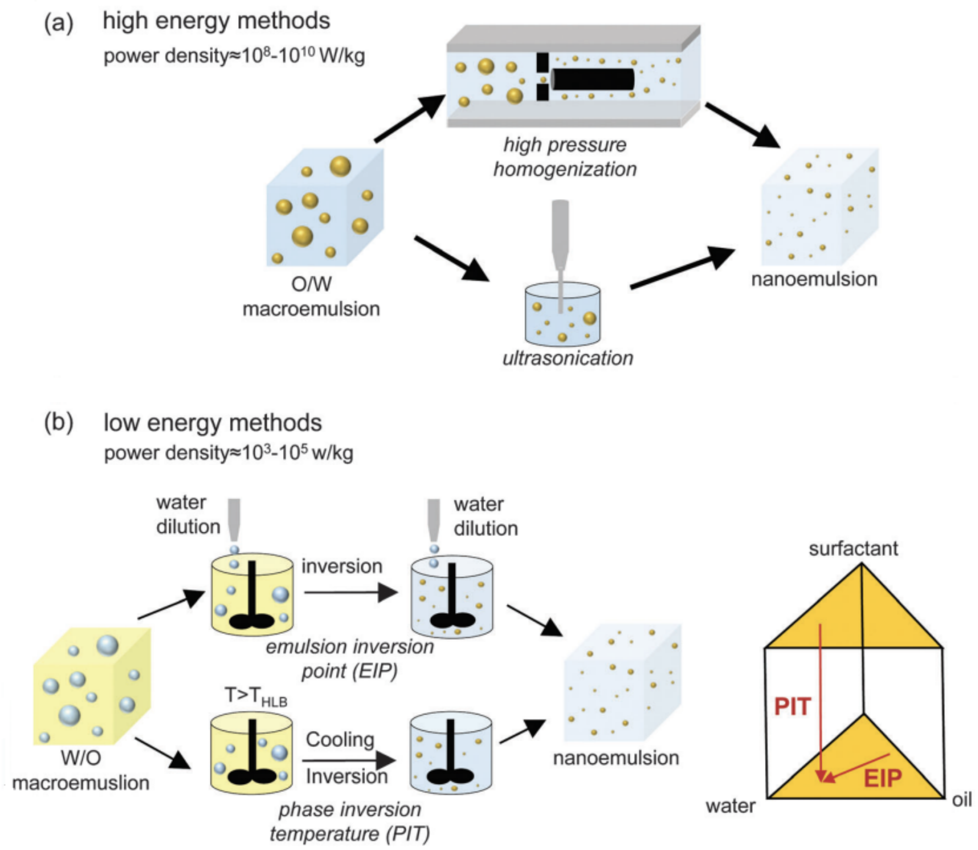

Figure 1.4.1 – *Overview of high energy and low energy methods for preparing O/W nanoemulsions. (a) High energy such as high pressure homogenization (HPH) and ultrasonication break macroemulsion drops into smaller droplets. (b) Low energy methods start with macroemulsions and break coarse emulsions into smaller droplets as they pass through a state of low interfacial tension during phase inversion. The Emulsion Inversion Point (EIP) technique induces a phase inversion by water dilution whereas the Phase Inversion Temperature (PIT) approach induces a phase inversion on cooling of the mixture [37].*

Section 2.8). In such a system, every parameter of production can be tightly regulated: the pressure at which the fluids enter the chip, the flow rates of the fluids and the geometry of the chip, thus generating highly monodisperse droplets (fig. 1.4.3). Droplet microfluidics has been used with various media, to encapsulate various actives, cells, genes or other biological material [40].

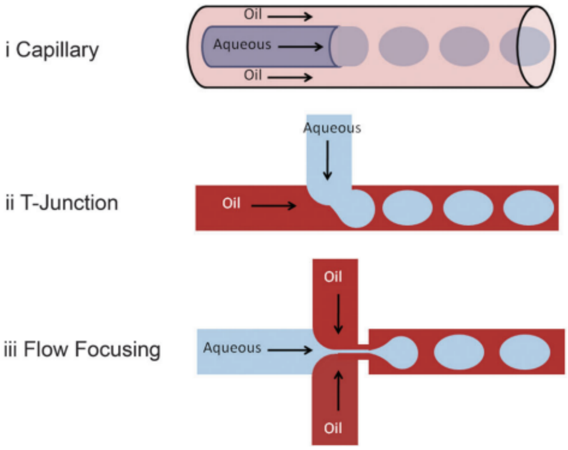

Figure 1.4.2 – *Droplet generation strategies: (i) co-flow in a capillary format; (ii) T-Junction in a planar chip format; (iii) flow focusing in a planar chip format [41].*

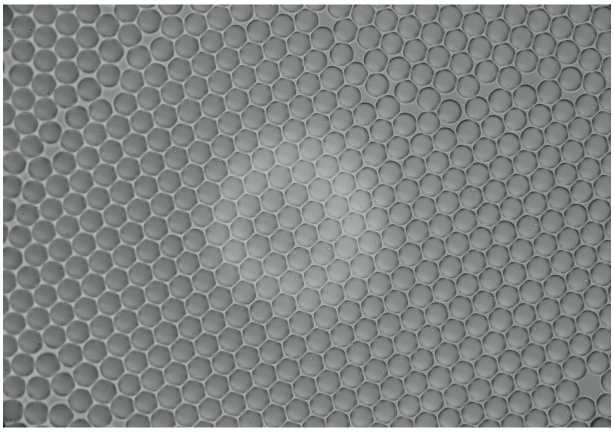

Figure 1.4.3 – *Monodisperse emulsion droplets of 20 µm diameter made in a microfluidic device (Camera Model SC1, Edgertronic, USA, microscope Leica DM IL objective x 10.*

1.5 Perfluorocarbon emulsions as drug delivery systems

Perfluorocarbon (PFC) based particles have been studied as drug delivery systems. PFC oils are inert and immiscible with most aqueous solutions and organic oils. They are clear, which allows observation of the encapsulated payload (cells or fluorescent drug for example).They are highly stable and do not undergo metabolism or enzymatic changes [42, 43]. They have high gas solubility, which makes them good candidates to encapsulate cells or biological material which requires gas exchange [44, 42]. Their oxygen and carbon dioxide carrying capacity is more than twice that of blood [45]. Most of the FDA approved PFC's are for use with lung ventilation. Due to their high density and high oxygen solubility, they can be breathed in and sediment at the bottom of lung alveoli to provide oxygen [46]. It has then been shown that they can be eliminated through exhalation or transpiration through the skin [46].

A particularly interesting feature for targeted drug delivery is that they have a phase change ability when treated with ultrasound. Indeed, liquid PFC will undergo a phase transition from a liquid droplet to a gas bubble under acoustic stimulus above a certain threshold. Once the PFC has gone from liquid to gas, the content of the particle can diffuse into its local environment. This phase change phenomenon, called Acoustic Droplet Vaporization (ADV) will be discussed in Section 1.7.

To stabilize PFC emulsions, the surfactants used are composed of a hydrophilic group on one end and a fluorophilic group on the other. Similarly to other components forming the particles, these fluorinated surfactants must be biocompatible, and they should not interact with the drug inside the droplet. However, most of the commercial surfactants available were originally developed for industrial purposes, not medical, so their biocompatibility has not been proven [47]. Another option is to stabilize them using lipids, polymers, or proteins, which have a low affinity for PFC's and therefore result in poor stabilization of the droplets. A class of surfactants, F-TAC, has been developped since the 90's at Université d'Avignon [48]. This class of surfactants is biocompatible and successfully stabilizes PFC based emulsions (more details in Sections 3.1, 3.2, and 3.3). The immiscibility of PFC's makes encapsulating various actives difficult. One option is to bond the drug to the molecule that stabilizes the interface (e.g. the hydrophobic part of a polymer). Zhong et al produced perfluoropentane (PFP) nanodroplets (NDs) stabilized by diblock co-polymers, and encapsulated various drugs of different hydrophobicities [49] by binding them to the hydrophobic block of the polymer. They found that the hydrophilic chemotherapy drug cisplatin could not be loaded in the droplets, while the loading of hydrophobic anti-hypertensives nicarpdipin and verapamil were successfully loaded. However, even the hydrophobic drugs could only be loaded at low percentages (less than 2% of the NPs weight). Currently, the only way to transport actives with nanometric PFC droplets is to trap them in the shell of the droplets. To encapsulate a large amount of actives in a PFC droplet, a hydrophobic or hydrophilic core has to be added. The encapsulation of drugs therefore requires the use of double emulsions of Water-in-PFC-in-Water (W/PFC/W), or Oil-in-PFC-in-Water (O/PFC/W). Incorporating a water or oil core into the PFC droplets cause an increase of the diameter, which reaches the micrometric range. Couture et al were able to deliver large payloads using water core PFC droplets converted into bubbles using an ultrasound clinical scanner [50].

1.6 Focused ultrasound as a stimulus for targeted delivery of molecules encapsulated in PFC droplets

Ultrasound has been widely and safely used in clinics for years [51]. It is a non-invasive external stimulus which allows for highly precise spatial (order of millimeter) and temporal control. Ultrasound consists of pressure waves with frequencies equal to or higher than 20 kHz. They can be generated by a transducer which changes a voltage from an electric source into an acoustic wave, in a medium in which the wave can propagate. These waves cannot propagate in air because the attenuation is too high. However, when an ultrasonic wave travels through an aqueous medium it can penetrate deeply into tissue. Ultrasound effects on delivery can be classified into two main categories: thermal and non-thermal.

Thermal effects consist in the associated temperature changes due to the absorption of the energy by the tissue [52]. The delivery of a drug through a thermal mechanism usually involves a thermosensitive material (e.g.polymer, protein, fluid) which will undergo a conformation-change or phase-change and allow the release of the encapsulated drug. However, there are certain limitations associated with the use of a thermal mechanism, notably that the function of cells is altered at temperatures that are higher than 37°C, and above 43°C the cells do not survive[53]. Therefore, the temperature changes cannot be more than 6 degrees (according to the FDA), and the treatment times should be short.

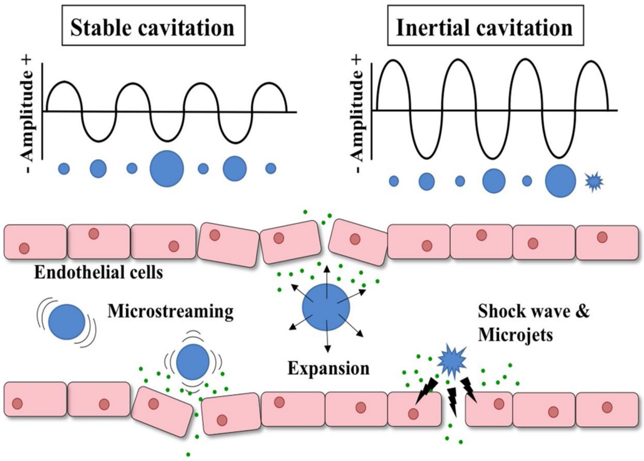

Figure 1.6.1 – *Sketch of stable and inertial cavitation showing the effects on the endothelium [55].*

Non-thermal effects consist in acoustic streaming, pressure, and the oscillation of bubbles due to the acoustic wave, among others. Bubbles can oscillate at the same frequency as the acoustic wave. They alternate between an increase and decrease in their volume. This is termed stable or non-inertial cavitation, as opposed to inertial cavitation. Stable cavitation can be used to increase the penetration of a drug in cells by opening the cell membrane [54]. Inertial cavitation occurs at higher acoustic pressures, when the oscillations of the bubbles increase and the bubbles collapse. This collapse is a violent process which induces significant pressure and temperature increase, which can cause deleterious effects to surrounding tissues and cells [54].

Using ultrasound as an external stimulus, multiple types of particles have been studied to carry and release drugs in the context of targeted and controlled drug delivery[49, 56, 50, 57, 58].

Baghbani and Mortarzadeh used stable cavitation to deliver the anticancer drug doxorubicin and the chemosentisizer curcumin from perfluorohexane (PFH) NDs, in mice [1, 59]. They showed a significant inhibition of the ovarian tumor growth on the group treated with the PFH NDs, compared to the group treated with saline (fig.1.6.2). Ultrasound combined with PFH NDs thus induced the selective death of the tumor cells.

Fabili et al encapsulated and delivered thrombin in blood *in vitro* from the aqueous core PFC double emulsion droplets by vaporizing the PFC to reduce the clotting time in canine blood [56].

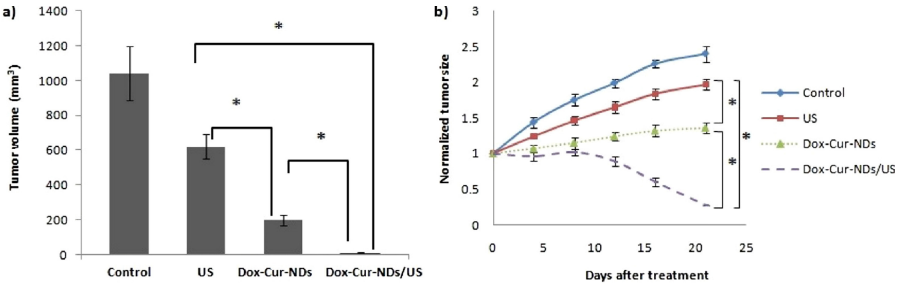

Figure 1.6.2 – *(a) Tumor volume in mice after 21 days of treatment with doxorubicin and curcumin-loaded PFH NDs destabilized by ultrasound at 28kHz. (b) Tumor growth curves of different groups of mice, treated with only ultrasound and no PFH NDs (US), mice treated with doxorubicin and curcumin-loaded PFH NDs without ultrasound (Dox-Cur-NDs), mice treated with doxorubicin and curcumin-loaded PFH NDs with ultrasound (Dox-Cur-NDs/US), and the control group[1]*

1.7 Acoustic Droplet Vaporization

The phenomenon of Acoustic Droplet Vaporization (ADV) has been studied for various biomedical applications such as imaging [60, 61, 62] and targeted drug delivery [63, 56]. It is believed that ADV is required to release the content of PFC droplets. However, the process of ADV and the parameters which affect it are still being discussed. The main study areas are

- understanding where ADV begins, or in other words where the nucleation initially occurs,
- why the ADV threshold pressure decreases with increasing droplet radius.

Both of these questions will be addressed in Section 3.1.

Li et al and Shpack et al have shown that the initial nucleation site is located inside of the droplet (homogeneous nucleation), due to a focalisation of the acoustic wave [65, 66] (fig.1.7.3). Superharmonic focalisation inside of the droplet occurs when the length of the incident acoustic wave, λ is smaller than the radius , r, of the droplet. On fig.1.7.2, we can see that a droplet of 10 µm diameter causes a focalisation of the incident wave.

It has also been shown that a second nucleation site can form following the first one [67, 68]. The droplet composition and structure have an effect on the mechanism of ADV [69]. The boiling point of the PFC oil used, will determine the pressure required to induce ADV. Recent studies show that the pressure amplitude required to induce ADV decreases with

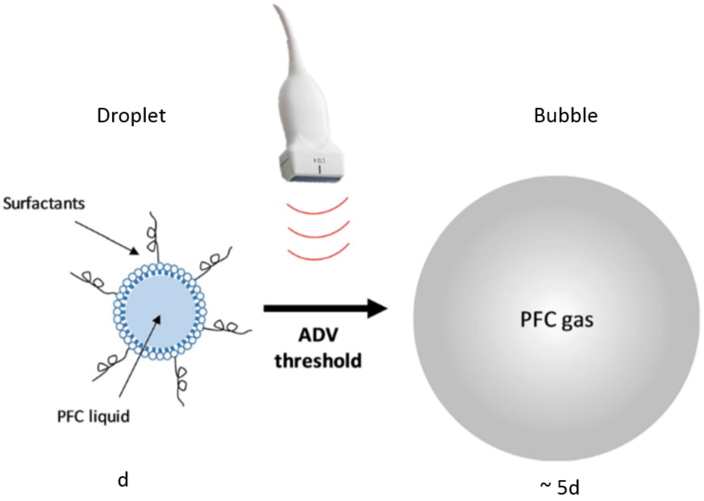

Figure 1.7.1 – *Scheme of ADV effect on PFC droplet (Melich et al) [64]. The diameter of the resulting bubble is increased by a factor 5.*

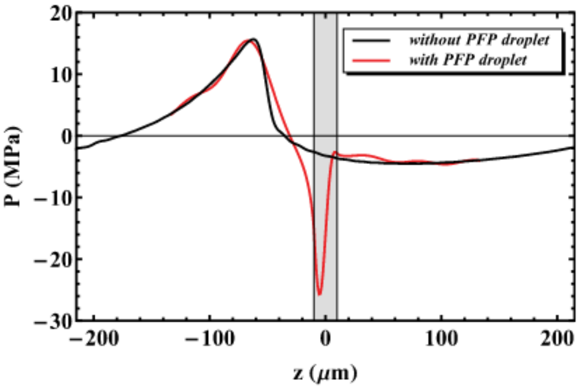

Figure 1.7.2 – *Snapshot of the superharmonic focusing effect within a spherical droplet (from Shpak et al [65]). The gray shaded region depicts the position of the droplet, R = 10 μm. The black line represents the acoustic pressure waveform on the axis of symmetry ($\theta = 0$) as a function of the z coordinate in the absence of a perfluoropentane (PFP). The red solid line is the focused pressure in the presence of the droplet. The snapshot is taken right at the moment of minimum focused pressure. The horizontal axis displays one full wavelength in the medium outside of the droplet. The focusing spot lies around z = -0.4R and the pressure is amplified 5.8 times compared with the incident acoustic pressure (-4.5 MPa).*

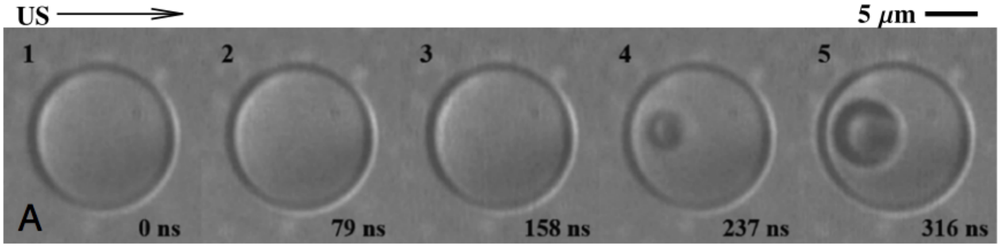

Figure 1.7.3 – *A set of consecutive images showing acoustic focalisation at -0.4R, inside of a 7.4 μm radius PFP droplet taken at a frame rate of 12.6 million frames per second. The droplet is triggered by an eightcycle, 5-MHz frequency ultrasound pulse. The nucleation is initiated between frames 3 and 4. Frames 4 and 5 show the subsequent vapor bubble growth" (copied from Shpak et al [65])*

increasing frequency [70, 71]. This is the opposite of the pattern observed for inertial cavitation (for which the pressure amplitude necessary to cavitate increases with higher frequencies)[51, 72]. The homogeneous nucleation model of ADV is valid for large droplets undergoing high frequency acoustic treatment. However, at lower frequencies, there is no longer a focalisation of the acoustic wave inside of the droplet, even for larger droplets as seen on fig. 1.7.4. Most of the studies have been done with large micrometric droplets for microscopic visualisation purposes. The location of the nucleation site in smaller droplets, in which the focalisation should not occur, has also been shown by Shpak et al. However, the reason for decreasing ADV threshold pressure with increasing droplet radius has not been explained.

Chapter 3.1 of this thesis will bring an explanation of this phenomenon, which stems from evidence of a heterogeneous nucleation.
Chapter 3.2 will demonstrate that ADV is not necessary to release molecules from PFC-based droplets.
Chapter 3.3 will show a method to produce alcohol-free monodisperse PFC nanodroplets in microfluidics using the Ouzo effect.
The next chapter will talk about the materials and methods used in this thesis to produce droplets in microfluidic devices, the acoustic experiments set ups used for ADV and release experiments, as well as the methods used for analysis.

Overall, this thesis is a study of the mechanisms involved in the release of hydrophilic and hydrophobic actives from versatile emulsion droplet systems, for use in biomedical applications.

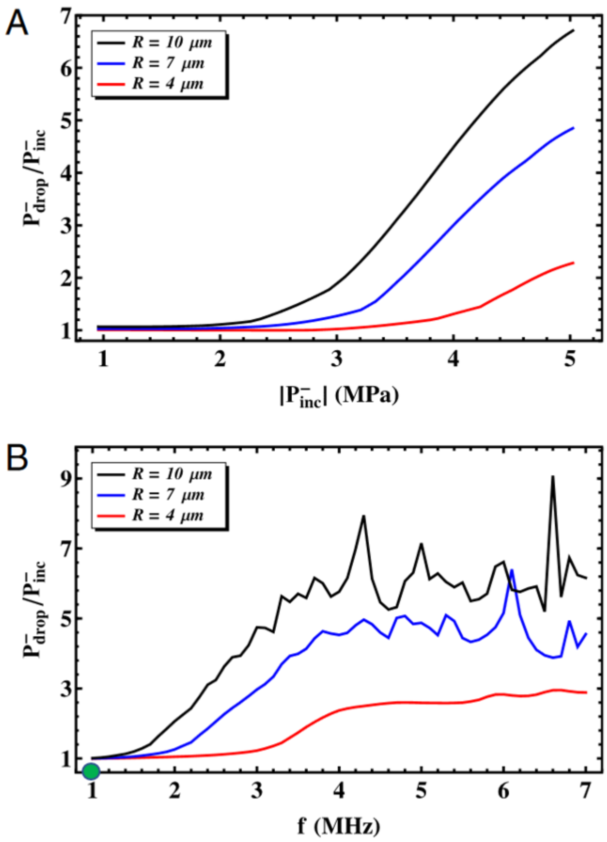

Figure 1.7.4 – *Dependence of the pressure amplification factor at the focusing spot for three microdroplet radii (A) as a function of the incident acoustic peak negative pressure* P^-_{inc} *at a driving frequency of 3.5 MHz and (B) as a function of the driving frequency* f *for a peak negative pressure of -4.5 MPa. The green dot indicates the frequency at which the experiments were done in this thesis. [65]*

Chapter 2

Materials and Methods

Perfluorohexane (PFH), perfluoropentane (PFP) and perfluorooctyl bromide (PFOB) were obtained from ABCR (Germany). Tributyl O-acetylcitrate (ATBC) was obtained from Merck. F_8TAC_{13} and $H_{12}TAC_7$ was synthesized by our collaborator Christine Contino-Pépin at Institut des Biomolécules Max Mousseron in Université d'Avignon (France). The fluorinated surfactants Krytox^{TM} 157 FSL and Zonyl FSO were purchased from Costenoble (Germany). NaCl, Nile red and sodium fluorescein were obtained from Merck. For microfluidic droplet production, the solutions are initially prepared in sterile 15 mL Falcon tubes and filtered with 0.2 µm Acrodisc filters from Pall, before transfer into 1.8 mL sterile vials (VWR, France) that are compatible with the microfluidic set-up (obtained from Fluigent, shown in Section 2.7). The SU8 Photoresist resin used to make the microfluidic wafers was purchased from Chimie Tech Services and the silicon wafers from BT Electronics. Poly(dimethylsiloxane) was obatined from Neyco. The water used is always ultra-pure water (Milli-Q IQ 7000 Type-1 water Purification System).

2.1 Droplets formulation

The oils used to produce the different droplet types are:

- Perfluoropentane (PFP),
- Perfluorohexane (PFH),
- Perfluorooctyl bromide (PFOB),
- Tributyl-o-acetylcitrate (ATBC).

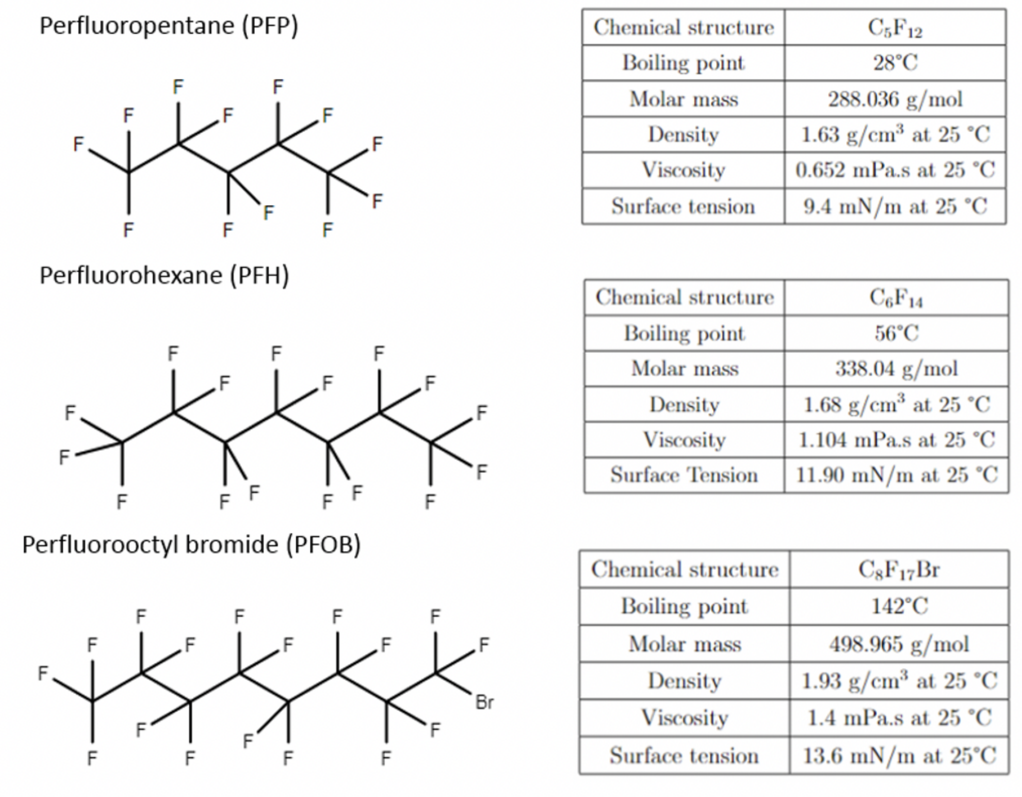

Chemical structure	C_5F_{12}
Boiling point	28°C
Molar mass	288.036 g/mol
Density	1.63 g/cm^3 at 25 °C
Viscosity	0.652 mPa.s at 25 °C
Surface tension	9.4 mN/m at 25 °C

Chemical structure	C_6F_{14}
Boiling point	56°C
Molar mass	338.04 g/mol
Density	1.68 g/cm^3 at 25 °C
Viscosity	1.104 mPa.s at 25 °C
Surface Tension	11.90 mN/m at 25 °C

Chemical structure	$C_8F_{17}Br$
Boiling point	142°C
Molar mass	498.965 g/mol
Density	1.93 g/cm^3 at 25 °C
Viscosity	1.4 mPa.s at 25 °C
Surface tension	13.6 mN/m at 25°C

Figure 2.1.1 – *Chemical structure and relevant chemical properties of PFC oils used in the formulation of emulsion droplets.*

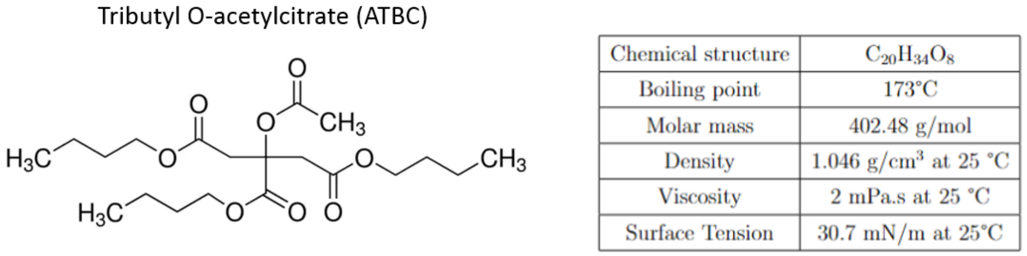

Chemical structure	$C_{20}H_{34}O_8$
Boiling point	173°C
Molar mass	402.48 g/mol
Density	1.046 g/cm^3 at 25 °C
Viscosity	2 mPa.s at 25 °C
Surface Tension	30.7 mN/m at 25°C

Figure 2.1.2 – *Chemical structure and relevant chemical properties of ATBC oil.*

Their structures and relevant properties are shown in fig.2.1.1 and 2.1.2. The surfactants used are the following:

- F_8TAC_{13}, a biocompatible fluorinated surfactant [48, 47] which stabilizes PFC/W interfaces. It is made by Christine Contino-Pépin and Stéphane Desgranges at Université d'Avignon (France). Its molecular weight is 1680 g/mol and its CMC is 0.017 mM.
- $H_{12}TAC_7$, a biocompatible surfactant [48] which stabilizes organic O/W interfaces. It is made by Christine Contino-Pépin and Stéphane Desgranges at Université d'Avignon (France). Its molecular weight is 1456 g/mol and its CMC is not known.
- Krytox^{TM} 157 FSL, a commercial chemically inert perfluoropolyether fluid based surfactant with a functional end group that serves to stabilize W/PFC interfaces. Its molecular weight is 2500 g/mol and its CMC is not known.
- Zonyl FSO, a commercial fluorinated surfactant which stabilizes PFC/W interfaces.Its molecular weight is not given by the manufacturer, and its CMC was measured to be between 1.02 mM and 0.0688 mM depending on the method used for measurement [73].

The droplets used in this thesis are the following (shown in fig.2.1.5):

- nanometric single emulsions of PFH-in-water (PFH/W), or PFP-in-water (PFP/W), or PFOB-in-water (PFOB/W), stabilized by 0.1%wt F_8TAC_{13},
- micrometric single emulsions of PFH in water (PFH/W), stabilized by 0.1%wt F_8TAC_{13},
- micrometric single emulsions of ATBC and 0.025%wt Nile red in water (ATBC/W), stabilized by 0.1%wt $H_{12}TAC_7$,
- micrometric double emulsions of water-in-PFH-in-water (W/PFH/W), made of multiple water NDs (water + 0.9%wt NaCl + 1%wt sodium fluorescein), stabilized by 5%wt Krytox 157 FSL, dispersed in a larger PFH droplet stabilized by 0.1%wt F_8TAC_{13} in water,
- micrometric double emulsions of W/PFH/W, made of a single water micrometric droplet (water + 0.9%wt NaCl + 1%wt sodium fluorescein), stabilized by 5%wt Krytox 157 FSL, dispersed in a larger PFH droplet stabilized by 0.1%wt F_8TAC_{13} in water.

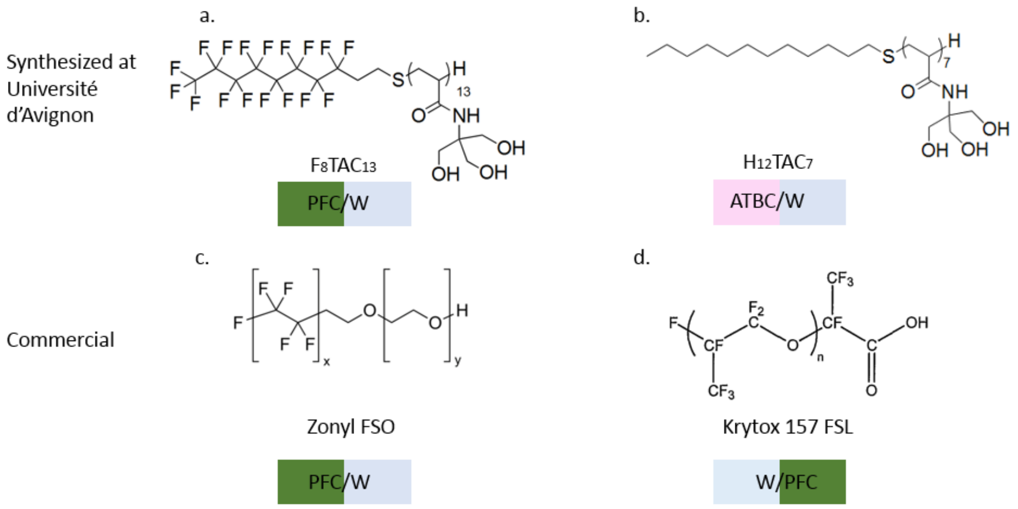

Figure 2.1.3 – *Chemical structure of surfactants used. a.* F_8TAC_{13} *is used to stabilize PFC/W emulsions. b.* $H_{12}TAC_7$ *is used to stabilize ATBC/W emulsions. c. Zonyl FSO is used to stabilize PFC/W emulsions. d. Kytox 157 FSL is used to stabilize PFC/W emulsions.*

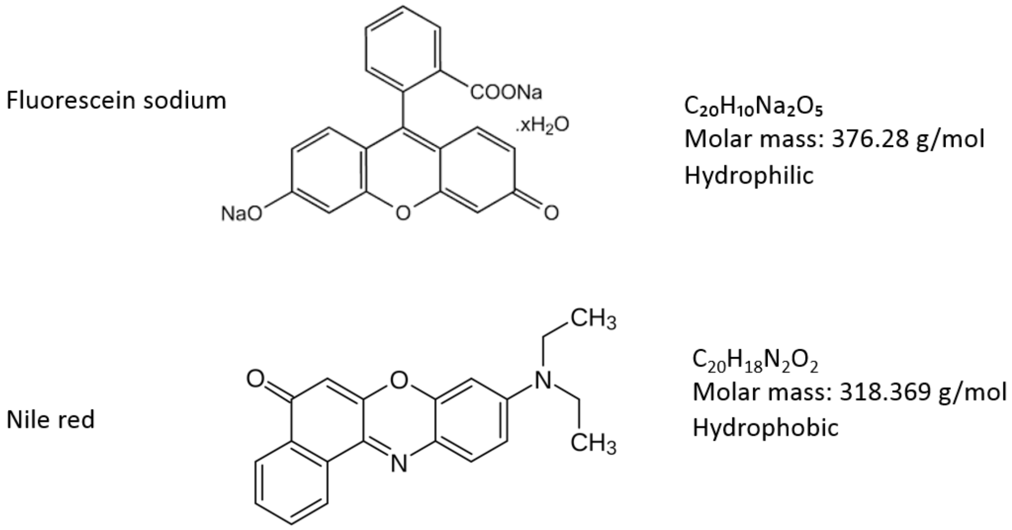

Figure 2.1.4 – *Chemical structures of fluorescein sodium and Nile red.*

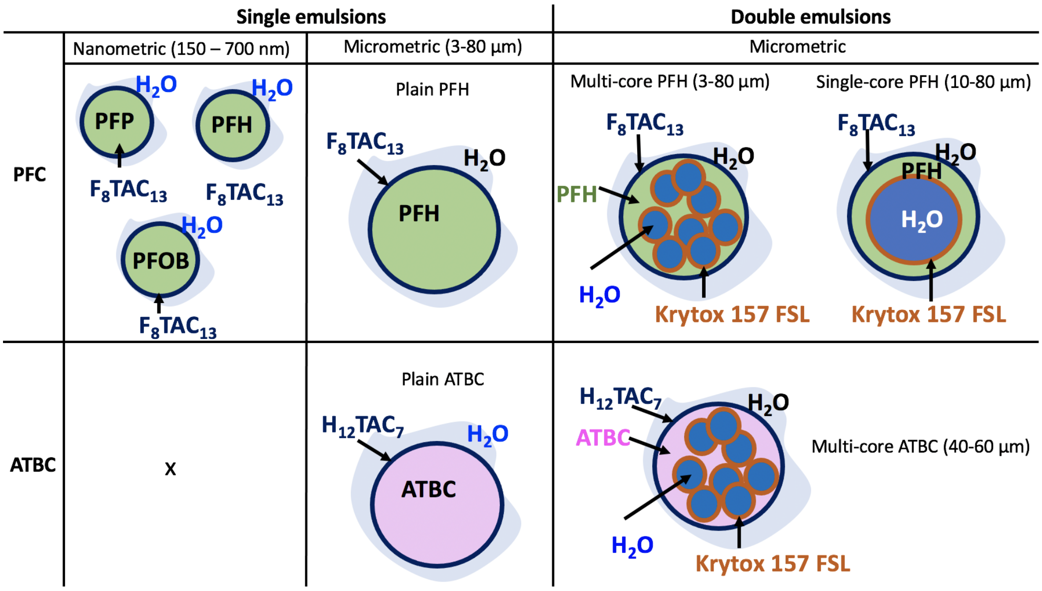

Figure 2.1.5 – *Table of all single and double elmusion types, made with PFC's or ATBC, that will be referred to in this thesis. The names of each emulsion types are shown in the corresponding box.*

2.2 Chip Designs

Micrometric single emulsions and multi-core double emulsions are made using the same chip design (fig.2.2.1 and fig.2.2.2).

The geometry used is called a flow-focusing device. It consists of a dispersed phase channel and two continuous phase channels, bringing their respective pressurized fluids to a nozzle. The size of this nozzle depends on the diameter of the droplet that we want. At the level of the nozzle, the two continuous phase arrive on the sides of the dispersed phase. Both phases are forced through the nozzle through hydrodynamic flow-focusing and the instabilities created by this geometric change cause a periodic break in the flow, thus creating a string of emulsion droplets.

Single-core double emulsions are made in a device that has two flow-focusing intersections in series (fig.2.2.3). The first one makes the emulsions of the dispersed phase in the intermediate phase, and the second junction encapsulates the first W/PFH emulsion in water.

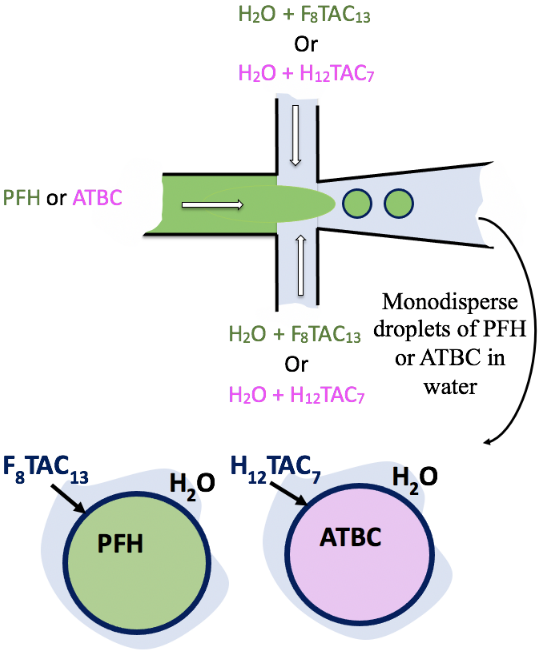

Figure 2.2.1 – *Scheme of microfluidic flow-focusing junction used to produce micrometric PFH or ATBC single emulsions.*

2.3 Chip fabrication

The chip circuits inside the microfluidic devices were designed in the lab using AutoCAD, with geometries found in the literature [74, 75]. These models were printed on wafers which served as mold to make the chips. Printing the designs on wafers was done using two different methods. The first one is high resolution laser lithography with a 3D Printer from Nanoscribe, performed by Justine Laurent from the laboratory Physique et Mécanique des Milieux Hétérogènes, at ESPCI. This method was used when there was only one chip to print at a time, on wafers (1 cm x 1 cm chip dimensions on 2.5 cm x 2.5 cm wafer dimensions). The second method is standard photolithography using SU8 photoresist resin on silicon wafers (10 cm diameter), from Institut Pierre Gilles de Gennes (Paris, France), performed by Vincent Faugeras (LPENS). This method was used when multiple chips had to be printed at a time (when trying out different geometries or to increase the production rate of chips for example).

The microfluidic chips were all made using polydimethylsiloxane (PDMS). The PDMS was poured onto the wafer which served as a mold for the circuit. The surface of a wafer is hydrophobic, and so is the PDMS. To prevent the

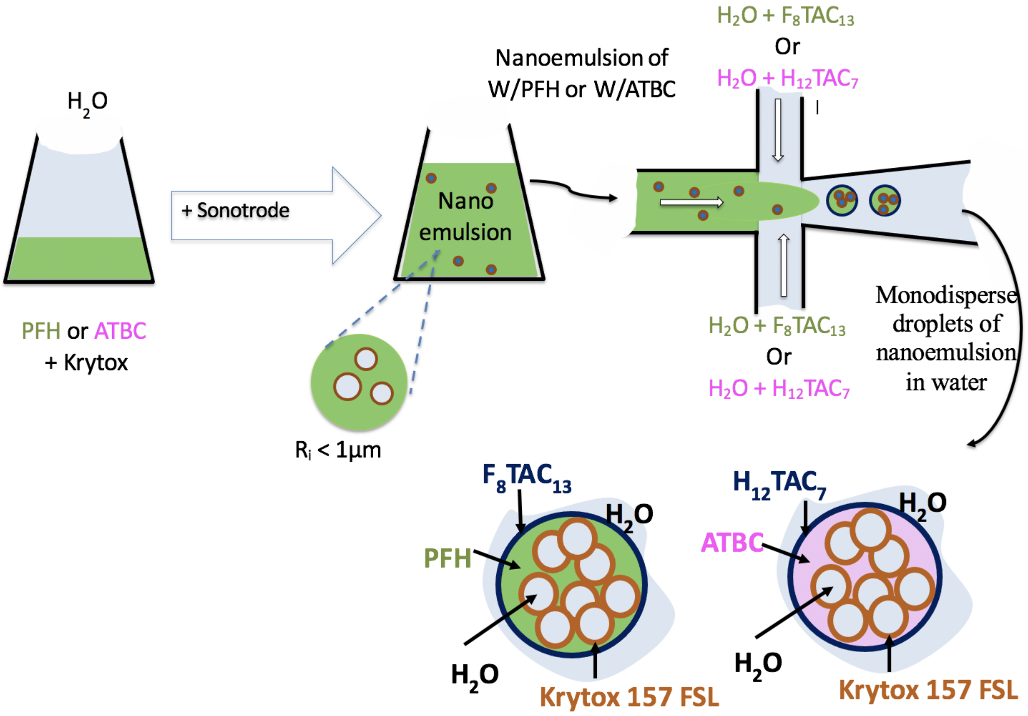

Figure 2.2.2 – *Scheme of production steps of multi-core PFH or ATBC double emulsions. Left: Sonication to produce the nanoemulsion. Right: Microfluidic flow focusing junction used to produce the double emulsion, with the nanoemulsion as the dispersed phase and water and the appropriate surfactant as the continuous phase.*

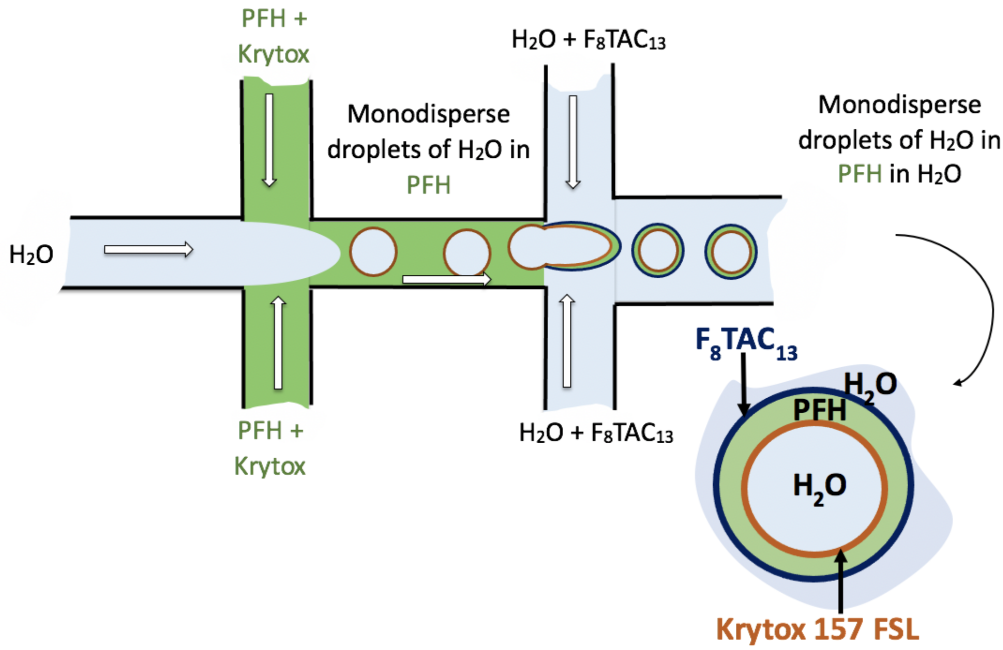

Figure 2.2.3 – *Scheme of two flow-focusing junctions used to produce single-core PFH double emulsions.*

PDMS from sticking to the wafer when making the mold of the chip, a surface treatment of the wafer surface is necessary. First, the surface of the wafer is activated using an air plasma (18W for 1 min). The wafer is put in a petri dish so that there is at least 1 cm of space between the wafer and the borders of the petri dish. Under a chemical fume hood, 20 µL of 1H,2H trichloromethylsilane (Sigma Aldrich, France) are taken with a micropipette and distributed equally onto the petri dish around the wafer (without actually touching the wafer). The petri dish is closed and left for 20 min, then the lid is removed and left open for 1h. The surface is now ready to be used with PDMS. The PDMS mixture was made of a 10:1 ratio of the silicone polymer and reticulating agent respectively. The height of the PDMS layer matters for the experiments; it needs to be higher than the PDMS circuit, but not too high so that the hole puncher used to make the holes for inlets and outlets can go through the entire layer. The ideal height is 3.5 mm, so the amount of PDMS needed in a specific container can be calculated accordingly. After it is poured, it is degassed in a vacuum then baked at 70°C for 2h. After the chip has cooled, it is cut in a square, leaving a little bit of space on the sides of the circuit (to increase the surface for sticking to strengthen the chip and avoid leakage during the experiment). The inlets and outlets were marked with a dot from a black marker (Stabilo OHPen Universal Permanent Marker S tip) then punched with a 0.35 mm diameter biopsy puncher (World Precision Instruments, USA). The chip was cleaned with isopropanol (VWR, France) and dried with nitrogen gas (particular attention was paid to drying the inlets and outlets as some isopropanol can be trapped there). A piece of adhesive tape was put on the circuit side of the chip, to keep it free from impurities. The chip was then bonded to a substrate (glass or thin layer of PDMS depending on the chip made, more details in Section 2.4).

2.4 Surface treatments

PDMS is hydrophobic, and the different phases used to make droplets are either hydrophobic or hydrophilic. In order for the continuous phase to remain on the outer side and for the droplet to remain stable, the channels of the chip need to have the right affinity. Therefore, depending on the droplet that was produce, the surface treatment will be different.

2.5 Single emulsions and multi-core double emulsion chips

A microscope glass slide (76x26x1 mm, Brand, Germany) was cleaned with ultra pure water, then ethanol, then water again, then ethanol again, and dried with nitrogen gas. The tape was removed from the circuit side of the chip, and a new piece of adhesive tape was used to clean it one more time before bonding. The circuit side of the chip and the glass slide were both activated in an air plasma (18W for 1 min, Harrick Scientific, NY, United States) (fig.2.5.2). They were then put in contact to bond, and placed in the oven at 70°C for 30 min. The chip was then taken out of the oven and cooled to room temperature. The outer phase of these emulsions is hydrophilic, so the PDMS circuit had to undergo a surface treatment to make it hydrophilic. To do that, the bonded chip was activated in the air plasma (18W for 1 min). Water was then inserted inside the microfluidic chip by inserting a tube from the pressure controllers (fig.2.5.1) into the continuous phase inlet, and applying pressure to reach a flow rate of 3 μL/min for 15 min (fig.2.2.1). At this point, the chip was adequately treated to start injecting the different emulsion phases into their respective inlets.

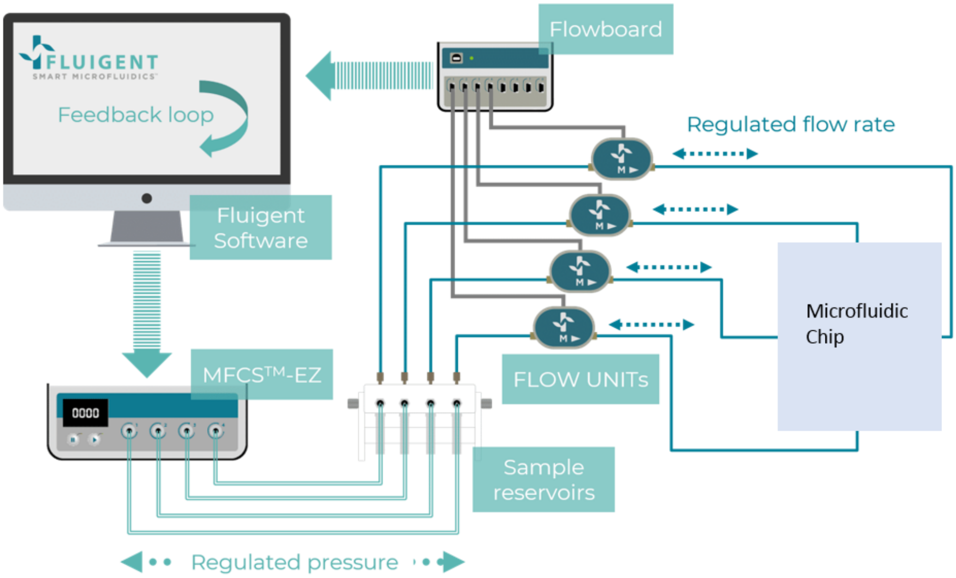

Figure 2.5.1 – *Scheme of microfluidic setup with 4 channels and 4 flow rate sensors (flow units). The desired pressure for each channel is entered into the software, which controls the MFCZ-EZ pressure controllers (controlled in mbar, 1mbar = 100 Pa). The pressure controllers apply the command pressure onto the headspace of the vials that are screwed onto a tube rack, which induces fluid flow into the tubes. The fluids reach their respective flow units, which send the detected flow rates back to the software which are indicated on the computer. The fluids then flow into their respective inlets and enter the microfluidic chip. (from Fluigent website [76], Le Kremlin-Bicêtre, France).*

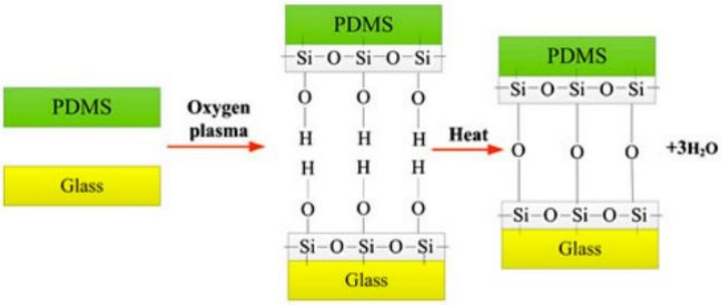

Figure 2.5.2 – *Scheme of covalent bonds formation following plasma activation of chip surfaces copied from [77]*

2.6 Single-core double emulsion chip

The chip used to make single-core emulsions has three inlets (one for each phase) and one outlet (fig.2.2.3). For the emulsions to remain stable during production, the continuous phase of the emulsion has to have an affinity with the walls of the channels. The walls of the blue channels on fig.2.2.3 should be hydrophilic since they are in contact with water, while the walls of the green channels should be hydrophobic since are in contact with PFH. This partitioned surface treatment is achieved by using the method developed by Bodin-Thomazo et al [78]. It consists of using a black marker (Stabilo© OHPen superfine) to draw a line on the PDMS, on the part of the channel that needs to remain hydrophobic before doing the plasma treatment.

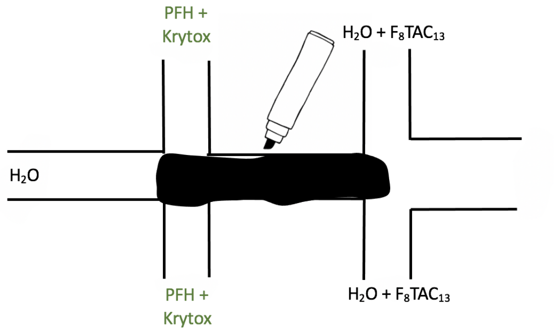

Figure 2.6.1 – *Scheme of partitioned surface treatment of single-core double emulsion droplet chip with marker patterning technique.*

The chip is bonded to a piece of flat PDMS that is made with the same 10:1 PDMS ratio. This piece is slightly longer and larger than the chip (4 mm on each side), but of similar height (3-4 mm). The black marker is used to draw a line on the flat PDMS that mirrors the line drawn on the chip so that when they are put in contact to bond, the two black lines superimpose. Doing this allows the channels to be shielded from the plasma activation and therefore they remain hydrophobic, while the other parts of the chip that have not been marked become activated. Once the chip and the piece of flat PDMS are taken out of the plasma, they are aligned carefully and are put in contact for 2 min. A 500g mass is placed on this system to ensure bonding. After 1 min, the chip is connected to the pressure controllers. Methanol (Sigma Aldrich, France) is passed through the dispersed phase inlet at 3 µL/min for 1 minute to remove the marker filling the channel. Once the marker is gone, water is passed through at 3 µL/min for 20 min (See Section 2.7 for an explanation of the microfluidic experimental set up).

2.7 Microfluidic Experimental set-up

All of the solutions used inside the microfluidic devices are filtered with 0.2 µm Acrodisc Syringe Filters (Pall, France) and used without further purification.

The fluids are contained in 1.8 mL solution-filled vials screwed onto a 4-channel tube rack. The fluids are injected into the microfluidic chips with pressure controllers from Fluigent (MFCS –EZ, Le Kremlin Bicêtre, France), and the flow rates are recorded with flow units from Fluigent, sizes S (for aqueous phases) and M (for the oil phase). The software used to control the pressures of the fluids injected is All-in-One (AiO) (Fluigent). The tubing used to connect the pressure controller to the flow units, and the flow units to the microfluidic chip, is made of poly(tetrafluoroethylene) with an internal diameter of 0.125 mm (VWR, France). 15 mm long metallic adaptors (PHYMEP, France) with an outer diameter of 0.61mm and internal diameter of (0.35 mm) are used to connect the tubing from the controllers to the chip inlets and from the outlets to the exit tubes. The microfluidic set-up is cleaned after each experiment by passing detergent (RBS T 105, RBS, Belgium) at a concentration of 20 mg/L of water at 7 µL/min for 20 min, then water at 7 µL/min for 20 min, then isopropanol at 70 µL/min for 20 min, and it is finally dried at 70 mbar for 20 min. The flow rates for all channels must be stable before shutting off the setup.

The microscope platform consists of an inverted microscope (Leica DM IRB) with objectives ×10, ×40, and ×60, as well as a fluorescence module. A temperature plate (PE 120 Peltier System, Linkam) is used to control the temperature of the chip when needed (-20°C to 120°C). The images and videos are recorded for analysis using a high-speed camera (SC1, Edgertronic, USA).

2.8 Droplet production in microfluidic devices

Various junction geometries exist to produce droplets in microfluidic devices (fig.2.8.1). The idea in all of these geometries is to create an interface between the two phases, and induce a destabilization which will lead to droplet pinch off and formation. Droplet formation is characterized by two dimensionless numbers. The capillary number, Ca,

$$Ca = \frac{\mu v}{\gamma}, \tag{2.1}$$

where μ is the dynamic viscosity (Pa.s), v is the average fluid velocity (m/s), and γ is the surface tension (N/m). The Weber number, We, illustrates the competition between inertia forces and surface tension force.

$$We = \frac{\rho v^2 l}{\gamma}, \tag{2.2}$$

where ρ is the density of the fluid (kg/m^3), v is the velocity (m/s), l is the diameter of the drop or of the liquid jet, and γ is the surface tension (N/m).

The Ca number of the outer fluid and the We of the inner fluid are essential to understand the formation. They can be changed to alter the production rate, regime or droplet diameter. The droplet generation behaviour can be classified into different regimes (fig.2.8.1).

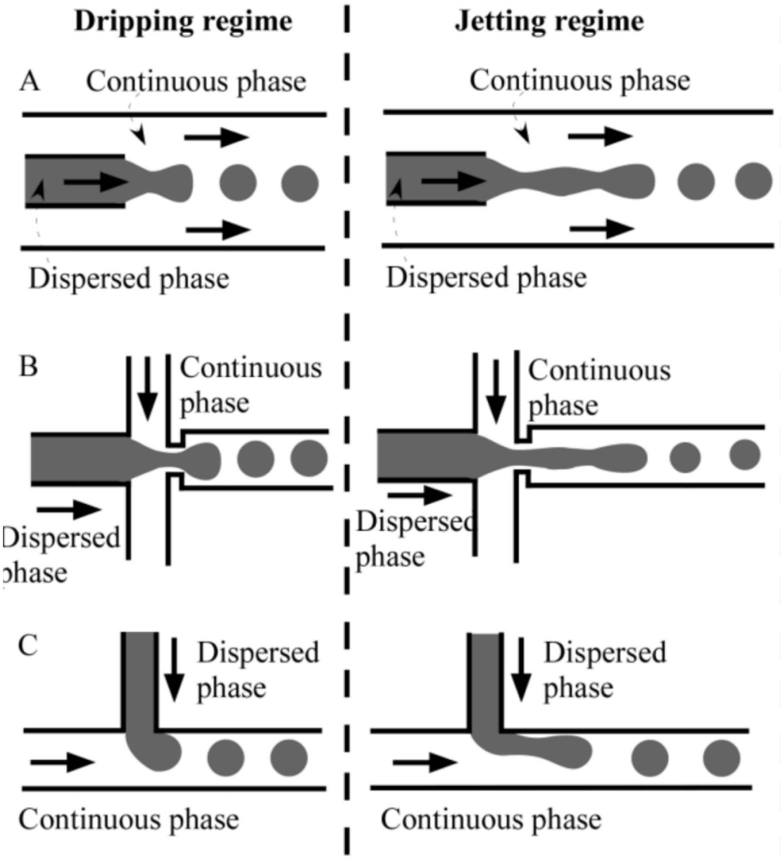

Figure 2.8.1 – *Scheme of dripping and jetting flow regimes in A: a co-flow device, B: a flow-focusing device, C: a T-junction device (copied from Nunes et al [79])*

2.8.1 Dripping regime

Dripping occurs at low flow rates of both phases. The droplet of the inner fluid grows and eventually pinches off to move downstream.
This process is analogous to what we see if we reduce the flow rate of a tap. Initially the droplet will stick to the tip and continue to grow, but at one point the droplet size increases and there is a pinch off.
In a microfluidic device, the droplet breaks due to the shear force, because the viscous drag exerted by the continuous phase is high. Initially the droplet diameter is small and the surface tension dominates. As the droplet grows, the radius increases, and the viscous drag exerted by the continuous fluid increases. The droplet breaks when the drag forces and surface tension are comparable in magnitude. If we change the Ca we can control the droplet diameter, which decreases as Ca is decreased. In the dripping regime the droplet size only depends on the shearing due to the velocity of the outer fluid. As the flow rate ratio,

$$\frac{Q_{in}}{Q_{out}} \tag{2.3}$$

increases, the droplet production frequency increases.

2.8.2 Jetting regime

If Q_{out} is increased above a critical value, there is a transition into the jetting regime. The higher Q_{in}, the lower the critical value of Q_{out}. The critical value of Q_{out} also depends on the viscosity ratio of the inner and outer fluids.

When Q_{out} increases, the droplet diameter is reduced and approaches the size of the nozzle. Continuing this increase leads to the elongation of the liquid stream and thus to the formation of a jet. That jet later on breaks up into droplets, due to the Rayleigh-Plateau instability:

The cylindrical jet of the inner fluid is moving along the channel, so there is a straight interface between the inner and outer immiscible fluids. Some disturbances then occur at the interface. On fig.2.8.2, the cross section at minima (R_A) is smaller than radius of curvature at maxima (R_B). The pressure inside the jet is higher than on the outside of jet because the pressure inside the concave side is higher. $P_A - P_{out} \approx \frac{\gamma}{R_A}$ and $P_B - P_{out} \approx \frac{\gamma}{R_B}$, since R_A is smaller than R_B so there is a higher pressure at A than B. A higher pressure will lead to fluid transfer from A to B so more accumulation of liquid at B. The initial disturbance will further amplify, and eventually form a drop.
Because the outer flow has a higher velocity, it speeds up the liquid jet so the cross section of the jet decreases, further downstream the diameter of the jet

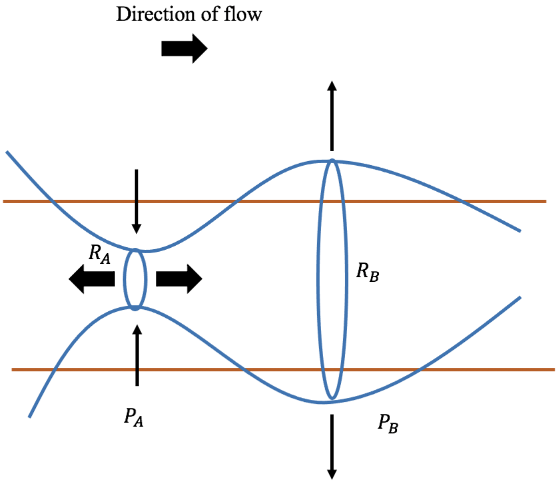

Figure 2.8.2 – *Scheme of Rayleigh Plateau instability during the flow of the inner phase into the outer phase.* R_A *is the radius is the first cross-section,* P_A *is the pressure at the first cross-section.* R_B *is the radius is the second, larger cross-section,* P_B *is the pressure at the second, larger cross-section. The thin arrows show the expansion of the cross-section. The thick arrows show the direction of the flow.*

is constant and the Rayleigh-Plateau instability leads to the formation of a droplet that is proportional to the diameter of the jet.

The squeezing regime, characteristic of flow-focusing geometries, occurs due to the continuous phase pushing on both side of the dispersed phase, before entering the nozzle (the junction that has a smaller width than the rest of the channels see fig.2.8.1B). The thread that results thins through hydrodynamic focusing to reach a diameter comparable to the size of the channel and droplets are formed through a pinch off that results from the Rayleigh-Plateau instability [80]. In flow focusing devices, the size of the droplet is also determined by the size of the nozzle through which the disperse phase is squeezed. By being in the dripping regime, the diameter of the droplet can be the same size as the nozzle width. By being in the jetting or squeezing regime, the diameter of the droplet can be smaller than the size of the nozzle.

2.8.3 Single emulsion microdroplets

To produce droplets of various sizes, different flow rates were used (See Table showing pressure, flow rate for each phase for each type of droplet). In the following droplet production systems presented below, Ca of the outer phase is on the order of 10^{-2} to 10^{-3}, and We is on the order of 10^{-2} to 10^{-4}, depending on the fluid used and the velocity. The different phases are injected into their corresponding inlets by applying a pressure at the headspace of each inlet using the pressure controllers. The start flow rates are 1 µL/min for all phases until they are stable (it is important to avoid any backflow at this step, to keep the proper surface treatment). Once they are stable, droplet production can start. The diameter of the droplets is checked throughout the experiment by taking videos using the ultra fast camera, and using an in-house Matlab code which allows to determine the radius from the image (Section 2.10.2 Matlab analysis for microdroplets). Once the desired diameter is obtained, the collection of droplets can start. They are recuperated in a 1.8 mL vial in normal saline and put in the fridge at 4°C for conservation.

		P (mbar)	Q (μL/min)
10μm	Φ_d	250	0.9
	Φ_c	480	8
40μm	Φ_d	180	0.9
	Φ_c	450	8
60μm	Φ_d	150	1
	Φ_c	200	2.5

Table 2.1 – *Table showing the pressures (mbar), denoted P and flow rates (µL/min), denoted Q of the dispersed phase (denoted Φ_d) and continuous phase (denoted Φ_c) to produce 10 µm, 40 µm and 60 µm diameter PFH single emulsion droplets using the flow-focusing chip shown in fig.2.2.1 using Fluigent pressure controllers, flow unit size M for the dispersed phase and flow unit size S for the continuous phase.*

2.8.4 Multi-core double emulsion droplets

The dispersed phase of the multi-core double emulsion droplet is a nanoemulsion that is produced using a Branson Ultrasonics Sonifier horn. The dispersed aqueous phase containing water, 0.9%wt NaCl, and 1%wt sodium fluorescein and the continuous phase containing PFH or ATBC and 5%wt Krytox^{TM} 157 FSL are added to a 1.8 mL vial (one used for microfluidic experiments as described in section 3.1.) with the desired volume fraction. They are sonicated directly into the vial, which is immersed in an ice-water

		P (mbar)	Q (μL/min)
40μm	Φ_d	180	N/A
	Φ_c	450	8
60μm	Φ_d	150	N/A
	Φ_c	200	2.5

Table 2.2 – *Table showing the pressures (mbar), denoted P and flow rates (μL/min), denoted Q of the dispersed phase (denoted Φ_d) and continuous phase (denoted Φ_c) to produce 40 μm and 60 μm diameter ATBC single emulsion droplets using the flow-focusing chip shown in fig.2.2.1 using Fluigent pressure controllers, and flow unit size S for the continuous phase. The flow rate of the dispersed was not recorded as it contains Nile red which tends to plug the flow unit.*

bath to avoid unwanted vaporization due to the heating generated during the process. The sonication is done at a frequency of 20 kHz, 40% of maximum amplitude, and cycles of 5 seconds on and 10 seconds off, for 2 min. The sonic tip is then cleaned with water and methanol after each use. This nanoemulsion is then used as the dispersed phase in the flow-focusing chip (see fig. 2.2.2). The diameter of the droplets is checked throughout the experiment by taking videos using the ultra fast camera, and using an in-house Matlab code which allows to determine the radius from the image (Section 2.10.2 Matlab analysis for microdroplets). Once the desired diameter is obtained, the collection of droplets can start. They are recuperated in a 1.8 mL vial in normal saline and put in the fridge at 4°C for conservation.

2.8.5 Single-core double emulsion droplets

Following the surface treatment of the chip, the fluids are injected into the chip in a specific order. The vial containing the water used for the hydrophilic surface treatment is changed on the tube rack and replaced with the solution of the dispersed phase (water, 0.9%wt NaCl, and 1%wt sodium fluorescein). Once the dispersed phase is inside the chip, the continuous phase (water and 0.1%wt F_8TAC_{13}) is injected into the chip. Finally, the intermediate phase, PFH and 5%wt Krytox^{TM} 157 FSL is injected. The reason for this order is to keep the selective hydrophilic surface treatment stable, and when injecting a PFH phase it might travel to those hydrophilic areas and destabilize it.

For single-core double emulsions, the flow rates used are shown in table.2.8.5. The flow rates are adjusted within these ranges so as to obtain one

		P (mbar)	Q (μL/min)
10μm	Φ_d	250	N/A
	Φ_c	480	8
40μm	Φ_d	180	N/A
	Φ_c	450	8
60μm	Φ_d	150	N/A
	Φ_c	200	2.5

Table 2.3 – *Table showing the pressures (mbar), denoted P and flow rates (μL/min), denoted Q of the dispersed phase (denoted Φ_d) and continuous phase (denoted Φ_c) to produce 10 μm, 40 μm and 60 μm diameter multi-core droplets using the flow-focusing chip shown in fig.2.2.2 using Fluigent pressure controllers and flow unit size M. The flow rate for the dispersed phase was not recorded, since it is a nanoemulsion which tends to plug the flow units.*

single water droplet inside the PFH capsule, with the desired volume fraction and size of the droplet. The diameter of the inner and outer droplets are checked throughout the experiment by taking videos using the ultra fast camera, and using an in-house Matlab code which allows to determine the radii from the image (Section 2.10.2). Once the desired diameters and volume fraction are obtained, the collection of droplets can start. Fig. 2.8.3 shows an example of single-core emulsions produced with this method. They are recuperated in a 1.8 mL vial in normal saline and put in the fridge at 4°C for conservation.

2.8.6 Single emulsion nanodroplets

The microfluidic chip used to produce nanodroplets is inspired by the one from Song et al[81]. It consists of a herringbone architecture that serves as a mechanical micro-mixer for the emulsion. The principle behind the production of this emulsion is the Ouzo effect (explained in Section 1.4.2). A primary emulsion is produced using PFC and ethanol at a volume ratio that depends on the diameter of NDs wanted (e.g. 2:98 to obtain 200 nm droplets). The continuous phase is water and 0.1%wt F_8TAC_{13}. The use for the micro-mixer is that mechanical agitation has been shown to make the population of droplets monodisperse[81]. The droplet diameters that can be obtained with this system range from 150 nm to 700 nm. This chip undergoes a hydrophilic surface treament, using the same method as for the micrometric single emulsion and multi-core emulsion chip (Section 2.4). The fluids are

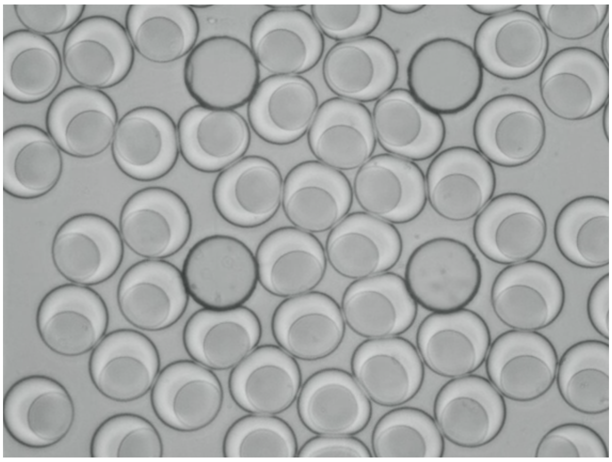

Figure 2.8.3 – *Monodisperse single-core double emulsion droplets of W/PFH/W, of 80 µm diameter made in the double flow-focusing microfluidic device (Camera Model SC1, Edgertronic, USA, microscope Leica DM IL objective x 10. The four larger are pillars that serve to stabilize the chip and avoid sagging.*

injected into the chip in no specific order. The droplets are produced at a flow rate ratio of 1:1. They are recuperated in a 1.8 mL vial of water and put in the fridge at 4°C for conservation.

2.9 Single emulsion nanodroplet production with microfluidizer

Single emulsions that are smaller than 1 µm are made using a high-pressure microfluidizer (model F12Y, internal dimension of 75 µm).

The dispersed (0.57 mL PFH) and continuous (4 mL 0.9%wt NaCl solution in water + 70 mg F_8TAC_{13} phases are mixed in a Falcon 15 mL tube and vortexed for 2 minutes. This emulsion solution is put into the left syringe of the microfluidizer for insertion. Once the solution has fully entered the microfluidizer, it is pressurized and arrives in the right syringe. The syringes are exchanged, and the process is repeated. 8 passages are done to obtain droplets of 200 nm. After that, the resulting solution is centrifuged for 30 seconds at 2 000 g (Mini Star, VWR) and the supernatant is transferred into a different vial by using a 1000 µL pipette The pellet is discarded. The supernatant is then centrifuged at 4°C at 17 000 g for 40 min (Micro star 17 R, VWR). The supernatant is then discarded and replaced with the same volume of 0.9%wt NaCl solution. It is mixed with the pellet to form a ho-

		P (mbar)	Q (μL/min)
10μm	Φ_{d1}	40	0.8-1.3
	Φ_{d2}	60	5.5
	Φ_c	80	8
40μm	Φ_{d1}	60	0.8-1.3
	Φ_{d2}	50	1.0-1.5
	Φ_c	80	2.0-2.5
60μm	Φ_{d1}	65	0.8-1.3
	Φ_{d2}	50	0.9-1.3
	Φ_c	75	2.0-2.5

Table 2.4 – *Table showing the pressures (mbar), denoted P and flow rates (μL/min), denoted Q of the aqueous dispersed phase (denoted Φ_{d1}), the PFH dispersed phase (denoted Φ_{d2}) and the continuous phase (denoted Φ_c) to produce 10 μm, 40 μm and 60 μm diameter single-core droplets using the flow-focusing chip shown in fig.2.2.3 using Fluigent pressure controllers and flow unit sizes S (for Φ_{d1} and Φ_{d2}) and M (for Φ_c).*

mogenous solution, using a 1000 µL pipette to slowly move the pellet up and down until the solution appears homogeneous. This is the final solution of nanodroplets.

2.10 Droplet Analysis

2.10.1 Dynamic Light Scattering for nanodroplets

Dynamic Light Scattering (DLS) is used to measure the size and polydispersity of the nanoemulsions (either the ones made in batch used as the dispersed phase for the multi-core emulsions, the ones made in microfluidics or with the microfluidizer). The polydispersity index (PDI) is an index which can be measured using

$$PDI = (\frac{\sigma}{\bar{d}})^2 \tag{2.4}$$

where σ is the standard deviation of the droplet diameters and $\bar{d}$ is the mean diameter of the droplets. A PDI ¡ 0.1 indicates a monodisperse population, meaning that all droplet diameters are homogenous. It was done using an ALV/CGS-3 platform based goniometer system (from ALV GmbH). The measurements were performed at room temperature, and scattering angles,

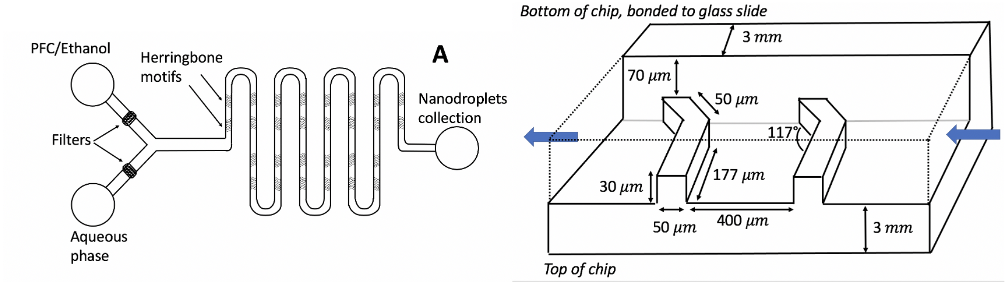

Figure 2.8.4 – *Herringbone architecture of chip used to produce NDs using the Ouzo effect.*

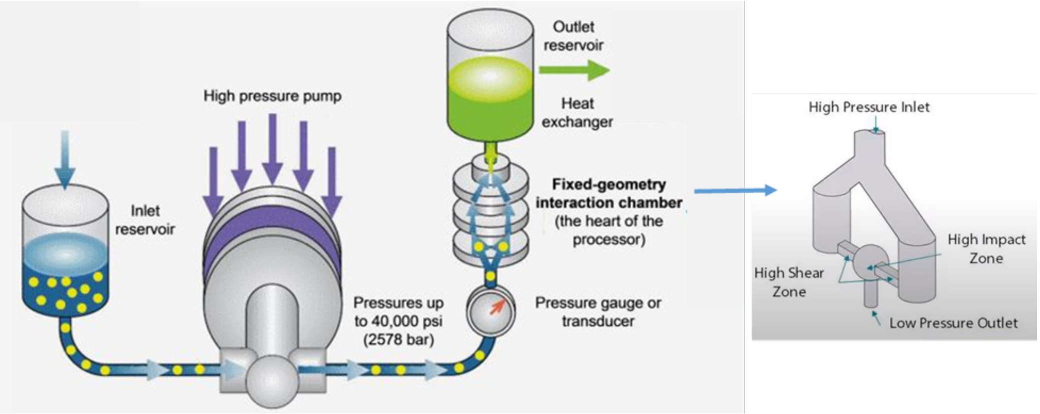

Figure 2.9.1 – *Scheme of microfluidizer mechanism (copied from Microfluidics*$_{TM}$ *documentation).*

θ, ranging from 90° to 130°, with a step of 10°. At each angle θ, the device provided the decay rate $\Gamma_\theta = q^2(k_BT/6\pi\eta R)$; where k_B is the Boltzmann constant, T is the temperature in K, η is the viscosity of the solvent, and $q(\theta) = 4\pi n sin(\Theta/2)/\lambda$ is the magnitude of the scattering vector. The refractive index of water is n = 1.33 and λ = 633 nm is the laser wavelength and θ is the scattering angle. A fit of the curve by the cumulant method made it possible to determine the hydrodynamic droplet mean radius R along with the PDI[82, 83, 84].

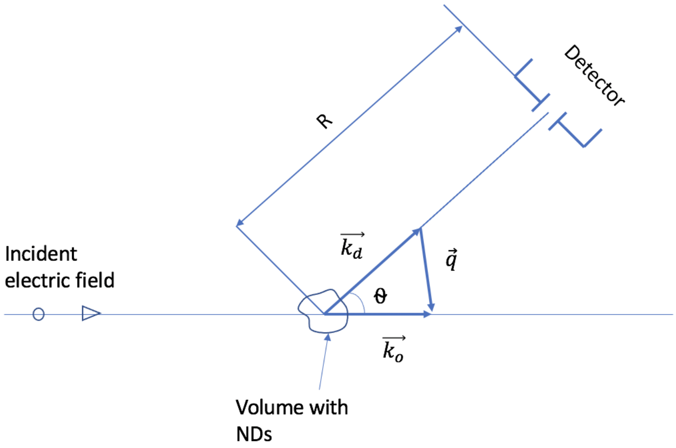

Figure 2.10.1 – *Scheme of principle of DLS.* k_d *is the wave vector*

2.10.2 Matlab analysis for microdroplets

The size, polydispersity and volume fraction of the micron size droplets were estimated from a series of videos taken with an ultra-fast camera (Model SC1, Edgertronic, USA) during their production. The collected recordings were treated with an in-house MATLAB program. The code uses a Circular Hough Transform (CHT) based algorithm for locating the droplets and then estimating their diameter along with the polydispersity index (PDI). This approach was chosen owing to its robustness in the presence of noise, occlusion and varying illumination. For single-core double emulsions, this function finds two circles: the one formed by the interface between the aqueous dispersed phase and the intermediate PFH phase, and the one formed by the interface between the intermediate PFH phase and the aqueous continuous phase. The inner circle defines the size of the water droplet inside the PFH capsule, while the second circle defines the outer limit of the PFH capsule (fig.2.10.2).

2.11 Acoustic Droplet Vaporization set up

The set up used for the ADV experiment is shown in fig. 2.11.1. A waveform generator (Model 33220A from Agilent) generated an electrical signal that goes first through a radio-frequency power amplifier (Model 150A100C from AR France), and then a power reflection meter (Model and NRT from Rohde Schwarz) measuring the delivered average electrical power. The electrical signal was converted into an acoustic wave by a focused transducer

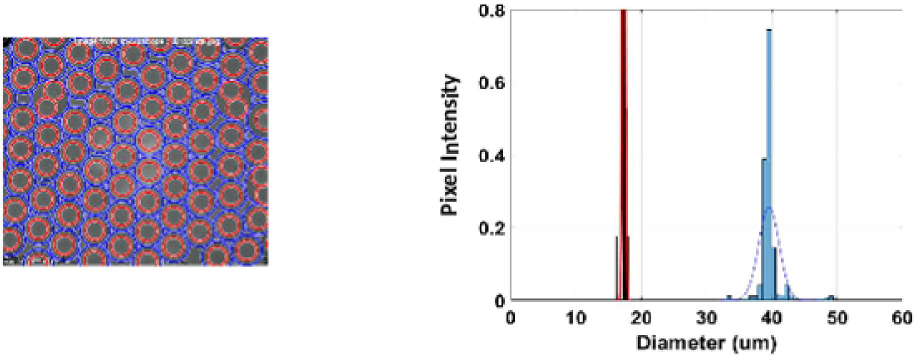

Figure 2.10.2 – *Example of single-core double emulsion droplets analysis with Matlab code.*

(Model H-101-G from Sonic concepts Inc.), whose fundamental mode is at 1.1 MHz. It is a curved monoelement transducer (the radius of curvature is 63.20 mm) that is focused at 51.74 mm from the transducer rim. It is centered at 1.07 MHz (fundamental mode) with a bandwidth varying from 0.710 dB to 1.390 dB. The dimension of the focal zone at the fundamental is 12.90 mm long and 1.9 mm wide.The acoustic wave propagated into a water tank thermostated at 20 ± 0.2 °C and connected to a degassing machine (Model WDS-1005 from Sonic Concepts). A PCR tube was mounted onto a positioning system equipped with three directional motors, along the x, y, and z directions and controlled by an in-house MATLAB program. The center of the sample tube was positioned at the transducer focus. A 0.2 mm needle hydrophone (model Y-107 from Sonic Concepts), whose focus overlaps the transducer one inside the tube, continuously monitored the emitted signal. The center is identified as the point at which the output voltage recorded by the hydrophone reaches its maximum for a given input pressure. We also used a Fabry-Pérot fiber-optic ultrasonic hydrophone (Precision Acoustics, Dorchester, UK) for the measurement of temperature[85, 86]. Temperature fluctuations never exceeded 0.5 ºC at the applied pressures. Before each experiment, the amplifier was turned on and the water degassed for at least 1h.

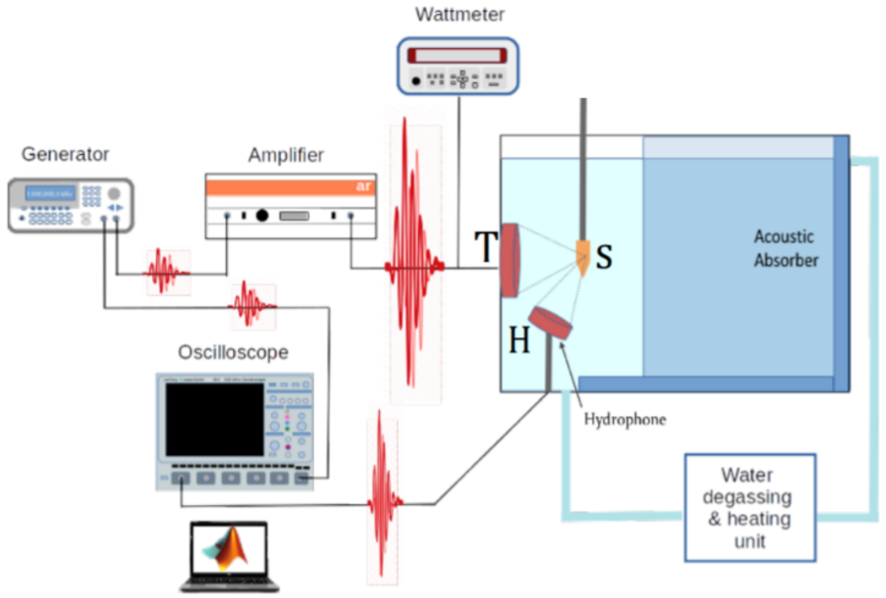

Figure 2.11.1 – *Experimental setup for ADV and measuring cavitation. A 1.1 MHz transducer (T) vaporized the droplets while the hydrophone (H) recorded at 0.55 MHz the scattered emissions due to the subharmonic response of vapor microbubbles in the sample (S).*

2.12 Acoustic delivery set up

In these experiments, we determined the amount of fluorescent probe released from emulsion droplets following an acoustic treatment. We assessed the release of hydrophilic sodium fluorescein from the water core of double emulsions and the release of hydrophobic Nile red from the oil core of single ATBC emulsions. These experiments were done in water, so the droplets sedimented to the bottom of the tube very quickly. For this purpose we used a different set up (shown in fig.2.12.1) than for the ADV experiments. For the ADV experiments, the transducer was perpendicular to the sample, therefore the wave arrived in the middle of the sample tube. In the case of delivery experiments, the droplets are at the bottom therefore the transducer was placed underneath the tube. We used a circular hollow stand of height 10 cm, on which we place a holder for the tube. A 3mm hole was made into the holder, to allow the passage of the acoustic wave to the sample tube. This system ensured that the sample was always placed at the same coordinates in the water tank, so that the bottom of the tube was always at the focus.

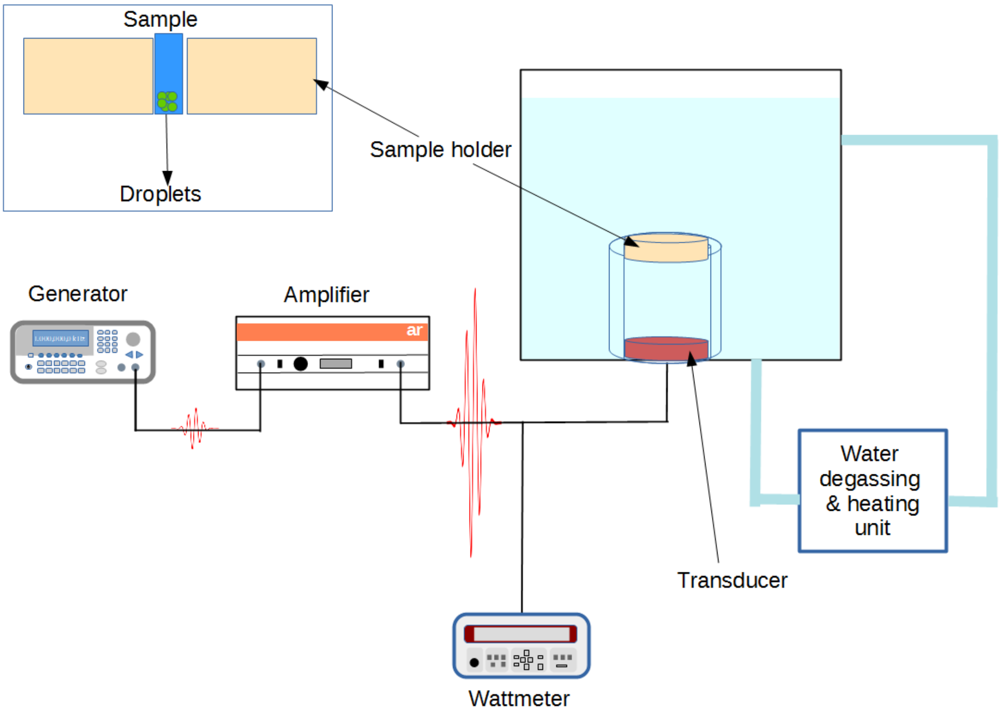

Figure 2.12.1 – *Acoustic set up used to perform acoustic delivery experiments.*

2.12.1 Spectrofluorometer

The analysis of the fluorescence intensity was done using a spectrofluorometer (Jasco Spectrofluorometer FP-8300, Germany), which was turned on 15 min before each experiment. In this technique, the fluorophore is excited at a wavelength and emits at a different (longer, higher) wavelength. For fluorescein, the excitation was done at 470 nm and the emission wavelength analyzed was 513 nm. The concentration of fluorescein present in the sample was calculated from a standard curve (fig.2.12.2) which was obtained using various concentrations of fluorescein in normal saline (9g NaCL/L of water). The analysis of the fluorescence of Nile red was done using an excitation wavelength of 560 nm and emission wavelength of 578 nm. The intensity of fluorescence was used to determine the concentration released, using the standard curve shown in Fig.2.12.3.

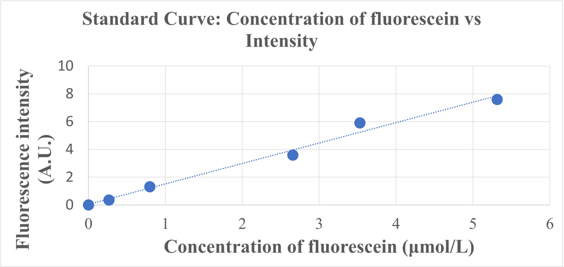

Figure 2.12.2 – *Standard curve of the concentration of fluorescein vs the associated intensity of fluorescence obtained from spectrofluorometry analysis, used to calculate the concentration of fluorescein released from the intensity value.*

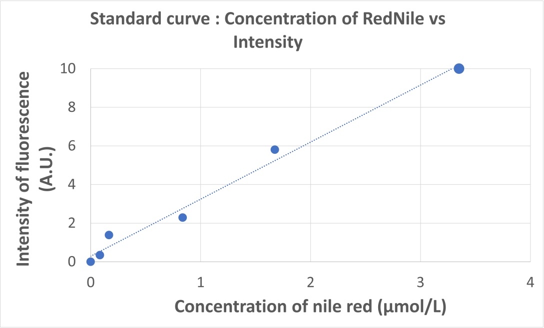

Figure 2.12.3 – *Standard curve of the concentration of Nile red vs the associated intensity of fluorescence obtained from spectrofluorometry analysis, used to calculate the concentration of Nile red released from the intensity value.*

Chapter 3

Results

3.1 Ultrasound Induced Vaporization of Perfluorohexane Droplets and Perfluorohexane/Water Droplets. Evidence of a heterogeneous nucleation.

The goal of targeted drug delivery is the spatial and temporal localization of a therapeutic agent and its associated bio-effects. One method of drug localization is acoustic droplet vaporization, whereby drug-laden perfluorocarbon (PFC) droplets are vaporized into gas bubbles using ultrasound, thereby releasing drug locally.

The Mechanical Index (MI) is an indication of the bioeffects due to ultrasound. It is expressed by

$$\frac{P}{\sqrt{f}} \tag{3.1}$$

where P is the peak negative pressure in MPa and f is the frequency in MHz. According to the FDA, diagnostic ultrasound should not exceed $MI = 1.9$ [87].

This work proposes a novel class of versatile PFC vectors - perfluorohexane (PFH) droplets produced as an emulsion made of a water core (where a potential hydrophilic drug can be dissolved), which is vaporized by focused ultrasound. A microfluidics technique was adopted to generate stable and monodisperse single (PFH-in-water) and double (water-in-PFH-in-water) emulsions. We investigated the acoustic vaporization threshold of these droplets as a function of two key parameters: the droplet diameter and the architecture of the water core of the droplet. Firstly, we found that the acoustic vaporization of the droplets occurs at low pressures which would avoid any deleterious biological effects when employed clinically (MI less than 2, in accordance with FDA regulations). Secondly, an inverse relationship is observed between the vaporization initiation threshold and the droplet size. Thirdly, we show that increasing the number of droplets lowers the vaporization threshold. Overall, we discuss a model of heterogeneous nucleation occurring on a soft surface, which explains the vaporization mechanism.

Ultrasound Induced Vaporization of Perfluorohexane Droplets and Perfluorohexane/Water Droplets. Evidence of a heterogeneous nucleation.

R. Ramesh[a,b,*], C. Thimonier[a,b,c,*], S. Desgranges[d], V. Faugeras[b], F. Coulouvrat[e], J. Laurent[f], G. Marrelec[a], C. Contino-Pépin[d], W. Urbach[b], C. Tribet[c], N. Taulier[a]

[a] *Sorbonne Université, CNRS, INSERM, Laboratoire d'Imagerie Biomédicale, LIB, F-75006 Paris, France.*
[b] *Laboratoire de Physique de l'École Normale Supérieure, ENS, Université PSL, CNRS, Sorbonne Université, Université de Paris Cité, F-75005 Paris, France.*
[c] *Département de Chimie, P.A.S.T.E.U.R., École Normale Supérieure, Université PSL, Sorbonne Université, CNRS, Paris 75005, Paris, France*
[d] *Avignon Université, Équipe Systèmes Amphiphiles bioactifs et Formulations Eco-compatibles, UPRI, 84000 Avignon, France.*
[e] *Sorbonne Université, Institut Jean le Rond d'Alembert, CNRS, 4 place Jussieu, 75005 Paris France.*
[f] *PMMH, ESPCI, Université PSL, CNRS, Sorbonne Université, Université de Paris Cité, 75005 Paris France.*

Abstract

Droplets made of liquid perfluorocarbon undergo a phase transition and transform into microbubbles when triggered by ultrasound of intensity beyond a critical threshold: this mechanism is called acoustic droplet vaporization (ADV). The advantages of perfluorocarbon droplets are to be more stable than ultrasound contrast agents, while offering the same effects after vaporization, such as echogenicity and membrane opening, as well as being used as drug carriers with the drug delivery be induced by ADV. However, ADV is far to be understood. In this work, we investigated the acoustic pressure threshold at which the vaporization of liquid perfluorohexane (PFH) occurs for three systems produced by microfluidics: plain PFH droplets, PFH droplets containing many nanometric water droplets and droplets made of a PFH corona encapsulating a single micrometric water droplet. We used a transducer emitting acoustic pulses at a frequency of 1.1 MHz and a pressure amplitude below 5 MPa. The probability to observe a vaporization event was measured as a function of pressure. As our experiments were performed on solutions of droplets, we developed a statistical model to extrapolate, from our experimental curves, the ADV pressure thresholds in the case where only one droplet is insonified. We observed that the value of this ADV pressure threshold decreases as the radius of the plain PFH droplets increases. This value was further reduced when PFH droplets encapsu-

---

[*] Authors contributed equally

Preprint submitted to Elsevier

late a micrometric water droplet, while the encapsulation of many nanometric water droplets did not modify the threshold. This behavior is not due to superharmonic focusing or homogeneous nucleation. It can be explained by the fact that the vaporization event is induced by heterogeneous nucleation. In the case of PFH droplets containing water, the nucleus leading to vaporization can appear either on the external surface (PFH droplet) or on the internal surface (*i.e.* the surface of the water droplets encapsulated into the PFH droplet). Our results suggest that vaporization is due to a nucleus appearing on the internal surface when the water droplet radius is micrometric, but on the external surface for nanometric water droplets. Finally, the theoretical model of heterogeneous nucleation is not accurate to predict our data as it is based on the assumption that the surface, on which the nucleus appears, is rigid, while the surface of our droplet shell is flexible.

Keywords: Acoustic Droplet Vaporization, Perfluorohexane, Droplets, Double emulsions

1. Introduction

Perfluorocarbon (PFC) oils have been studied as candidates for the formulation of drug delivery systems in the formulation of emulsion droplets and used as blood substitutes due to their high oxygen solubility[1]. PFC liquids are inert, highly stable in the body due to their lipo- and hydro-phobicity, and can circulate for two hours [2], which is considerably more than the PFC microbubbles commonly used as contrast agents [3]. The PFC drug carriers thereby enhance the therapeutic index of the carried drug by: offering a protection from drug degradation, allowing a targeted accumulation, enabling a long-term drug release, and increasing bioavailability [4]. Moreover, liquid PFCs possess a phase change ability: subjecting PFC droplets to sufficient acoustic energy triggers a liquid-to-vapor transition, called Acoustic Droplet Vaporization (ADV) [5]. The therapeutic potentials of ADV have been exploited for various applications including embolotherapy, phase aberration correction [6, 7], and high-intensity focused ultrasound (HIFU) therapy [8, 9, 10, 11, 12]. The understanding of the ADV mechanism is currently an active research domain. The growth of a vapor nucleus excited by ultrasound has been successfully modeled [13] and compared to optical observations [14, 15]. However, ADV is far from being fully grasped yet. Individual droplets cannot be detected optically in the nanometric range, thus drastically limiting direct observations. The droplet size plays a role, with lower pressures required for larger droplets [8, 16]. Nanosecond imaging of a series of experiments on the ADV process with micron-sized PFC droplets [17], has established that a nonlinear distortion of the acoustic wave prior to hitting the droplet, combined with the droplet-induced focusing of the wave, are responsible for the initiation of acoustic vaporization. This effect is all the more efficient as the droplet is large, thus explaining in part the radius dependence for large droplets (larger than 6 µm for PFP droplets at 3.5 MHz). However, this effect fades out for increasingly small particles, which can not play anymore the role of acoustic lenses, even though they require more and more intense pressures. These assumptions have led to the characterization of ADV into two distinct regimes: nucleation and growth of the vapor bubble during ultrasound exposure; and a continued growth of the vapor bubble even after the ultrasound exposure is terminated [17]. These regimes sum up the fate of a droplet following ADV. Microscopic voids formed during the rarefactional phase of an acoustic pulse, serve as the seeds required to facilitate the transformation of the liquid into a vapor bubble once sufficient acoustic energy is supplied. Similar observations reported in related studies [18, 13, 19] have further enhanced the validity of this model.

A recent study has brought to light yet another puzzling behavior of ADV. A nucleation map constructed from ultra-high speed imaging displayed bubbles with nucleation spots at random positions throughout the droplet [15]. This makes one wonder if these localized spots were indeed a function of the droplet size. Finally, the decrease of the threshold pressure with increasing droplet size [20, 21] remains theoretically unexplained. This lack of in-depth knowledge severely limits the tuning of applied physical stimuli to better serve the drug delivery and the utility of PFC-based emulsions as stimuli responsive devices.

In order to gain a better knowledge in ADV we have investigated three types of droplets which allow to vary the external (concave) and internal (convex) surface area in contact with perfluorocarbon:

1. Plain PFH droplets surrounded by a monolayer of a homemade fluorinated surfactant;
2. Water multi-core PFH droplets, similar to (1) but containing in their core nanodroplets of water surrounded by a surfactant shell ensuring their dispersion in the PFH;
3. Water single-core PFH droplet, similar to the previous one but with a single water microdroplet instead of several water nanodroplets.

For these three types of emulsions, we have determined the variation of the ADV threshold with the droplet size, as well as with the volume fraction of water trapped in the PFH.

2. Materials & methods

2.1. Materials

Unless otherwise stated, all chemicals were used without further purification and all solutions were filtered using Acrodisc® Syringe Filters (from PALL) with a pore size of 0.2 µm. All aqueous solutions were made using Milli-Q IQ 7000 Type-1 water Purification System. Methanol and NaCl were obtained from Sigma Aldrich. PDMS Sylgard 184 was purchased from Neyco. Photoresist SU8 was purchased from Chimie Tech Services. Silicon wafers were obtained from BT Electronics. The pressure controllers (model MFCS–EZ) used to inject the fluids into the microfluidic chips were purchased from Fluigent. The tubing connecting the pressure controllers to the microfluidic chip was bought from

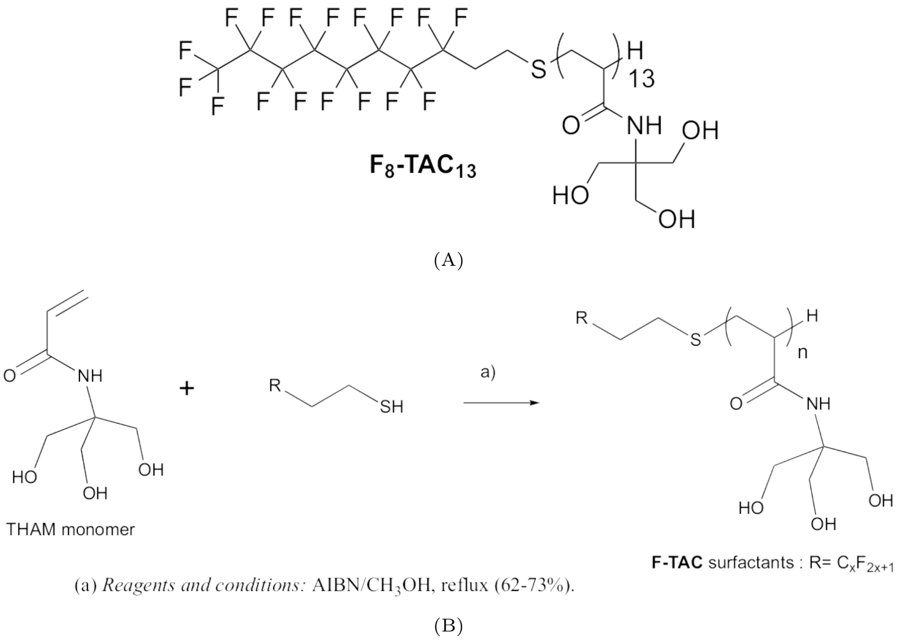

Figure 1: (A) Chemical structure of F_8-TAC_{13} surfactant. (B) General synthetic pathway of F–TAC surfactants (reagents and conditions: AIBN/CH_3OH, reflux 62-73%).

VWR (Internal diameter: 0.51 mm, External diameter: 1.52 mm). The channel inlets and outlets were punched with a 0.35 mm biopsy punchers delivered by World Precision Instruments (WPI); while the plasma cleaner was purchased from Harrick Scientific.

The perfluorohexane PFH and the fluorinated surfactant, Krytox 157 FSL, were purchased respectively from ABCR GmbH and Chemours.

2.2. Synthesis of F-TAC surfactant

F–TAC surfactants are amphiphilic molecules composed of two structural units (Fig. 1A). One unit is the polar head, made of a water-soluble oligomer of Tris(hydroxymethyl) aminomethane (Tris). The second is the fluorinated tail. Its length can be tuned according to the concentration of starting reactants and conditions carried out for their synthesis. F–TAC surfactants are readily available at the gram scale in one step by free radical polymerization of the tris(hydroxymethyl) acrylamidomethane (THAM) monomer according to the reaction shown in Fig. 1B [22].

Within a perfluorocarbon emulsion, the F–TAC polar head is located at the surface of perfluorocarbon droplets, in contact with water, while the fluorinated tail acts as a fluorophilic anchorage ensuring the stabilization of PFH droplets. In order to ensure an optimal droplet stabilization and water solubility, the F–TAC used in the current study is made of a fluorinated tail with eight fluorinated carbons and endowed with thirteen Tris units, and will be named "F_8-TAC_{13}" surfactant.

2.3. Interfacial tension

The interfacial tension between water and PFH liquid was measured with an error of 2 mN/m using a Tracker tensiometer (Teclis, France) at 20 ℃. The tensiometer analyzes the shape of a pendant PFH drop in water, using the Young–Laplace equation to derive the interfacial tension. During the experiment, the water drop volume was kept constant at $6\,\mathrm{mm}^3$ in the absence of a surfactant and at $2\,\mathrm{mm}^3$ when the water contained 0.1%wt F_8TAC_{13} or when the drop contained 5% Krytox 157 FSL (the percentage used in all formulations). We waited until the interfacial tension reached an equilibrium value to extract the interfacial tension value. As a control test, we measured the interfacial tension of a sessile air bubble in water: a value of 71.9 mN/m was measured.

2.4. Droplet Generation and Characterization

2.4.1. Microfluidic chip fabrication

We manufactured two types of chips. The first one, suitable for the production of either plain PFH droplets or water multi-core PFH droplets, uses a single classic flow-focusing chip (top and middle figures in Fig. 2). In these chips, all channels are 50 µm deep and 100 µm wide, while the nozzle size is 10 µm.

The second type of chips was used for the production of water single-core PFH droplets and is made of two flow-focusing junctions in series inside one chip as shown in bottom figure of Fig. 2. For this chip, all channels are 50 µm deep and 100 µm wide, the nozzle sizes are 35 µm (first nozzle) and 70 µm (second nozzle).

Both chip types were first designed on AutoCAD, then printed using a two-photon polymerization printer, a Nanoscribe GT Photonic Professional device, with a negative-tone photoresist IP-S (Nanoscribe GmbH, Germany) and 25× objective, directly on silicon substrates after a nitrogen plasma cleaning preparation (to increase the resin adhesion on the substrate). To reduce printing time, a shell writing strategy was applied. It consists of fabricating a dense shell delimiting the structure, the inner being only partly polymerized in the form of a scaffold. After developing in propylene glycol methyl ether acetate (30 min) and isopropanol (5 min), a batch polymerization is performed with UV-exposure. Soft lithography was then used to replicate the channels. PDMS and its cross-linking agent were mixed at a ratio 10:1 (wt/wt), degassed and poured onto the mold. The polymer was cured for 2 hours at 70 ℃. PDMS chips were then peeled off carefully from the mold, and 350 µm holes were punched into the chip with biopsy punchers to create inlets and outlets. Once the design was etched onto the PDMS, activating the patterned surface of the chip sealed the microfluidic chip and that of a glass slide for 1 min in a plasma cleaner filled with air and at a power of 18 W. This plasma activation ensures the secure bonding of the chip on the glass slide. The walls of the single flow-focusing junction chip were treated hydrophilic. To do this the chip was plasma activated for 1 minute and water was passed through the channels.

2.4.2. Production of plain PFH droplets

We used two distinct processes to generate perfluorohexane droplets depending on their diameter d. In both processes, the mass ratio of F–TAC to continuous aqueous phase was 0.1%.

Plain PFH droplets with a diameter $d < 1\,\mu\text{m}$ were produced using a high-pressure homogenizer (model LV1 from Microfluidics). For this technique, a coarse emulsion was first prepared by vortexing. The coarse emulsion was then used with the high-pressure homogenizer, where the emulsion went at a high velocity (thanks to a high pressure pump) through two capillaries which met inside a Y shape chamber (model F12Y, internal dimension of 75 µm). The high shear forces occurring in this chamber between the two emulsion flows induce a reduction in droplet size. The passage through the chamber is repeated 8 times at a pressure of 138 MPa. The resulting emulsion was centrifuged at 6000 rpm (*i.e.*, at a relative centrifugal force of 2000 g) for 30 s using a bench mini-centrifuge (Mini Star from VWR) to force any droplets with $d > 1\,\mu\text{m}$ to sediment and only the supernatant was kept.

Plain PFH droplets with $d > 1\,\mu\text{m}$ were generated by microfluidics using a conventional single flow focusing chip with the following flow rates: 0.9-1 µL/min for the channel filled with perfluorohexane (white arrow in the top figure of Fig. 2), 2.5-8 µL/min for channel filled with the aqueous solution solubilizing F_8-TAC_{13} (orange arrows in the top figure of Fig. 2).

2.4.3. Production of water single-core PFH droplets

These droplets were produced using a two-nozzle device (see Fig. 2). Following the procedure of Bodin-Thomazo *et al.* [23], the channel making the junction between the PFH and water channels (*i.e.*, channel C between channels B and D in Fig. 2), was selectively patterned using a black marker to avoid the wetting of the walls by the PFH. We used a flat PDMS layer as a substrate for the chip instead of a glass slide. This was followed by the surface treatment procedure previously explained (air plasma for 1 min). After the treatment, the chip and the flat PDMS were aligned to fit the marker pattern. In this chip, the walls of the unpatterned channels remain hydrophilic, while the walls of the patterned channel are kept hydrophobic. The chip was flushed with methanol and flushed with water for 20 minutes before starting the production of droplets. Then, the different fluid phases (PFH and aqueous solutions) were injected into the microfluidic device by applying a pressure of 20 mbar to the headspace of their respective inlets. The flow rates were adjusted to encapsulate exactly one water droplet in each double emulsion within these ranges: 0.8-2.3 µL/min for the dispersed aqueous phase (orange arrow in channel A in the bottom figure of Fig. 2), 1-5.5 µL/min for the intermediate PFH phase (white arrows in channels B), and 2-8 µL/min for the continuous aqueous phase (orange arrows in channels D).

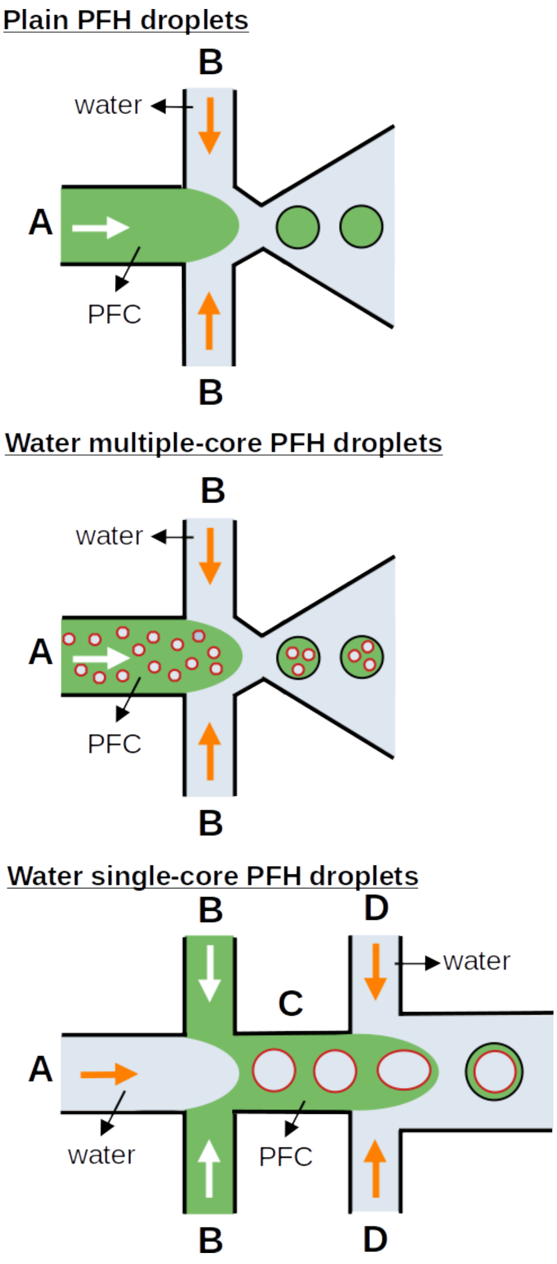

Figure 2: Schematic representation of one- (top and middle schemes) and two-nozzle (bottom scheme) microfluidics chips used to produce respectively plain PFH droplets, water multiple core PFH droplets and water single-core PFH droplets. The green and blue colors filling the channels are for perfluorohexane and water, respectively. The black line around droplets indicates the presence of F_8TAC_{13} surfactant, while the red line indicates the presence of Krytox surfactant.

2.4.4. Production of water multi-core PFH droplets

A coarse emulsion of water in PFH was first produced inside a vial from a mixture of normal saline (0.9% wt NaCl), PFH, and Krytox (5% wt). The ratio of normal saline to PFH was adjusted depending on the desired water volume fraction inside a multi-core droplet. The coarse emulsion was obtained by sonication using a Branson digital Sonifier (model 450) with a double step microtip at a frequency of 20 kHz, 30% of maximum amplitude for a pulse of 5 seconds, and 10 seconds pause, for 2 minutes. During sonication, the vial containing the fluids was immersed in an ice-water bath to avoid the vaporization of PFH due to the heating generated during the process. An emulsion made of normal saline nanodroplets surrounded by Krytox and dispersed in the PFH was thus produced.

In the next step the multi-core droplets were generated in the same flow-focusing chip as the one used for a plain droplet generation, with the primary nanoemulsion as the dispersed phase. The resulting multi-core droplet therefore consists of multiple aqueous nanodroplets inside a larger PFH droplet surrounded by water. We define φ_w as the volume fraction of water composing a droplet and d_w the mean diameter of the water droplets encapsulated inside the PFH droplets.

The flow rates used to produce these emulsions are in the same ranges as the ones used for plain PFH droplets.

2.4.5. Size and polydispersity measurements

The size and polydispersity of the microdroplets were estimated from a series of videos taken with an ultra-fast camera (Model SC1, Edgertronic, USA) during their production. The collected recordings were treated with an in-house MATLAB program. The code uses a Circular Hough Transform based algorithm for locating the droplets and then estimating their diameter along with the polydispersity index (PDI). This approach was chosen owing to its robustness in the presence of noise, occlusion and varying illumination. An example is given in Fig. S.1 for water single-core droplets where the inner radius (R_w) and outer radius (R) diameter were extracted using MATLAB. The water volume faction φ_w was derived from R_w and R for water single-core droplets.

For nanodroplets of PFH in water stabilized by F–TAC (*i.e.* plain PFH droplets) and nanodroplets of water in PFH stabilized by Krytox (*i.e.* water droplets that are later encapsulated into PFH droplets), their size and polydispersity were determined by dynamic light scattering. The measurements were performed on emulsions diluted 100 times, using an ALV/CGS-3 platform based goniometer system (from ALV GmbH), at room temperature. An experiment consists of measurements of the same solution at scattering angles, θ, ranging from 50° to 160°, with a step of 10°. At each angle θ, the device provides the decay rate $\Gamma_\theta = q^2 \frac{k_B T}{6\pi\eta R}$, where k_B is the Boltzmann constant, T is the temperature in K, η is the viscosity of the solvent, and $q(\theta) = (4\pi n_s/\lambda)\sin(\theta/2)$ is the magnitude of the scattering vector. The refractive index of the solvent is $n_s = 1.33$ and $\lambda = 633$ nm is the laser wavelength. A fit of the curve by the

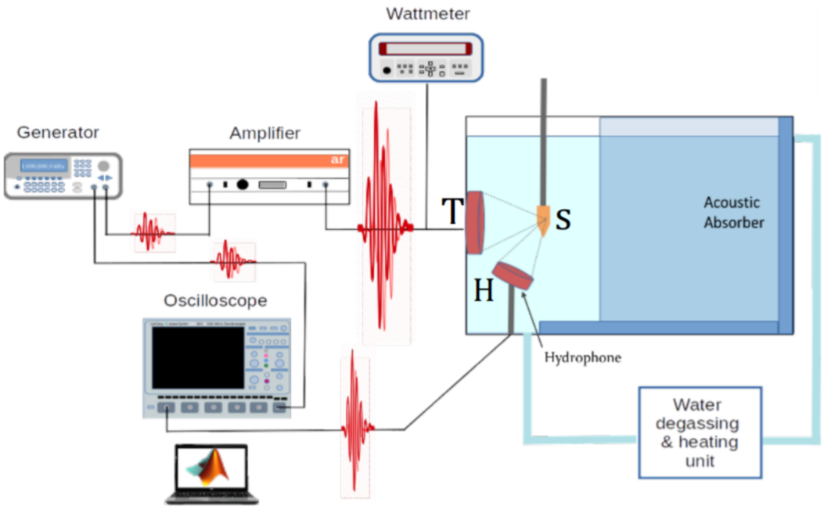

Figure 3: Experimental setup for ADV and measuring cavitation. A 1.1 MHz transducer (T) vaporized the droplets while the hydrophone (H) recorded at 0.55 MHz the scattered emissions due to subharmonic response of vapor micro bubbles in the sample (S).

cumulant method made it thus possible to determine the hydrodynamic droplet mean radius R along with the polydispersity index PDI [24]. A typical example of Γ_θ versus q^2 plot is presented in Fig. S.2 for plain PFH droplets which exhibit a diameter of 149 nm.

2.5. Acoustic droplet vaporization experiments

2.5.1. Acoustic setup

Fig. 3 sketches the ultrasonic setup triggering the ADV. A waveform generator (Model 33220A from Agilent) generates an electrical signal, that first goes through a radio-frequency power amplifier (Model 150A100C from AR France), and then through a power reflection meter (Model & NRT from Rohde Schwarz) measuring the delivered average electrical power. The electrical signal is converted into an acoustic wave by a focused transducer (Model H-101-G from Sonic concepts Inc.), whose fundamental mode is at 1.1 MHz. The acoustic wave propagates into a water tank thermostated at 20 ± 0.2 °C and connected to a degassing machine (Model WDS-1005 from Sonic Concepts). A PCR tube, filled with 200 µL of sample, is placed at the transducer focus. A hydrophone (model Y-107 from Sonic Concepts), whose focus overlaps with the transducer's inside the tube, continuously monitors the emitted signal.

The positioning of the PCR tube at the transducer focus was performed using a 0.2 mm needle hydrophone (from Precision acoustics) placed inside an open tube where the transducer emitted long and low intensity acoustic pulses. This was achieved by monitoring the signal amplitude recorded by the hydrophone.

The tube/hydrophone position was varied thanks to x-y-z motored stages and we selected the position corresponding to the maximum amplitude recorded by the hydrophone to place the tube at the focal point.

In addition, we used a Fabry-Pérot fiber-optic ultrasonic hydrophone (Precision Acoustics, Dorchester, UK) for the measurement of temperature [25]. In our case, temperature variations never exceeded 0.5 °C at the applied pressures.

2.5.2. Acoustic parameters

The signal consisted of sine-wave bursts at fundamental frequency 1.1 MHz. We employed short bursts of 5-cycles sine wave gated by a rectangular window of 91 µs pulses at an interval of 3 seconds to allow sufficient time to record the output. To subsidize any thermal effects we fixed the duty cycle at 5% and a pulse repetition frequency at 11 kHz. The total time of insonation was 7 min. Acoustic pressures varied from 0.3 to 7 MPa.

2.5.3. Samples preparation

Due to their high density, the droplets sediment quickly when dispersed in water. In order to guarantee a homogeneous dispersion of the droplets during the duration of the experiment, glycerol was chosen as the bulk phase because of its viscosity of 11.1 mPa s.

The samples were prepared by taking for instance $v = 0.1\,\mu\mathrm{L}$ at the bottom of a solution of droplets in water (so that the pipetted volume is mostly made of droplets) and by dispersing it in a volume of 200 µL of degassed glycerol in a PCR tube. In this case, the volume fraction of droplets was approximately $\varphi_d = 5 \times 10^{-4}$. Other values of φ_d were obtained by varying the volume v of droplets added to the 200 µL of glycerol. To ensure a homogeneous distribution of the droplets before each experimental test, the tube was vortexed at 2000 rpm for 30 s. Table 2 lists the different sizes and the corresponding numbers of droplets dispersed in 200 µL of glycerol solution. A solution of fresh droplets was prepared before each experiment.

2.5.4. ADV signal processing

The method of measuring the ADV threshold is based on the principle that microbubbles (*i.e.*, vaporized droplets) are much more powerful acoustic sources than liquid droplets because of the high compressibility of gases compared to liquids [26, 27]. When excited at a given frequency f_0, a bubble oscillates at this same frequency, but also at the subharmonic $f_0/2$ [28], and at higher harmonics if_0 (where i is an integer larger than 1). However, higher harmonics if_0 can also appear due to the non-linear propagation of an acoustic wave [29]. Hence, the appearance and magnitude of the subharmonic peaks at half the fundamental frequency, here $f_0/2 = 0.55\,\mathrm{MHz}$, was used as the most relevant indicator to detect the onset of ADV.

For instance, Fig. S.3.A displays the signal emitted by a glycerol solution containing plain PFH droplets with a radius of 20 µm that were insonified by a sound wave of amplitude 2 MPa, sufficient to trigger ADV. This is evidenced by the magnified level of the subharmonic at 0.55 MHz (grey solid line) in

Fig. S.3.B compared to pure glycerol (black dotted line). However, a basic observation of the subharmonic alone is not a definitive indication of ADV. For example, the initial subharmonic spikes in the droplet sample, as opposed to the glycerol response seen in Fig. S.3.B, could also be due to acoustic scattering caused by droplets (though these ones are expected to behave mostly linearly), and not necessarily bubble formation. Therefore, we used two different, more refined, quantification methods to determine the ADV threshold.

To compare the two methods and check their reproducibility, three different samples were used for each experiment. For each sample, the amplitude of the emitted signal was progressively increased, by increments of 25 mV at the waveform generator. For each increment, the pressure wave scattered by the droplets was collected by the hydrophone. 100 pulses were sent onto each sample, leading to the recording of 100 scattered signals which are stored for each pressure and each sample. During acquisition, the oscilloscope performed analog-to-digital conversion of the signal at a sample rate of 1 GHz. Once recorded, the Fast Fourier Transform (FFT) of each acquired signal was calculated using MATLAB. Therefore, the data points in the charts shown in this article are all averages over 300 FFT data.

***Method A*:** We extracted the magnitude of the subharmonic peak at $f_0/2$ from the FFT spectra of the signal emitted from a droplet sample at an applied acoustic pressure, P. The magnitude was then normalized by the excitation pressure, and the resulting value was plotted versus P. The data points were fitted using a piecewise linear function (see Fig. S.4). The pressure at the intersection point of the two linear fits indicated the ADV threshold [7, 30, 31].

***Method B*:** The differentiation between the presence and absence of bubble formation is made by taking the integral I of the Fourier Transform (IFT) in the subharmonic range between 0.4 and 0.6 MHz [6, 32] of the droplet sample $I_{\text{vap}}(P)$ and a control sample of glycerol $I_{\text{gly}}(P)$ containing no droplets, at each applied pressure. Vaporization occurrence at a particular acoustic pressure P was determined according to the criterion,

$$I_{\text{vap}}(P) \geq I_{\text{gly}}(P) + \zeta\sigma, \tag{1}$$

where ζ is an integer and σ is the standard deviation value of the values of $I_{\text{gly}}(P)$, recorded from glycerol at pressure P, compared to its means value. Each time the condition in Eq. 1 was met, a vaporization event was counted. As the phenomenon is stochastic, its probability, p, was calculated by repeating the experiment 100 times at the same pressure value and for the same sample. The probability, p, of bubbles appearing, for a given pressure P and sample, was defined as the frequency of vaporization, *i.e.*, the sum of vaporization events observed divided by 100. This value was then averaged over three independent experiments using three different samples. The top curve in Fig. S.5 shows an example of values of p determined for plain PFH droplets (with $R = 20\,\mu\text{m}$), at various acoustic pressures, when using $\zeta = 7$.

The probability p to observe a vaporization event in a solution of n droplet is fitted by Eq. 28 given in the Appendix A.1 to obtain the value of $P_{0.5}^{(n)}$ (derived using Eq. 33). However, the determination of the $P_{0.5}^{(n)}$ value depends on the value chosen for ζ [6]. The bottom curve of Fig. S.5 shows that the values $P_{0.5}^{(n)}$ changed according the choice of ζ. It is expected that when ζ is low, fluctuations of the background, at $f_0/2$, may contribute to the events ascribed to vaporization, which is introducing a bias in $P_{0.5}^{(n)}$ determination. In contrast if ζ is large, we may fail to detect vaporization events. The calculated effective $P_{0.5}^{(n)}$ doubled when ζ increased from 3 to 5. Variation with ζ of effective $P_{0.5}^{(n)}$ were dampered between $\zeta = 7$ and 10 ($< 30\%$ change), suggesting that $\zeta = 7$ minimizes the bias.

3. Results and Discussion

3.1. Cavitation pressure threshold in glycerol

The pressure threshold that induces cavitation in pure glycerol was evaluated in the absence of droplets. In these experiments, all glycerol solutions were vortexed at a speed of 2000 rpm for 30 s before measurements. Using the Method A described in section 2.5.4, we measured the normalized subharmonic peak amplitude of the acoustic signal of pure glycerol for an acoustic peak negative pressure increasing from 1 up to 5.2 MPa, as shown in Fig. S.4B. In these experiments, a different glycerol solution was used for each measurement. We observe from Fig. S.4B that cavitation starts to occur above 4.5 MPa in pure glycerol. In the following experiments, all of our measurements were performed at a pressure smaller than 4.5 MPa, hence in the absence of cavitation occuring in glycerol.

3.2. Vaporization pressure threshold of droplet solutions

A vaporization event is a stochastic phenomenon, thus an appropriate model needs to be used to derive from the probability curve the vaporization pressure threshold for solutions where n droplets are insonified. To do so, we assumed that in a solution of droplets, each droplet vaporizes independently of the other with probability $p^{(1)}$. The number of vaporization events from n droplets is then given by a binomial distribution with parameters n and $p^{(1)}$, and the probability to observe at least one vaporization by (see Appendix A.1)

$$p_{\geq 1}^{(n)} = 1 - \left[1 - p^{(1)}\right]^n . \tag{2}$$

When n becomes large, $p_{\geq 1}^{(n)}$ is approximated by a minimal Gumbel distribution with location parameters $\mu^{(n)}$ and scale parameters $\beta^{(n)}$ (see Appendix A.1)

$$p_{\geq 1}^{(n)} \approx 1 - \exp\left[-e^{\left(\frac{P-\mu^{(n)}}{\beta^{(n)}}\right)}\right]. \tag{3}$$

The median of this distribution is $P_{0.5}^{(n)}$ and can be expressed as:

$$P_{0.5}^{(n)} = \mu^{(n)} + \beta^{(n)} \ln(\ln(2)). \tag{4}$$

In addition, it can be shown that if $p^{(1)}$, which is a function of P, is given by an integral Gaussian distribution with median $P_{0.5}^{(1)}$ (ADV pressure threshold when 1 droplet is insonified) and standard deviation $\sigma^{(1)}$, then $\mu^{(n)}$ and $\beta^{(n)}$ can be expressed as

$$\mu^{(n)} = P_{0.5}^{(1)} - \sigma^{(1)} d_n \tag{5}$$

and

$$\beta^{(n)} = \sigma^{(1)} c_n, \tag{6}$$

respectively, with

$$c_n = \frac{1}{\sqrt{2\ln(n)}} \tag{7}$$

and

$$d_n = \sqrt{2\ln(n)} - \frac{\ln(\ln(n)) + \ln(4\pi)}{2\sqrt{2\ln(n)}}. \tag{8}$$

By replacing the value of $\mu^{(n)}$ given by Eq. 5 in the Eq. 3 we obtain a relation between $P_{0.5}^{(n)}$ and $P_{0.5}^{(1)}$

$$P_{0.5}^{(n)} \simeq P_{0.5}^{(1)} - \sigma^{(1)} \left[d_n + c_n \ln(\ln(2)) \right]. \tag{9}$$

We used Eq. 3 to fit our probability curves determined from the insonation of n droplets. The fit allows us to derive either $P_{0.5}^{(1)}$ or $P_{0.5}^{(n)}$, *i.e.* the ADV pressure threshold when 1 or n droplets are insonified, when using respectively Eq. 5–8 or 4.

3.3. Interfacial tensions

Several interfaces are at play in our system, each of them characterized by an interfacial tension γ. Since some theories have shown that these tensions play a role in the vaporization event, we measured the values of interfacial tensions at equilibrium for all the configurations met in our droplet systems: interfacial tensions between liquid PFH and water (γ_{lw}), between gaseous PFH and water (γ_{gw}), and between gaseous and liquid PFH (γ_{gl}). They were measured in the presence of each surfactant, F–TAC or Krytox, employed to stabilize our droplet systems. All data displayed in Table 1 were measured at equilibrium, using droplets of millimetric size. The effective interfacial tension varies with the droplet radius according to Tolman [33]:

$$\gamma(x) = \frac{\gamma(\infty)}{1 - \frac{2\delta}{x}}, \tag{10}$$

where x is the radius of the droplet, $\gamma(\infty)$ is the interfacial tension for a flat interface (*i.e.* $x = \infty$), δ is the Tolman length, whose value is on the order of the Angström [34] (we used $\delta = 1\,\text{Å}$ in our calculations). According to this equation, the value of the interfacial tension greatly decreases for radii smaller than 200 nm, while it hardly changes for larger ones. In our experiments, we considered that we measured the values $\gamma_{lw}(\infty)$, $\gamma_{gw}(\infty)$, $\gamma_{gl}(\infty)$ and we used Eq. 10 to derive the effective tensions $\gamma_{lw}(x)$, $\gamma_{gw}(x)$, $\gamma_{gl}(x)$.

Interfacial tension	with F–TAC (mN/m)	with Krytox (mN/m)
$\gamma_{gl}(\infty)$	12	12
$\gamma_{lw}(\infty)$	25	18
$\gamma_{gw}(\infty)$	38	66

Table 1: Interfacial tensions between liquid PFH and air (γ_{gl}), liquid PFH and water (γ_{lw}), and air and water (γ_{gw}), where air has been taken as a replacement for gaseous PFH. The measurements were done in the presence of surfactant, either F–TAC or Krytox, at their maximum solubility. The error in the values is ±2 mN/m.

3.4. Plain PFH droplets

3.4.1. Choice of methods to determine ADV pressures

We performed measurement on solutions of plain PFH droplets with a radius of 20 µm. We used Method A and B to determine the value of $P_{0.5}^{(n)}$. Fig. S.4 shows that Method A gave a value of $P_{0.5}^{(n)} = 2.1 \pm 0.3\,\mathrm{MPa}$, which is at the point of intersection of the linear piecewise fit. While Method B yielded $P_{0.5}^{(n)} = 2.12 \pm 0.03\,\mathrm{MPa}$ as shown in Fig. S.5 from the fit of the data to Eq. 3 and the use of Eq. 4. Consequently, both methods gave similar ADV threshold values $P_{0.5}^{(n)}$. The error obtained by Method B was noticeably smaller than Method A and for this reason we used Method B to detect the probability of vaporizaton in the following experiments. Note that the number of detected vaporization events associated with the droplets is expected to be much smaller than the number of cavitation event occuring in glycerol. Thus, while the precision of Method A is adequate to detect cavitation in glycerol, the precision of Method B is more adapted for the detection of vaporization event.

3.4.2. ADV pressure threshold as a function of droplet number

We performed measurements on solutions made of plain PFH droplets whose radius was 20 µm. Then, we derived the ADV threshold for droplet volume fractions φ_d varying from 2.5×10^{-4} up to 50×10^{-4}. In these experiments, only the droplets located in the volume v_{focus} of the transducer focus may be vaporized. The volume v_{focus} is equal to 0.38 µL (determined at −6 dB according to the manufacturer specifications) and contained 3, 6, 11, 28, and 57 droplets when φ_d was equal to 2.5×10^{-4}, 5×10^{-4}, 10×10^{-4}, 25×10^{-4}, and 50×10^{-4}, respectively. We observe in Fig. 4A that the probability curves are shifted upon the addition of droplets. The value of $P_{0.5}^{n}$ determined for each curves using Eq. 4 and 6–8 correspond to the values of pressure at which $p = 0.5$. Fig. 4B shows the behavior of the values of $P_{0.5}^{n}$ as a function of the number n of insonified droplets. We observe that $P_{0.5}^{n}$ decreases as n increases. These results show that a comparison between measurements can be drawn only if they were performed at the same number of droplets. They also indicate that conclusions may be difficult to draw from a panel of experiments performed at an unknown number of droplets.

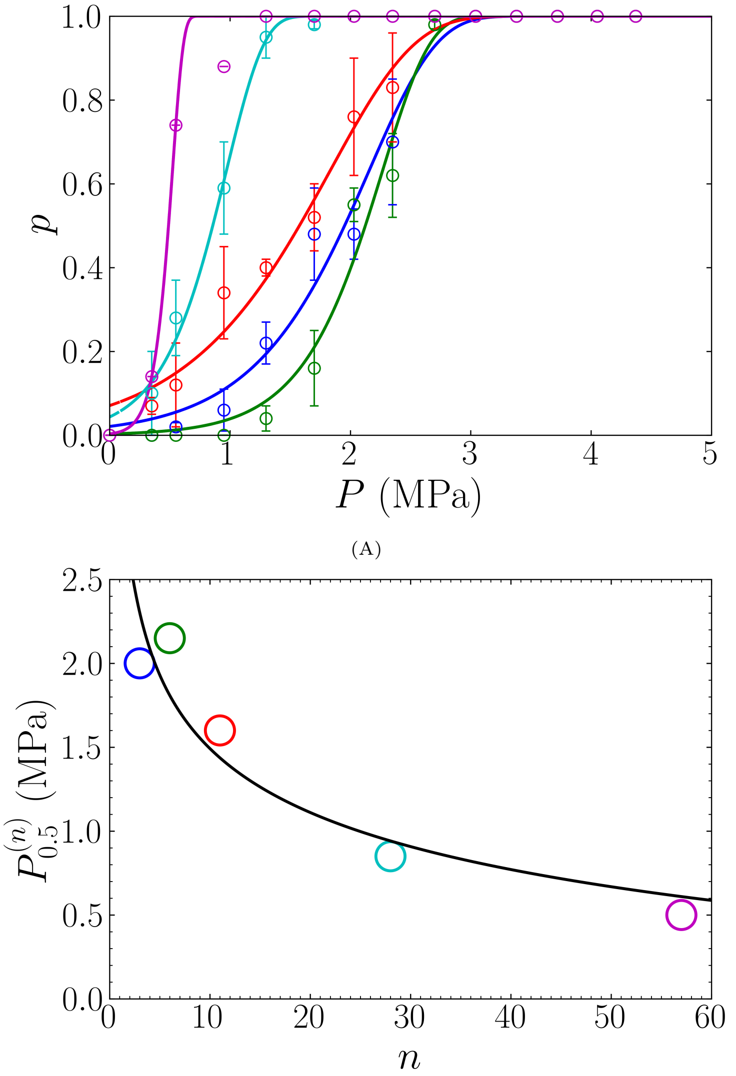

(A)

(B)

Figure 4: (A) All points represent the probability p to measure a vaporization event as a function of pressure for solutions containing droplets of radius 20 µm with various droplet volume fraction φ_d (see text), leading to a number of droplets in the transducer focus of 3 (○), 6(○), 11 (○), 28 (○), and 57 (○).The lines are fits performed using either Eq. 3 or 9, as there is no difference between the two fits. (B) The values $P_{0.5}^{(n)}$ obtained from the previous fit are plotted as a function of n, the number of droplets localized in the transducer focus. The line is a fit ($R^2 = 0.88$) using Eq. 9, 7, and 8, for which $P_{0.5}^{(1)} = 3.3 \pm 0.4$ MPa and $\sigma^{(1)} = 1.2 \pm 0.3$ MPa.

In addition, since models were developed to predict nucleation only in the case of one droplet, it is better to obtain the ADV pressure threshold in the case of only one insonified droplet. From our measurements, we could derive the value of ADV pressure threshold for the case of only 1 insonified droplet using two methods. In the first one, the $P_{0.5}^{(n)}$ values in Fig. 4B were fitted using Eq. 9. The fit gives the values $P_{0.5}^{(1)} = 3.3 \pm 0.4\,\mathrm{MPa}$ and $\sigma^{(1)} = 1.1 \pm 0.3\,\mathrm{MPa}$. In the second one, each p curves in Fig. 4A were fitted by Eq. 3 and Eq 5–8 were used to derive the $P_{0.5}^{(1)}$ values for each curve. The average value of $P_{0.5}^{(1)}$ for all curves except for the point corresponding to 57 droplets (magenta curve, for which a point is left out by the fit) lead to a value of $3.1 \pm 0.5\,\mathrm{MPa}$ and $\sigma^{(1)} = 1.0 \pm 0.3\,\mathrm{MPa}$. Consequently, both methods are equivalent in providing a value for $P_{0.5}^{(1)}$.

R (µm)	n_{tot}	n	$P_{0.5}^{(n)}$ (MPa)	$P_{0.5}^{(1)}$ (MPa)	σ^1 (MPa)
0.1	2.4×10^{10}	4.5×10^7	2.51 ± 0.02	8.5 ± 0.6	1.08 ± 0.11
2.5	1.5×10^6	2.9×10^3	2.42 ± 0.01	5.8 ± 0.2	0.86 ± 0.05
5	1.9×10^5	3.6×10^2	2.39 ± 0.01	4.9 ± 0.2	0.86 ± 0.05
20	2.9×10^3	6	2.12 ± 0.01	3.1 ± 0.1	0.75 ± 0.09
30	8.8×10^2	2	1.41 ± 0.01	1.5 ± 0.1	0.21 ± 0.01

Table 2: Results from experiments performed on a solution of PFH plain droplets dispersed in glycerol, at a droplet volume fraction $\varphi_d = 5 \times 10^{-4}$. R is the radius of the droplets, n_{tot} is the total number of droplets in the sample tube, while n is the number of droplets inside the acoustic focus volume (determined at −6 dB). $P_{0.5}^{(1)}$ and $P_{0.5}^{(n)}$ are the derived pressure at which the probability to observe a vaporization event is 0.5, when 1 or n droplets are respectively present in the acoustic focus volume. σ^1 is the standard deviation on the gaussian distribution having $P_{0.5}^{(1)}$ as a median

3.4.3. ADV pressure threshold as a function of droplet radius at a constant φ_d

Our next measurements were performed at a constant volume fraction of plain droplets, $\varphi_d = 5 \times 10^{-4}$, irrespective of the droplet radius. We studied solutions of droplets having a radius of either 0.1, 2, 5, 20 or 30 µm. As a consequence, the number of droplets n located in the volume of the transducer focus varied. We calculated it was respectively $n = 4.5 \times 10^7$, 2.9×10^3, 3.6×10^2, 6 and 2 droplets. For each radius, we determined the probability p to observe a vaporization event as a function of acoustic pressure P. From these probability curves, we evaluated $P_{0.5}^{(1)}$ and $P_{0.5}^{(n)}$, the acoustic pressures at which $p = 0.5$ when respectively, 1 and n droplets were insonified. The resulting values are displayed in Table 2 and Fig. 5.

From Fig. 5, we observe that the values of $P_{0.5}^{(1)}$ and $P_{0.5}^{(n)}$ are very different when n is large but they are converging to the same value for the largest droplet radius, where $n = 3$. It is notable that the values of $P_{0.5}^{(1)}$ decreases from 8.5 down to 1.5 MPa when the droplet radius increases from 0.2 to 30 µm. We would like to determine the reason of this dependence.

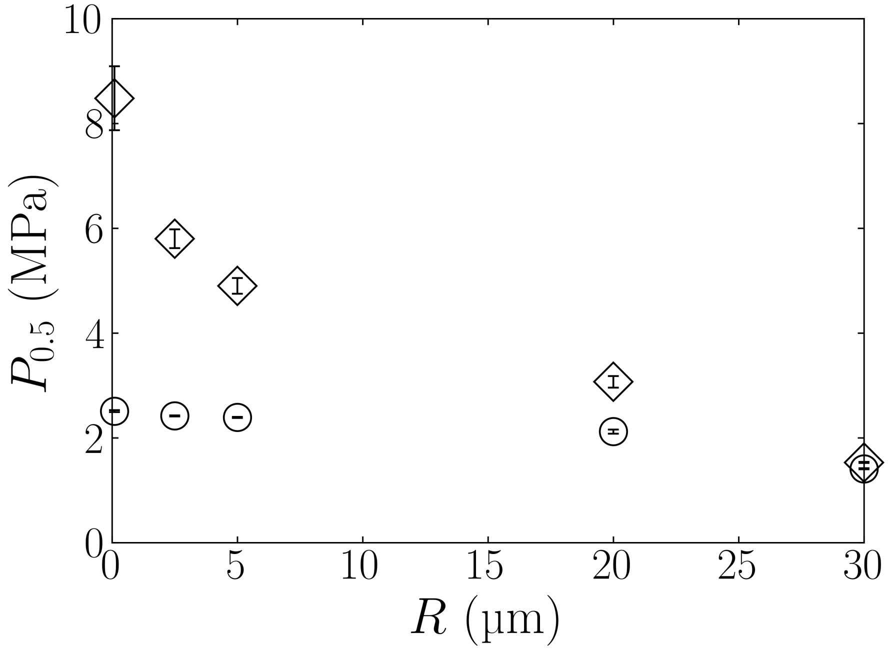

Figure 5: Values of $P_{0.5}^{(1)}$ ($\Diamond$) and $P_{0.5}^{(n)}$ ($\circ$) determined for solutions at constant volume fraction of droplets ($\varphi_d = 5 \times 10^{-4}$), with droplet radius varying from 0.1 to 30 µm.

From the literature, it has been suggested that a vaporisation event may be due to two main mechanisms. The first one, called superharmonic focusing [17], is due to the focalization of the harmonic part of the ultrasonic wave inside the droplet. The second one is due to a nucleation that spontaneously appears inside the droplet under the pressure wave. The nucleation can appear either in the droplet volume (*i.e.* homogeneous nucleation) or at the droplet surface (*i.e.* heterogeneous nucleation). Since each of these mechanisms has been mathematically described (for the case of one droplet), we can assess if these effects can account for the occurrence of vaporization in our experiments by trying to fit the values of $P_{0.5}^{(1)}$ in Fig 5.

Superharmonic focusing. We followed the procedure described by Shpak *et al.* [17]. We first used the software HIFU-beam Simulator [35] to evaluate the shape of the acoustic wave produced by our transducer in the absence of droplet. In this Matlab script, we used as input parameters, the frequency ($f = 1.1\,\mathrm{MHz}$), the geometric focus (63.2 mm) and radius (64.00 mm) of the transducer, as given by the manufacturer Sonic Concepts. The acoustic pressure wave was evaluated at the transducer focus and then fitted by a Fourier series

$$P_0(t) = \sum_{n=0}^{\infty} a_n e^{i(n\omega t + \phi_n)}, \tag{11}$$

where $\omega = 2\pi/f$, ϕ_n is a phase term, and a summation up to 10 was more than enough to fit the acoustic wave. We used the values a_n and ϕ_n to evaluate the contribution to the acoustic pressure P_d due to the presence of the droplet:

$$P_d(r,\theta,t) = \sum_{n=0}^{\infty}\sum_{m=0}^{\infty} a_n e^{i(n\omega t + \phi_n)} \alpha_{mn} j_m(nk_1 r) P_m(\cos\theta), \tag{12}$$

where j_m is the spherical Bessel function of the first kind of order m, P_m is the Legendre polynomial of order m, and

$$\alpha_{mn} = \chi_m \frac{j_m(x_0) h_m^{(2)'}(x_0) - h_m^{(2)}(x_0) j_m'(x_0)}{j_m(x_1) h_m^{(2)'}(x_0) - \frac{k_1\rho_0}{k_0\rho_1} h_m^{(2)}(x_0) j_m'(x_1)}, \tag{13}$$

where $\chi_m = (-i)^m(2m+1)$, $x_0 = nk_0R$, $x_1 = nk_1R$, and $h_m^{(2)}$ is the spherical Hankel function of the second kind of order m. Using Eq. 12, we looked at the moment where the pressure reached its minimum value inside the droplet. For all combinations of droplet radius and acoustic pressure tested in our experiments, we observed no superharmonic focusing. An example of curve snapshot is given in Fig. S.6 for the biggest droplet radius of 30 µm.

The lack of superharmonic focusing effect observed in our case is due the fact that our acoustic signal exhibits harmonics of too small amplitude. This results is in agreement with the data of Shpak *et al.* [17] who predicted a disappearance of the effect when the frequency decreases toward 1 MHz.

Homogeneous nucleation. In this mechanism, a nucleus can appear randomly inside the volume of the droplet of radius R. Once formed, the nucleus can either continue to grow and lead to the whole droplet vaporization, or shrinks and disappears. The fate of the nucleus depends on its radius r compared to a critical radius, $r^* = \frac{2\gamma_{gl}(r^*)}{P^*}$, for which the nucleus has equal chance to grow or to shrink. The nucleation energy $W^{\text{hom}}(r)$ required to obtain a nucleus of radius $r = r^*$ is (see Apendix A.2)

$$W^{\text{hom}}(r^*) = \frac{16\pi\gamma_{gl}^3(r^*)}{3P^{*2}}, \tag{14}$$

where P^* is the acoustic pressure inside the droplet that leads to a nucleus of size r^*. Since at r^* the probability of the nucleus to grow is $1/2$, the probability to obtain a vaporization of the droplet is also $1/2$. Consequently, we can write, taking into account the Laplace pressure

$$P^* = P_{0.5}^{(1)} + \frac{2\gamma_{lw}(R)}{R}. \tag{15}$$

Besides, the probability $q_{\geq 1}$ that at least 1 nucleus appears is given by (see Apendix A.4)

$$q_{\geq 1} = 1 - e^{-N(\tau)}, \tag{16}$$

where $N(\tau)$ is the average number of nucleus during a time τ and within a volume V. This can be expressed as $N(\tau) = JV\tau$. where J is the volumic rate of nucleation $J = J_0 e^{-\frac{W^{\text{hom}}(q_{\geq 1})}{k_B T}}$ and $J_0 = N_v\sqrt{\frac{2\gamma_{gl}}{M\pi}}$ [36] with M the mass of a PFH molecule and N_v the volume number of PFH ($N_v = \frac{N_A\rho}{M_w}$, where ρ and M_w are respectively the density and molecular weight of PFH, and N_A the Avogadro number). Consequently, we have

$$W^{\text{hom}}(q_{\geq 1}) = k_B T \ln\left(\frac{J_0 V\tau}{\ln\left(\frac{1}{1-q_{\geq 1}}\right)}\right). \tag{17}$$

A vaporization event will take place with a probability $p = 0.5$ at the condition that there is half a chance that at least a nucleus appears with a critical radius $r = r^*$, that is when $W^{\text{hom}}(r = r^*) = W^{\text{hom}}(q_{\geq 1} = 0.5)$. Thus, by equalizing Eq. 14 and 17, we can easily calculate the ADV pressure threshold using Eq. 15

$$P_{0.5}^{(1)} = \sqrt{\frac{16\pi\gamma_{gl}^3(r^*)}{3k_B T \ln\left(\frac{2\pi J_0 R^3}{3f\ln(2)}\right)}} - \frac{2\gamma_{lw}(R)}{R}, \tag{18}$$

where we made the replacement $V = \frac{4}{3}\pi R^3$ and $\tau = 1/(2f)$, as we suppose that the vaporization occurs during the half period where the acoustic pressure is negative. Since all parameters in Eq. 18 are known, we used it to estimate the values $P_{0.5}^{(1)}$ for various droplet radii. We calculated values that are larger than 12 MPa whatever the droplet radius, thus much larger than our experimental values of $P_{0.5}^{(1)}$ as shown in Fig. S.7. Smaller values could be predicted by decreasing the surface tension $\gamma_{gl}(\infty)$ of the nucleus surface down to 8 mN/m (instead of an experimentally measured value of 12 mN/m), but the calculation variation in $P_{0.5}^{(1)}$ is too small to fit our experimental data as shown in Fig. S.7.

We conclude that homogeneous nucleation is not the mechanism leading to droplet vaporization in our experiments.

Heterogeneous nucleation. The theory shows that a nucleation event may have more chance to occur on a surface than a volume. Indeed, the energy required to form a nucleus with a radius $r^* = \frac{2\gamma_{gl}(r^*)}{P^*}$ at a concave surface (with radius R, see Fig. S.8) is [37]

$$W^{het}(r^*) = W^{\text{hom}}(r^*)h(m_\theta, x), \tag{19}$$

where, for a concave surface, the function $h(m_\theta, x)$ is

$$h(m_\theta, x) = -1.5m_\theta x^2 + \frac{m_\theta x g}{2} - x^3 + x^2 g - \frac{g}{2} + \frac{1}{2}, \tag{20}$$

with $x = \frac{R}{r^*}$ and

$$m_\theta = \cos\theta = \frac{\gamma_{lw}(R) - \gamma_{gw}(R)}{\gamma_{gl}(r^*)}. \tag{21}$$

Since the function $h(m_\theta, x)$ is smaller or equal to 1, we have $W^{het}(r^*) \leq W^{\text{hom}}(r^*)$.

Following the approach used in the previous section, the average number of nucleus within a time τ and surface S is $N(\tau) = \Pi S\tau$, where Π is the surface rate of nucleation $\Pi = \Pi_0 e^{-\frac{W^{het}(q_{\geq 1})}{k_B T}}$ and $\Pi_0 = N^{2/3}\left(\frac{1-\cos\theta}{2}\right)\sqrt{\frac{2\gamma_{gl}}{\pi M}}$ [36]. In this case we have

$$W^{\text{het}}(q_{\geq 1}) = k_B T \ln\left(\frac{\Pi_0 S\tau}{\ln\left(\frac{1}{1-q_{\geq 1}}\right)}\right). \tag{22}$$

We equalize Eq. 19 and 22 with $q_{\geq 1} = 0.5$.

$$W^{\text{hom}}(r^*)h(m_\theta, x) - k_B T \ln\left(\frac{\Pi_0 S\tau}{\ln(2)}\right) = 0. \tag{23}$$

There is no analytical solution $P_{0.5}^{(1)}$ from this equation and one needs to solve it numerically. Using the values of surface tension of Table 1, we solved Eq. 23 to estimate the values of $P_{0.5}^{(1)}$ for a large radius range, but we found an important discrepancy between the experimental and predictive values as shown in Fig. S.7. However, it should be emphasized that the model of heterogeneous nucleation was developed on the assumption that the nucleus appears on a surface that is rigid. However, the surface of a plain PFH droplet is far from being rigid. We can expect the droplet surface to get locally modified by the presence of the nucleus. In such a case, the contact surface between the nucleus and the PFH droplet shell may exhibit a curvature $(1/r_2)$ smaller than the curvature ($1/R$) of the droplet shell. In such a case, the nucleus is made of two surface, one of radius r (interface between the liquid and gaseous PFH) and the other one (interface between water and gaseous PFH) is an effective radius r_2 smaller than R which reflects the deformation of the surface due to the nucleus presence. Under this assumption, we should now have

$$m_\theta = \frac{\gamma_{lw}(r_2)\cos\varphi - \gamma_{gw}(r_2)}{\gamma_{gl}(r^*)} \tag{24}$$

instead of Eq. 21 and most importantly Eq. 19 should be re-derived as it is no more valid within this new assumption.

To alleviate the problem, we made the assumption that the angle φ may be small enough so that $\cos\varphi \approx 1$. Under this assumption, we tried to solve Eq. 23 using the experimental values of $P^{(1)}_{0.5}$ to get the values r_2, with the constraint that $\cos(\varphi)$ should be given at the same time by equation 24 and by the following equation

$$\cos(\varphi) = \frac{r_2 - r m_\theta}{\sqrt{r_2^2 + r^2 + 2r_2 r m_\theta}}, \tag{25}$$

which is obtained from geometrical considerations [37]. Note that for a solid surface (i.e. when $r_2 = R$), $\cos\varphi$ is only defined by Eq. 25 as m_θ is defined by Eq. 21. Thus, we miminized Eq. 23 for various values of interface tensions ($20 < \gamma_{lw} < 30$, $5 < \gamma_{gl} < 17$, $20 < \gamma_{gw} < 40$). All these minimization gave values of r_2 that were used to calculate the difference in $\cos(\varphi)$ when using Eq. 24 and 25, that is

$$\Delta\cos(\varphi) = \frac{r_2 - r m_\theta}{\sqrt{r_2^2 + r^2 + 2r_2 r m_\theta}} - \frac{m_\theta \gamma_{gl}(r^*) + \gamma_{gw}(r_2)}{\gamma_{lw}(r_2)} \tag{26}$$

We chose the tuple of interface tensions that was the closest to the experimental values we measured, while giving the lowest difference in the value of $\Delta\cos(\varphi)$. Using this approach, the surface tensions $\gamma_{lw} = 29\,\mathrm{mN/m}$, $\gamma_{gl} = 6\,\mathrm{mN/m}$, and $\gamma_{gw} = 35\,\mathrm{mN/m}$ (instead of 25, 12 and 38 mN/m as experimentally measured) led to a difference in $\Delta\cos(\varphi)$ smaller than 0.04 for three smallest droplet radii, while the difference was larger than 0.7 for the two larger droplet radii. The derived values for r_2 were 0.66, 0.15 and 0.14 µm when the droplet radius was 0.5, 1.25 and 2.5 µm, respectively. Consequently, $r_2 \approx R$ for the smallest droplet size ($R = 0.5\,\mu\mathrm{m}$), which suggests that the droplet surface was not modified by the nucleus presence. However, the value r_2 was diverging from R for larger droplet radii and could not be derived for the two larger droplets (*i.e.* when $R = 20$ and $30\,\mu\mathrm{m}$). These results suggest that when the droplet is small, its surfactant shell is rigid enough (probably thanks to the overpressure inside the droplet, according to the Laplace equation) to prevent the nucleus from deforming it. In this case, the classical theory of heterogeneous nucleation applies. However, when the droplet is getting larger, its shell is becoming more flexible (as the overpressure vanishes), and the nucleus induces a (concave) deformation of the shell, with a radius r_2 that diverges from the droplet radius R. For the largest radii, 20 and 30 µm, the radius r_2 may be too different from R to comply with the assumption that $\cos\varphi \approx 1$ is small.

In conclusion, the model of heterogeneous nucleation can explain our data for small droplets (with a radius on the nanometric range) or for larger droplets by making the assumption that the nucleus curvature in contact with the droplet shell is different from the shell curvature. In the last case, the model is approximated and holds only when the two curvatures are not too different.

3.5. Water multi-core PFH droplets

To discriminate experimentally if heterogenous nucleation predominated in ADV, we studied vaporization in multiple emulsions, *i.e.* replacing plain PFH droplets by PFH droplets containing smaller internal water droplets. In the following experiments, the droplet volume fraction and droplet radius were constant, namely $\varphi_d = 5 \times 10^{-4}$ and $R = 20\,\mu\text{m}$.

3.5.1. ADV pressure threshold between water single-core and multi-core PFH droplets

We first compared two types of droplets with the same volume fraction of encapsulated water ($\varphi_w = 0.4$). The first type is made of a single water droplet (called water single-core PFH droplet) of radius $R_w = 10.5\,\mu\text{m}$. The second type comprises many water droplets (called water multi-core PFH droplet) of radius $R_w = 0.215\,\mu\text{m}$. For each droplet type, we measured the probability p to observe a vaporization event. The results are displayed in Fig. 6. From these curves, we derived the values $P_{0.5}^{(1)} = 1.9 \pm 0.1\,\text{MPa}$ ($P_{0.5}^{(n)} = 1.6 \pm 0.1\,\text{MPa}$) and $P_{0.5}^{(1)} = 3.0 \pm 0.1\,\text{MPa}$ ($P_{0.5}^{(n)} = 2.3 \pm 0.1\,\text{MPa}$) for the single and multi-core water droplets, respectively. The $P_{0.5}^{(1)}$ value for multi-core water droplets is identical to the value determined for plain PFH droplets of the same diameter, whereas the $P_{0.5}^{(1)}$ value for single water droplets is 1 MPa smaller.

As in the previous experiments with plain PFH droplets, the acoustic wave exhibited at the focus few high harmonics as the acoustic parameters remained the same. Consequently, no superharmonic focusing effect was expected in this more complex droplet system.

In addition, since the volume of PFH were the same in the two droplet types, the probability to obtain a nucleus leading to a vaporization event was expected to be identical. Indeed, Eq. 18 gives the same value for $P_{0.5}^{(1)}$ for both droplet systems, where V should be calculated from an effective radius of a sphere containing all the PFH comprised into the water single or multi-core PFH droplet.

Since only the surface area and the radius of the encapsulated water droplets was different between the two droplet types, we expect these differences to explain the variation in ADV pressure threshold. This can be explained in the framework of heterogeneous nucleation. Indeed, heterogeneous nucleation models were derived for concave surface (corresponding to the external droplet surface) [37] and convex surface (the water droplet surface in our case) [38].

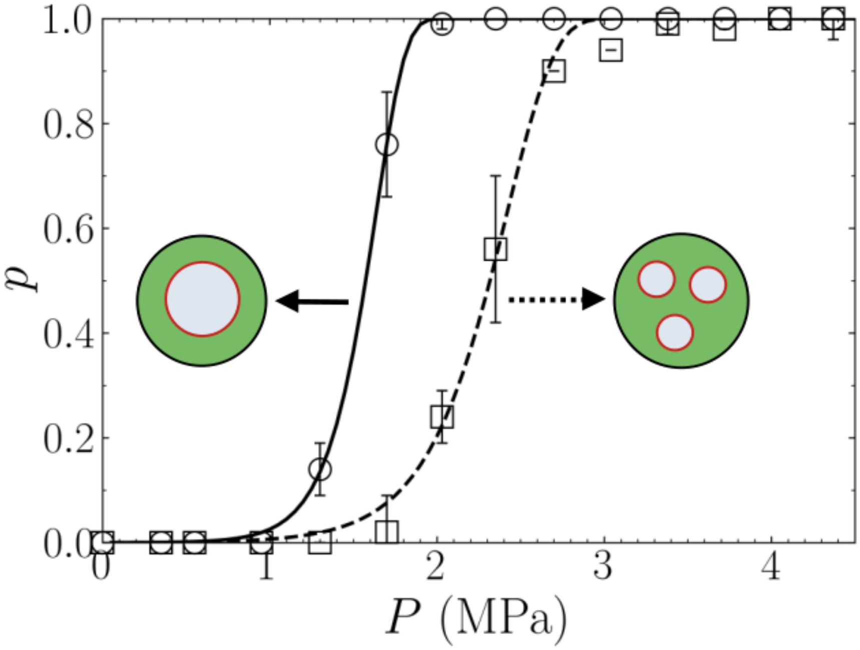

Figure 6: Probability to measure a vaporization event for water single-core (◯) and multi-core (□) PFH droplets, having a similar radius of $R = 20\,\mu\text{m}$ and the same water volume fraction ($\varphi_w = 0.4$). The experimental points are fitted by Eq. 3. The droplet radius R_w is $10.5\,\mu\text{m}$ for the water single-core PFH droplet and 250 nm for the water multi-core PFH droplet. The lines are the fits of the data using Eq. 3.

According to these models, a nucleus can appear either on the external droplet surface $S = 4\pi R^2$ or on the internal water droplet $S_w = 4\pi R_w^2$ and the energy to create a nucleus with critical radius r^* increases when the surface curvature increases. Consequently, for the case of water single-core PFH droplet, our results suggest that the vaporization is due to a critical nucleus that appears on the internal surface S_w. On the contrary, it is due to a critical nucleus appearing on the external surface S for the case of water multi-core droplets, as a consequence the value for ADV pressure threshold is similar to droplets of identical size and devoid of encapsulated water droplets.

3.5.2. ADV pressure threshold as a function of volume fraction of encapsulated water

If our previous explanation is correct, the ADV pressure threshold should not depend on the quantity of water droplets of radius 250 nm since a critical nucleation (i.e. leading to a vaporization event) will preferably occur on the external surface S. To verify this, we performed experiments for PFH droplets containing various concentrations of water droplets. The water volume fraction φ_w was ranging from 0.05 up to 0.8 and the values of $P_{0.5}^{(1)}$ was determined for each φ_w. The measured values are displayed in Fig. 7 along with the value for plain PFH droplets (where $\varphi_w = 0$) and the value for the water single-core shell droplet for which $\varphi_w = 0.4$. We observe that the values of $P_{0.5}^{(1)}$ are on average around 2.8 MPa (dotted line in Fig. 7) for the water multi-core PFH droplets, close to the value $P_{0.5}^{(1)}$ for plain PFH droplet. The observed variations may be due to the error made in estimating the fraction of droplets for each sample. Indeed, we used φ_d to estimate n as it intervenes in the fit through the number of droplets that are insonified.

4. Conclusion

We developed a statistical model that allows to derive the ADV pressure threshold at $p = 0.5$ for a single droplet from curves describing the probability p to observe a vaporization event in a solution of n droplets. We observed that the ADV pressure threshold $P_{0.5}^{(1)}$ decreases as the radius of the plain PFH droplets increases. The threshold $P_{0.5}^{(1)}$ can be reduced by encapsulating a micrometric water droplet, while the encapsulation of many nanometric water droplets does not induce a modification in $P_{0.5}^{(1)}$ compared to the case of plain droplets. We showed this behavior is not due to superharmonic focusing, nor to homogeneous nucleation. The observed vaporization can be explained by heterogeneous nucleation, indeed the probability to obtain a critical nucleus (i.e. a nucleus leading to vaporization with a probability $p = 0.5$) increases with increasing concave external surface S_{ext} (*i.e.* of the droplet radius R). In the case of PFH droplet containing water, the critical nucleus shall appear either on the external surface or on the convex internal surface (i.e. the surface of the water droplets of radius R_w). Our results suggest that the critical nucleus appears on the internal surface when the water droplet radius is of the micrometric size (10.5 µm). In contrast,

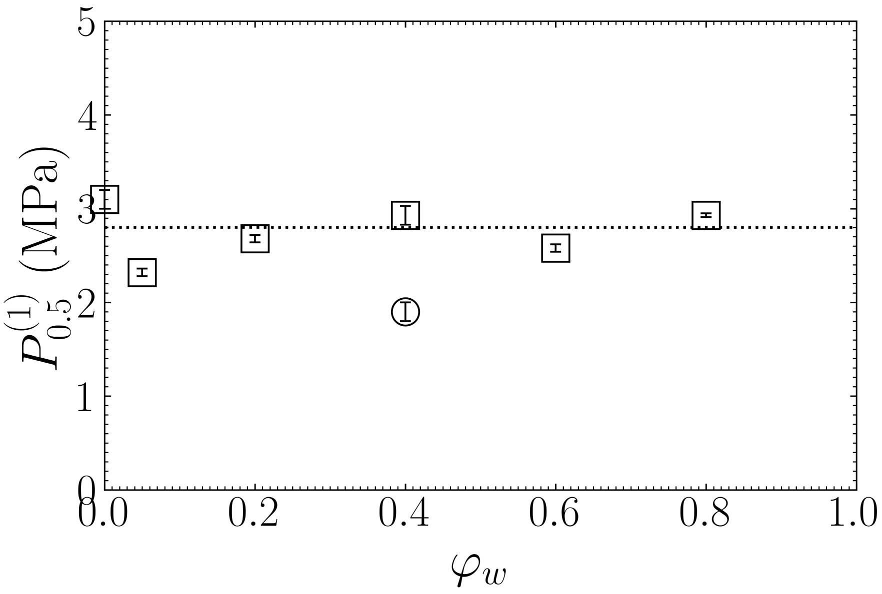

Figure 7: Composite emulsion: (W/PFH/W). Variation of the PADV threshold with the volume fraction of water droplets present in each PFH drop core. The water droplets, $\langle d_w \rangle = 0.43\,\mu\text{m}$, are stabilized by Krytox, and dispersed in PFH droplets ($d = 40\,\mu\text{m}$).

the critical nucleus is always appearing in the external surface when the water droplet is of the nanometric size (250 or 75 nm). We used an approximated model of heterogeneous nucleation as the current model used the assumption of a rigid surface, which is not the case in our system. In the future, a better understanding of droplet vaporization will require the development of a model of heterogeneous nucleation based on the hypothesis that the surface, on which a nucleus appears, is flexible.

CRediT authorship contribution statement

R. Ramesh: Conceptualization, Formal analysis, Investigation, Writing - original draft. **C. Thimonier:** Conceptualization, Investigation, Writing - original draft. **S. Desgranges:** Resources. **V. Faugeras:** Methodology, Writing - review & editing . **F. Coulouvrat:** Writing - review & editing. **J. Laurent:** Resources. **G. Marrelec:** Formal analysis, Writing - review & editing. **C. Contino-Pépin:** Resources, Writing - review & editing. **W. Urbach:** Conceptualization, Formal analysis, Supervision. **C. Tribet:** Supervision, Writing - review & editing. **N. Taulier:** Formal analysis, Supervision, Writing - review & editing.

Declaration of Competing Interest

The authors declare that they have no known competing financial interests or personal relationships that could have appeared to influence the work reported in this paper.

Acknowledgment

The authors acknowledge the funding from Plan cancer 2014-2019 (Project BubDrop4Glio). The Ph.D scholarship of C. T. was funded by ITMO cancer.

Appendix A

A.1. Extrapolating results from n droplets to 1 droplet

We assume that each droplet can vaporize independently of what happens with the other ones. Indeed, low droplet volume fractions were used to minimize interactions between droplets as well as between vaporization events. Under this assumption of independence, the probability to observe k vaporization events from the n droplets is given by the binomial distribution with parameters n and $p^{(1)}$. From this model, the probability to obtain no vaporization event is given by $\left[1-p^{(1)}\right]^n$, and the probability to observe at least one vaporization event by

$$p_{\geq 1}^{(n)} = 1 - \left[1-p^{(1)}\right]^n. \tag{27}$$

Note that for $p^{(1)}$ small and n large such that $np^{(1)}$ remains moderate, a good approximation of the binomial distribution is the Poisson distribution. In Eq. 27, $p^{(1)}$ is an increasing function of pressure P with values in [0,1], which we can express as $p^{(1)} = \Psi(P)$. If $\Psi(P)$ is considered as the cumulative distribution function (cdf) of a random variable X, then Eq. 27 shows that $p_{\geq 1}^{(n)}$ is the expression for the cdf corresponding to the minimum of n independent and identically distributed (i.i.d.) samples of X (Eq. 9.1.1 in [39]). Extreme value theory then shows that, when n becomes large, $p_{\geq 1}^{(n)}$ can only converge toward one of three types of distributions depending on $\Psi(P)$ (Section 10.5 in [40]). In particular, when $\Psi(P)$ belongs to specific families (including the normal, lognormal, maximal Gumbel, minimal Gumbel, maximal Weibull, and maximal Fréchet distributions), the limiting distribution for $p_{\geq 1}^{(n)}$ is the minimal Gumbel distribution with location parameter $\mu^{(n)}$ and scale parameter $\beta^{(n)}$ (Table 9.5 in [39]), i.e.,

$$p_{\geq 1}^{(n)} \approx 1 - \exp\left[-e^{\left(\frac{P-\mu^{(n)}}{\beta^{(n)}}\right)}\right], \tag{28}$$

Furthermore, given $\Psi(P)$, it is possible to provide an asymptotic expression for the parameters of the minimal Gumbel distribution as a function of n. For instance, if $\Psi(P)$ is given by the error function or, equivalently, an integral

Gaussian distribution, with median $P_{0.5}^{(1)}$ and standard deviation $\sigma^{(1)}$, then it can be shown that the parameters $\mu^{(n)}$ and $\beta^{(n)}$ can be expressed as

$$\mu^{(n)} = P_{0.5}^{(1)} - \sigma^{(1)} d_n \tag{29}$$

and

$$\beta^{(n)} = \sigma^{(1)} c_n, \tag{30}$$

with

$$c_n = \frac{1}{\sqrt{2\ln(n)}} \tag{31}$$

and

$$d_n = \sqrt{2\ln(n)} - \frac{\ln(\ln(n)) + \ln(4\pi)}{2\sqrt{2\ln(n)}}. \tag{32}$$

This result was obtained by combining the asymptotic result regarding the maximum in the case of a standard normal distribution (Example 3.3.29 in [41]), the relation between maximum and minimum (Section 3.1 in [41]) as well as the expression of a general normal distribution in terms of a standard normal distribution. Finally, the ADV corresponding to n droplets, which we denote by $P_{0.5}^{(n)}$ here to emphasize the dependence on n, is the median of the Gumbel distribution of Eq. 28, given by

$$P_{0.5}^{(n)} = \mu^{(n)} + \beta^{(n)} \ln(\ln(2)) \tag{33}$$

$$= P_{0.5}^{(1)} - \sigma^{(1)} \left[d_n - c_n \ln(\ln(2)) \right], \tag{34}$$

from Eqs. (24)–(27).

A.2. Homogeneous Nucleation

The work required to create a spherical gas volume, so-called nucleus, of radius r is

$$W^{hom} = \frac{4}{3}\pi r^3 \left(P_v - P\right) + 4\pi r^2 \gamma_{gl}, \tag{35}$$

where γ_{gl} is the surface tension of the nuclei surface (interface between gas and liquid), P_v is the saturated vapor pressure and P is the pressure amplitude developed in the liquid. The first term represents the free energy gain from converting liquid to gas, while the second term represents the energy cost of introducing an interface between the liquid and vapor phases. The first one is negative because the energy per unit volume of vapor is lower than the liquid one. Since the number of atoms that have changed from liquid to vapor varies as the cube of the radius r of the bubble, whereas the area of the interface varies as its square, the total energy first increases with increasing radius, reaches a maximum and then decreases. This maximum is reached at the critical radius r^*. Taking

$$\frac{dW^{hom}}{dr} = 0, \tag{36}$$

we find that (since $P_v \ll P^*$)

$$r^* = \frac{2\gamma_{gl}}{P^*}. \tag{37}$$

Inserting this value in Eq. 35 gives

$$W^{hom}(r^*) \approx \frac{16\pi\gamma_{gl}^3}{3P^{*2}}. \tag{38}$$

$W^{hom}(r^*)$ represents an energy barrier for vaporization: a nucleus with a size $r > r^*$ will spontaneously grow until the whole droplet becomes a bubble, otherwise it will be driven by thermodynamic forces to shrink.

A.3. Heterogeneous nucleation

If a nucleus appears at the surface of a droplet of radius R, this nucleus is then a spherical cap of radius r whose free energy of formation is:

$$W^{het} = \gamma_{gl}a_{gl} + (\gamma_{gl} - \gamma_{lw})a_{gw} + (P_v - P)v \tag{39}$$

where the subscripts l, g, and w refers to the liquid PFH, the gaseous PFH, and the water, respectively, v is the nucleus volume, γ_{ij} is the interfacial free energy per unit area between the phases i and j, which are separated by a surface area a_{ij}. The volume of the nuclei is thus enclosed inside a surface whose area is $a = a_{gl} + a_{gw}$.

For the case of a nuclei occurring on a convex surface of a dropet of radius R_w, Fletcher hypothesized that the critical radius r^* is identical to the homogeneous case [42] and found that the value of $W^{het}(r^*)$ is

$$W^{het}(r^*) = W^{hom}(r^*)h^{cnx}(m_\theta, x), \tag{40}$$

where

$$x = \frac{R_w}{r^*} \tag{41}$$

$$m_\theta = \cos\theta = \frac{\gamma_{lw} - \gamma_{gw}}{\gamma_{gl}} \tag{42}$$

and

$$\begin{aligned} h^{cnx}(m_\theta, x) = \frac{1}{2}\Bigg\{ & 1 - \left(\frac{m_\theta x - 1}{g^{cnx}}\right)^3 \\ & + x^3\left[2 - 3\left(\frac{x - m_\theta}{g^{cnx}}\right) + \left(\frac{x - m_\theta}{g^{cnx}}\right)^3\right] \\ & + 3m_\theta x^2\left(\frac{x - m_\theta}{g^{cnx}} - 1\right)\Bigg\} \end{aligned} \tag{43}$$

with

$$g^{cnx} = \sqrt{1 + x^2 - 2m_\theta x}. \tag{44}$$

Qian et al. demonstrated that this is the case by calculation [37] and extended the solution to a concave surface

$$W^{het}(r^*) = W^{hom}(r^*)h^{cnv}(m_\theta, x), \tag{45}$$

where

$$\begin{aligned} h^{cnv}(m_\theta, x) = \frac{1}{2}\Bigg\{ & 1 - \left(\frac{1+m_\theta x}{g^{cnv}}\right)^3 \\ & - x^3\left[2 - 3\left(\frac{x+m_\theta}{g^{cnv}}\right) + \left(\frac{x+m_\theta}{g^{cnv}}\right)^3\right] \\ & -3m_\theta x^2\left(1 - \frac{x+m_\theta}{g^{cnv}}\right)\Bigg\} \end{aligned} \tag{46}$$

and

$$g^{cnv} = \sqrt{1 + x^2 + 2mx_\theta} \tag{47}$$

The expressions for $h^{cnx}(m_\theta, x)$ and $h^{cnv}(m_\theta, x)$ can be rewritten in a simple form:

$$\begin{aligned} h^{cnx} = & -1.5m_\theta x^2 + \frac{m_\theta x g^{cnx}}{2} \\ & + x^3 - x^2 g^{cnx} + \frac{g^{cnx}}{2} + \frac{1}{2}, \end{aligned} \tag{48}$$

$$\begin{aligned} h^{cnv} = & -1.5m_\theta x^2 + \frac{m_\theta x g^{cnv}}{2} \\ & - x^3 + x^2 g^{cnv} - \frac{g^{cnv}}{2} + \frac{1}{2}. \end{aligned} \tag{49}$$

A.4. Nucleation probability

The stochastic nature of bubble nucleation on exposure to an acoustic wave leads us treat the formation of a nucleus in a given volume as a series of random events. The Poisson distribution law gives the probability q_m of forming exactly m nuclei within a time interval τ [43, 44], assuming they occur independently from one another:

$$q_m = \frac{N^m(\tau)^m e^{-N(\tau)}}{m!}. \tag{50}$$

Here $N(\tau)$ is the expected average number of nuclei created during the time interval τ. For instance, the probability to form exactly no nucleus is $q_0 = e^{-N(\tau)}$. The sum of all probabilities should be equal to 1:

$$1 = \sum_{i=0}^{\infty} q_i \tag{51}$$

Thus, the probability to create at least one nucleus is

$$q_{\geq 1} = 1 - q_0 = 1 - e^{-N(\tau)}, \tag{52}$$

which can be rewrite as

$$N(\tau) = \ln\left(\frac{1}{1-q_{\geq 1}}\right). \tag{53}$$

For homogeneous nucleation, the average number of nuclei occuring during a time τ and inside a volume V is related to the volume nucleation rate J through

$$N(\tau) = JV\tau, \tag{54}$$

while for heterogeneous nucleation, the average number of nuclei during a time τ and on a surface area A is related to the surface nucleation rate Π:

$$N(\tau) = \Pi A\tau. \tag{55}$$

The nucleation rates depends on the Boltzmann constant k_B, the absolute temperature T, and the energy barrier to be overcome W as follows. In the homogeneous case,

$$J = J_0 \exp\left(-\frac{W^{\mathrm{hom}}}{k_B T}\right), \tag{56}$$

where [36]

$$J_0 = N_A \rho \sqrt{\frac{2\gamma}{\pi M}}. \tag{57}$$

N_A is the Avogadro number, ρ the density and M the mass of a molecule (of PFH in our case). In the heterogeneous case,

$$\Pi = \Pi_0 \exp\left(-\frac{W^{\mathrm{het}}}{k_B T}\right), \tag{58}$$

where [36]

$$\Pi_0 = N^{2/3} \frac{1-\cos\theta}{2} \sqrt{\frac{2\gamma_{gl}}{\pi M}}. \tag{59}$$

The rate is null when $\cos\theta = 1$, *i.e.* when $\theta = 0$ (there is no nucleus) or π (the nucleus is not attached to the surface). Because of the exponential in nucleation rate, changes by several orders of magnitude in the values of J_0 and Π_0 only marginally affect the final results in nucleation rate.

We can thus relate the probability to create at least one nucleus to the rate of nucleation regardless the type of nucleation (homogeneous or heterogeneous) using Eq. 52 and Eq. 56 or 58, and leading to

$$q_{\geq 1} = 1 - e^{-\Omega\tau}, \tag{60}$$

where Ω is equal to either JV or ΠA depending on whether the nucleation is homogeneous or heterogeneous. The energy required to create at least one nucleus is thus

$$W(q_{\geq 1}) = k_B T \ln\left(\frac{\Omega\tau}{\ln\left(\frac{1}{1-q_{\geq 1}}\right)}\right). \tag{61}$$

References

[1] J. G. Riess, Oxygen carriers ("blood substitutes") - raison d'etre, chemistry, and some physiology. blut ist ein ganz besondrer saft, Chem. Rev. 101 (9) (2001) 2797–2920. `doi:10.1021/cr970143c`.

[2] N. Rapoport, K.-H. Nam, R. Gupta, Z. Gao, P. Mohan, A. Payne, N. Todd, X. Liu, T. Kim, J. Shea, C. Scaife, D. L. Parker, E.-K. Jeong, A. M. Kennedy, Ultrasound-mediated tumor imaging and nanotherapy using drug loaded, block copolymer stabilized perfluorocarbon nanoemulsions, J. Contr. Release 153 (1) (2011) 4–15, eighth International Nanomedicine and Drug Delivery Symposium. `doi:10.1016/j.jconrel.2011.01.022`.

[3] S. Sirsi, J. Feshitan, J. Kwan, S. Homma, M. Borden, Effect of microbubble size on fundamental mode high frequency ultrasound imaging in mice, Ultrasound Med. Biol. 36 (6) (2010) 935–948. `doi:10.1016/j.ultrasmedbio.2010.03.015`.

[4] H. Lea-Banks, M. O'Reilly, K. Hynynen, Ultrasound-responsive droplets for therapy: A review, J. Contr. Release 293 (2019) 144–154. `doi:10.1016/j.jconrel.2018.11.028`.

[5] L. J. Crouse, J. Cheirif, D. E. Hanly, J. A. Kisslo, A. J. Labovitz, J. S. Raichlen, R. W. Schutz, P. M. Shah, M. D. Smith, Opacification and border delineation improvement in patients with suboptimal endocardial border definition in routine echocardiography: Results of the phase iii albunex multicenter trial, J. Am. Coll. Cardiol. 22 (5) (1993) 1494–1500. `doi:https://doi.org/10.1016/0735-1097(93)90562-F`.

[6] M. L. Fabiilli, K. J. Haworth, N. H. Fakhri, O. D. Kripfgans, P. L. Carson, J. B. Fowlkes, The role of inertial cavitation in acoustic droplet vaporization, IEEE Trans. Ultrason. Ferroelectr. Freq. Control 56 (5) (2009) 1006–1017. `doi:10.1109/TUFFC.2009.1132`.

[7] M. Aliabouzar, K. N. Kumar, K. Sarkar, Effects of droplet size and perfluorocarbon boiling point on the frequency dependence of acoustic vaporization threshold, J. Acoust. Soc. Am. 145 (2) (2019) 1105–1116. `doi:10.1121/1.5091781`.

[8] O. D. Kripfgans, J. B. Fowlkes, M. Woydt, O. P. Eldevik, P. L. Carson, In vivo droplet vaporization for occlusion therapy and phase aberration correction, IEEE Trans. Ultrason. Ferroelectr. Freq. Control 49 (6) (2002) 726–738. `doi:10.1109/TUFFC.2002.1009331`.

[9] S. D. Sokka, R. King, K. Hynynen, MRI-guided gas bubble enhanced ultrasound heating in in vivo rabbit thigh, Phys. Med. Biol. 48 (2) (2003) 223–241. `doi:10.1088/0031-9155/48/2/306`.

[10] P. Zhang, T. Porter, An in vitro study of a phase-shift nanoemulsion: A potential nucleation agent for bubble-enhanced hifu tumor ablation, Ultrasound Med. Biol. 36 (11) (2010) 1856–1866. `doi:https://doi.org/10.1016/j.ultrasmedbio.2010.07.001`.

[11] M. Zhang, M. L. Fabiilli, K. J. Haworth, F. Padilla, S. D. Swanson, O. D. Kripfgans, P. L. Carson, J. B. Fowlkes, Acoustic droplet vaporization for enhancement of thermal ablation by high intensity focused ultrasound, Acad. Radiol. 18 (9) (2011) 1123–1132. `doi:https://doi.org/10.1016/j.acra.2011.04.012`.

[12] C. C. Chen, P. S. Sheeran, S.-Y. Wu, O. O. Olumolade, P. A. Dayton, E. E. Konofagou, Targeted drug delivery with focused ultrasound-induced blood-brain barrier opening using acoustically-activated nanodroplets, J. Control. Release 172 (3) (2013) 795–804. `doi:10.1016/j.jconrel.2013.09.025`.

[13] P. S. Sheeran, T. O. Matsunaga, P. A. Dayton, Phase change events of volatile liquid perfluorocarbon contrast agents produce unique acoustic signatures, Phys. Med. Biol. 59 (2) (2013) 379–401. `doi:10.1088/0031-9155/59/2/379`.

[14] N. Reznik, M. Seo, R. Williams, E. Bolewska-Pedyczak, M. Lee, N. Matsuura, J. Gariepy, F. S. Foster, P. N. Burns, Optical studies of vaporization and stability of fluorescently labelled perfluorocarbon droplets, Phys. Med. Biol. 57 (21) (2012) 7205–7217. `doi:10.1088/0031-9155/57/21/7205`.

[15] O. Shpak, L. Stricker, T. Kokhuis, Y. Luan, B. Fowlkes, M. Fabiilli, D. Lohse, N. de Jong, M. Versluis, Ultrafast dynamics of the acoustic vaporization of phase-change microdroplets, J. Acoust. Soc. Am. 133 (5) (2013) 3586–3586. `doi:10.1121/1.4806609`.

[16] R. Williams, C. Wright, E. Cherin, N. Reznik, M. Lee, I. Gorelikov, F. S. Foster, N. Matsuura, P. N. Burns, Characterization of submicron phase-change perfluorocarbon droplets for extravascular ultrasound imaging of cancer, Ultrasound Med. Biol. 39 (3) (2013) 475–489. `doi:10.1016/j.ultrasmedbio.2012.10.004`.

[17] O. Shpak, M. Verweij, H. J. Vos, N. de Jong, D. Lohse, M. Versluis, Acoustic droplet vaporization is initiated by superharmonic focusing, Proc. Nat. Acad. Sci. 111 (5) (2014) 1697–1702. `doi:10.1073/pnas.1312171111`.

[18] O. D. Kripfgans, J. B. Fowlkes, D. L. Miller, O. P. Eldevik, P. L. Carson, Acoustic droplet vaporization for therapeutic and diagnostic applications, Ultrasound Med. Biol. 26 (7) (2000) 1177–1189. `doi:10.1016/S0301-5629(00)00262-3`.

[19] T. Lacour, T. Valier-Brasier, F. Coulouvrat, Ultimate fate of a dynamical bubble/droplet system following acoustic vaporization, Phys. Fluids 32 (5) (2020) 051702. `doi:10.1063/5.0004375`.

[20] T. D. Martz, P. S. Sheeran, D. Bardin, A. P. Lee, P. A. Dayton, Precision manufacture of phase-change perfluorocarbon droplets using microfluidics, Ultrasound Med. Biol. 37 (11) (2011) 1952–1957. `doi:10.1016/j.ultrasmedbio.2011.08.012`.

[21] P. S. Sheeran, S. H. Luois, L. B. Mullin, T. O. Matsunaga, P. A. Dayton, Design of ultrasonically-activatable nanoparticles using low boiling point perfluorocarbons, Biomaterials 33 (11) (2012) 3262–3269. `doi:10.1016/j.biomaterials.2012.01.021`.

[22] C. Contino, M. Ollier, J. C. Maurizis, J. M. Lacombe, B. Pucci, Synthesis of cotelomers derived from tris(hydroxymethyl)acrylamidomethane (tham) bearing cytosine arabinoside moieties. preliminary investigation of their biological activity, Tetrahedron Lett. 37 (50) (1996) 9049–9052. `doi:https://doi.org/10.1016/S0040-4039(96)02122-3`.

[23] N. Bodin-Thomazo, F. Malloggi, P. Guenoun, Marker patterning: a spatially resolved method for tuning the wettability of pdms, RSC Adv. 7 (2017) 46514–46519. `doi:10.1039/C7RA05654K`.

[24] A. G. Mailer, P. S. Clegg, P. N. .Pusey, Particle sizing by dynamic light scattering: non-linear cumulant analysis, J. Phys. Condens. Matter 27 (14) (2015) 145102. `doi:10.1088/0953-8984/27/14/145102`.

[25] P. Morris, A. Hurrell, A. Shaw, E. Zhang, P. Beard, A fabry–pérot fiber-optic ultrasonic hydrophone for the simultaneous measurement of temperature and acoustic pressure, J. Acoust. Soc. Am. 125 (6) (2009) 3611–3622. `doi:10.1121/1.3117437`.

[26] C. K. Holland, R. E. Apfel, Thresholds for transient cavitation produced by pulsed ultrasound in a controlled nuclei environment, J. Acoust. Soc. Am. 88 (5) (1990) 2059–2069. `doi:10.1121/1.400102`.

[27] R. E. Apfel, Activatable infusable dispersions containing drops of a superheated liquid for methods of therapy and diagnosis (1997).
URL `https://www.surechembl.org/document/US-5840276-A`

[28] K. Johnston, C. Tapia-Siles, B. Gerold, M. Postema, S. Cochran, A. Cuschieri, P. Prentice, Periodic shock-emission from acoustically driven cavitation clouds: A source of the subharmonic signal, Ultrasonics 54 (8) (2014) 2151–2158. `doi:10.1016/j.ultras.2014.06.011`.

[29] T. G. Muir, E. L. Carstensen, Prediction of nonlinear acoustic effects at biomedical frequencies and intensities, Ultrasound Med. Biol. 6 (4) (1980) 345–357. `doi:10.1016/0301-5629(80)90004-6`.

[30] M. Aliabouzar, X. Lu, O. D. Kripfgans, J. B. Fowlkes, M. L. Fabiilli, Acoustic droplet vaporization in acoustically responsive scaffolds: Effects of frequency of excitation, volume fraction and threshold determination method, Ultrasound Med. Biol. 45 (12) (2019) 3246–3260. `doi:10.1016/j.ultrasmedbio.2019.08.018`.

[31] K. Radhakrishnan, K. B. Bader, K. J. Haworth, J. A. Kopechek, J. L. Raymond, S.-L. Huang, D. D. McPherson, C. K. Holland, Relationship between cavitation and loss of echogenicity from ultrasound contrast agents, Phys. Med. Biol. 58 (18) (2013) 6541–6563. `doi:10.1088/0031-9155/58/18/6541`.

[32] T. Giesecke, K. Hynynen, Ultrasound-mediated cavitation thresholds of liquid perfluorocarbon droplets in vitro, Ultrasound Med. Biol. 29 (9) (2003) 1359–1365. `doi:10.1016/S0301-5629(03)00980-3`.

[33] R. C. Tolman, The effect of droplet size on surface tension, J. Chem. Phys. 17 (3) (1949) 333–337. `doi:10.1063/1.1747247`.

[34] V. Holten, D. G. Labetski, M. E. H. van Dongen, Homogeneous nucleation of water between 200 and 240 k: New wave tube data and estimation of the tolman length, J. Chem. Phys. 123 (10) (2005) 104505. `doi:10.1063/1.2018638`.

[35] P. V. Yuldashev, M. M. Karzova, W. Kreider, P. B. Rosnitskiy, O. A. Sapozhnikov, V. A. Khokhlova, “hifu beam:” a simulator for predicting axially symmetric nonlinear acoustic fields generated by focused transducers in a layered medium, IEEE Trans. Ultrason. Ferroelectr. Freq. Control 68 (9) (2021) 2837–2852. `doi:10.1109/TUFFC.2021.3074611`.

[36] M. Blander, J. L. Katz, Bubble nucleation in liquids, AIChE J. 21 (5) (1975) 833–848. `doi:10.1002/aic.690210502`.

[37] M. Qian, J. Ma, The characteristics of heterogeneous nucleation on concave surfaces and implications for directed nucleation or surface activity by surface nanopatterning, J. Cryst. Growth 355 (1) (2012) 73–77. `doi:10.1016/j.jcrysgro.2012.06.031`.

[38] M. Qian, J. Ma, Heterogeneous nucleation on convex spherical substrate surfaces: A rigorous thermodynamic formulation of fletcher’s classical model and the new perspectives derived, J. Chem. Phys. 130 (21) (2009) 214709. `doi:10.1063/1.3146810`.

[39] E. Castillo, A. Hadi, N. Balakrishnan, J. Sarabia, Extreme Value and Related Models With Applications in Engineering and Science, Wiley, 2005.

[40] H. A. David, H. N. Nagaraja, Order Statistics, Wiley Series in Probability and Statistics, Wiley, 2004.
URL `https://books.google.fr/books?id=bdhzFXg6xFkC`

[41] P. Embrechts, C. Klüppelberg, T. Mikosch, Modelling Extremal Events for Insurance and Finance, Springer-Verlag, 1997. `doi:10.2143/AST.28.2.519071`.

[42] N. H. Fletcher, Size effect in heterogeneous nucleation, J. Chem. Phys. 29 (3) (1958) 572–576. `doi:10.1063/1.1744540`.

[43] S. Toschev, A. Milchev, S. Stoyanov, On some probabilistic aspects of the nucleation process, J. Cryst. Growth 13-14 (1972) 123–127, third International Conference on Crystal Growth. `doi:10.1016/0022-0248(72)90073-5`.

[44] V. Skripov, R. Kondor, D. Slutzkin, Metastable Liquids, A Hasted Press book, J. Wiley, 1974.
URL `https://books.google.fr/books?id=Sv6AAAAAIAAJ`

Supplemental Materials

Ultrasound Induced Vaporization of Perfluorohexane Droplets and Perfluorohexane/Water Droplets. Evidence of a heterogeneous nucleation

R. Ramesh, C. Thimonier, S. Desgranges, V. Faugeras, F. Coulouvrat, J. Laurent, G. Marrelec, C. Contino-Pépin, W. Urbach, C. Tribet, N. Taulier

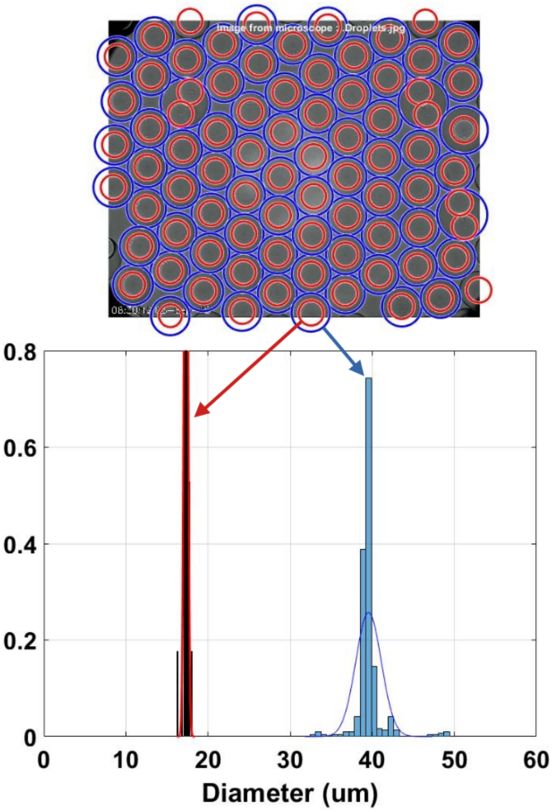

Figure S.1: Characterization of core shell droplets with the water volume fraction of $\varphi_w = 0.4$. The red circles delimit the water core and the blue circles the outer surface of the droplets. The measurements carried out on 75 droplets and fitted by a Gaussian distribution led to the following results: the external droplet radius $R = 20.3\,\mu\text{m}$ and the polydispersity, $\text{PDI} = (\sigma/\mu)^2 \approx 3 \times 10^{-3}$, where σ and μ are respectively the standard deviation and the mean value. The internal water radius $R_w = 9.1\,\mu\text{m}$ and $\text{PDI} \approx 6 \times 10^{-4}$.

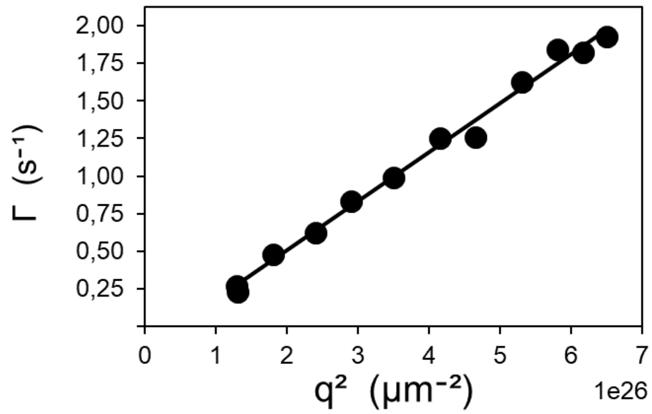

Figure S.2: The data represent Dynamic Light Scattering measurements performed on an emulsion prepared by high-pressure microfluidizer. The linear fit of Γ_θ versus q^2 leads to $R = 74.5 \pm 2\,\mathrm{nm}$ and to a polydispersity index PDI $= 0.12 \pm 0.06$, which indicates that the sample is monodisperse.

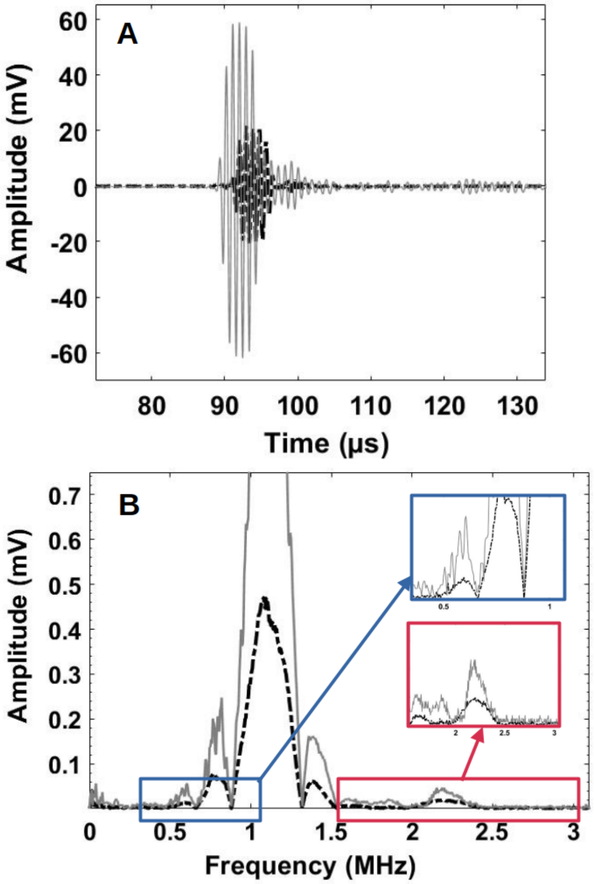

Figure S.3: In these experiments, plain PFH droplets of radius $R = 20\,\mu\text{m}$ were used in glycerol at 20°C with $P = 2\,\text{MPa}$ and $f_0 = 1.1\,\text{MHz}$. (A) Signals emitted by a sample, containing either glycerol (black) or PFH bubbles in glycerol (grey). (B) Fourier transforms of the mean values of 300 signals represented in (A). Insets: magnifications of the signals in the vicinity of 0.55 and 2.2 MHz, respectively.

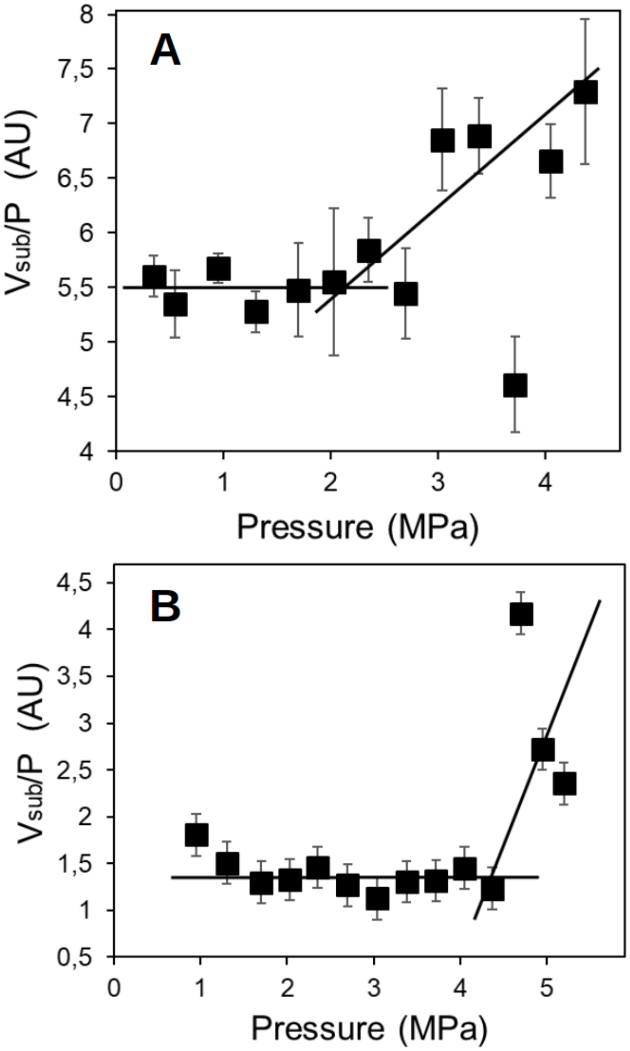

Figure S.4: Normalized subharmonic component peak amplitude of the scattered response of a suspension of PFH droplets ($R = 20\,\mu\text{m}$, $\varphi_d = 5 \times 10^{-4}$) in glycerol (figure A) and of a glycerol solution devoid of droplets (figure B) as a function of applied acoustic pressure P.The two lines intersect give $P = 2.1 \pm 0.3\,\text{MPa}$ for the figure A and $4.5 \pm 0.3\,\text{MPa}$ for the figure B. Consequently, the vaporization of PFH droplets appears before glycerol cavitation when pressure increases.

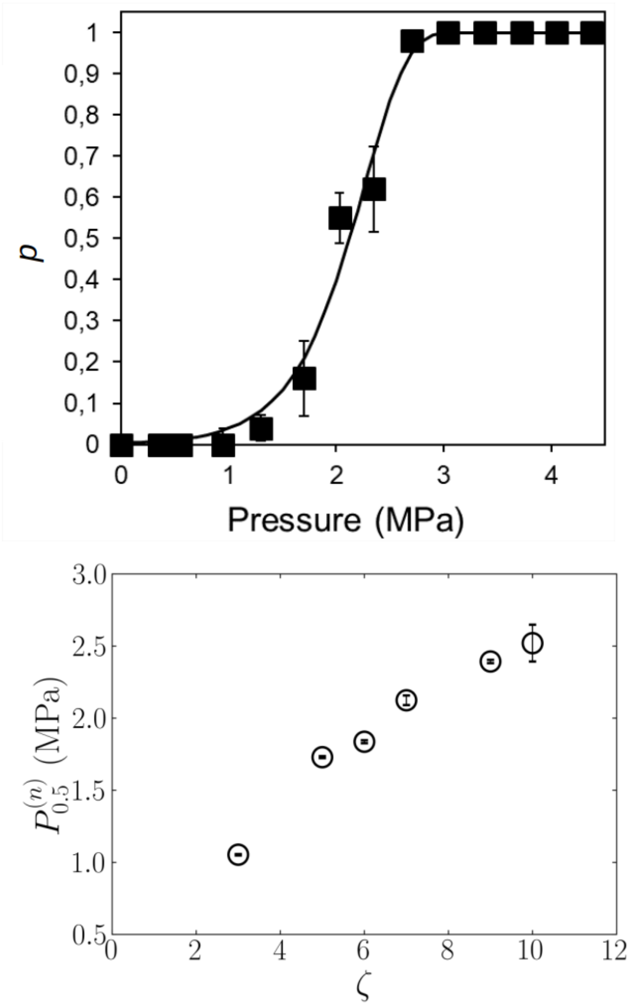

Figure S.5: For both figures we used a solution of plain PFH droplets having a radius of $R = 20\,\mu\text{m}$, at a droplet volume fraction of $\varphi_d = 5 \times 10^{-4}$. The top figure represents the probability p to measure an ADV event as a function of the applied acoustic pressure P. From this figure we derived that $P = 2.12 \pm 0.03\,\text{MPa}$ at $p = 1/2$, the solid line being a fit to Eq. 3 with $\zeta = 7$. The bottom figure shows how the derived value of $P_{0.5}^{(n)}$, the acoustic pressure when to probability of an ADV event is $p = 1/2$, behaves when varying the number of standard deviations ζ. In all these figures, each point represents the average of 3 measurements.

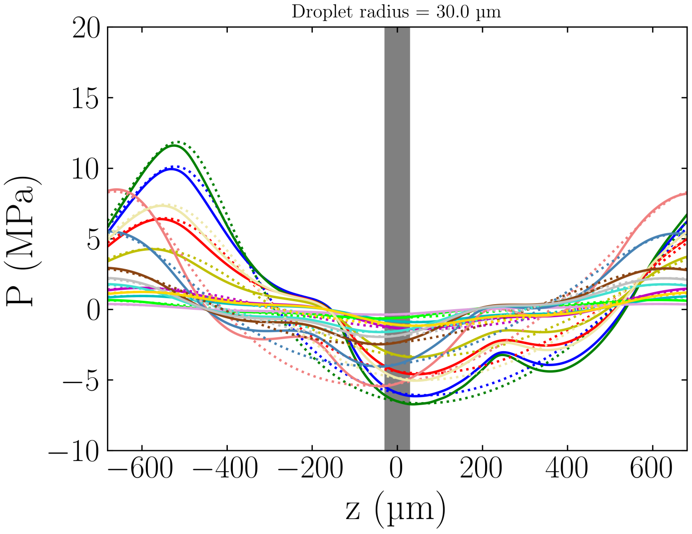

Figure S.6: Variation of the pressure wave in the presence of a droplet (solid lines) and in the absence of a droplet (dotted lines) along the z axis (i.e. $\theta = 0$ or π, and $0 < r < R$). The different color lines correspond to various intensities given to the transducer in the HIFU-beam simulator script. The grey band indicates the radius of the droplet, that is 30 µm in this figure. The calculation was performed for z spanning over the acoustic wavelength (i.e. c/f). The lines are snapshots of the wave where t varies over a wave period $T = 1/f$ and for which the pressure inside the droplet is the minimal.

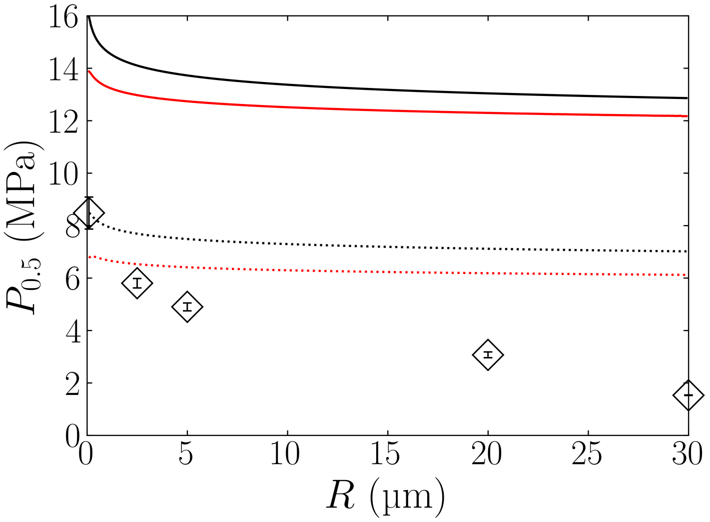

Figure S.7: The points ($\Diamond$) are the experimentally derived values of $P_{0.5}^{(1)}$, as given in Fig. 5. The black lines are the prediction of the change in $P_{0.5}^{(1)}$ calculated from homogeneous nucleation as given by Eq. 18 when using $\gamma_{gl}(\infty) = 12\,\mathrm{mN/m}$ as experimentally measured (black solid line) or $8\,\mathrm{mN/m}$ (black dotted line). The red lines are the prediction calculated from heterogeneous nucleation as given by Eq. 23 when using the experimental interface tension given in Table 1 (red solid line) or when taking $\gamma_{gl}(\infty) = 8\,\mathrm{mN/m}$ (red dotted line).

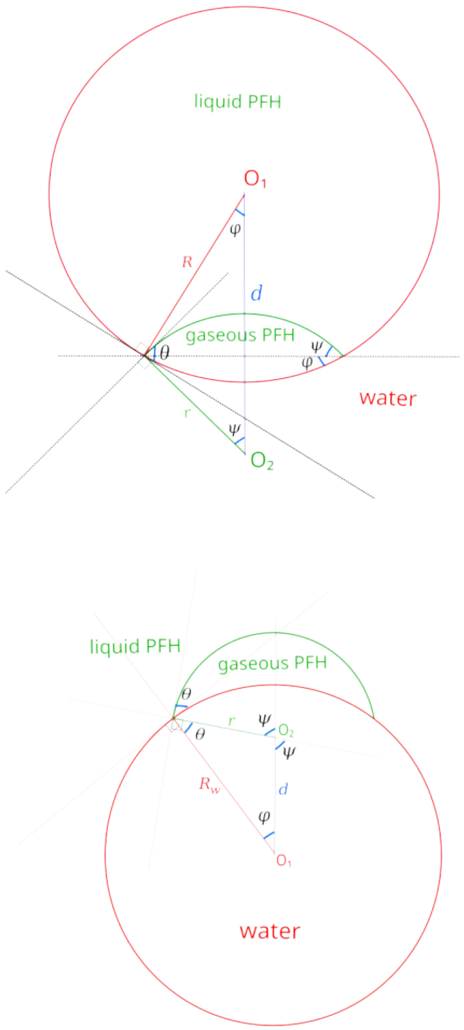

Figure S.8: Schemes of the heterogeneous nucleation occurring on either concave (top) or convex (bottom) rigid surfaces.

3.2 Ultrasound-triggered delivery from versatile emulsion droplets systems at pressures below Acoustic Droplet Vaporization (ADV) threshold

Following the determination of the ADV threshold for our droplet systems in the previous chapter, we then studied the parameters necessary to deliver the hydrophilic or hydrophobic content from the core of emulsion droplets. We studied PFH droplets and ATBC (non-vaporizable) droplets, to compare the release. We investigated the mechanism of delivery of hydrophilic fluorescein sodium from the following types of water-core droplets:

- multiple water droplets in perfluorohexane, in water,
- multiple water droplets in tributyl o-acetylcitrate, in water,
- a single water droplet in perfluorocarbon, in water.

We also studied the release of hydrophobic Nile red from single emulsion droplets made with tributyl-o-acetyl citrate. These droplets were made in microfluidic systems, using flow-focusing junctions. The effect of the radius of the droplets on the percentage of release was studied by using radii of 20 μm and 30 μm. The effect of the duty cycle was studied by varying the ultrasonic pulse length: 5 or 50 sinusoidal periods were used, at a PRF of 11 kHz, resulting in duty cycles of 5% or 50% respectively. The release started at a peak negative pressure between 0.2 MPa and 0.5 MPa for all droplets, regardless of the diameter and the oil composition. These low pressures are clinically relevant, but more importantly, they are below the ADV threshold. In all cases, delivery started without the vaporization of the PFC or cavitation. The percentages of release from multi-core PFH droplets, multi-core ATBC droplets, and plain ATBC droplets, align on a universal curve, indicating the same diffusion mechanism of release. In the case of single-core droplets, we observe a different mechanism of release, for which the inner water droplet is partially pushed out of the PFH shell with the acoustic wave. This conformation can result either in the inner droplet going back into the core of the PFH phase or can be pushed out completely and release its content in the bulk.

Overall, this article demonstrates the possibility to use versatile emulsion systems for the controlled delivery of hydrophilic and hydrophobic payload, without vaporization or cavitation, therefore without risking degradation of the content, or of the surrounding tissue in biomedical applications.

Ultrasound-triggered delivery from versatile emulsion droplets systems at pressures below Acoustic Droplet Vaporization (ADV) threshold

C. Thimonier[a,b,c], F.Pincet[b], M.Martin[a,b], S.Desgranges[d], J. Laurent[e], C. Contino-Pépin[d], W. Urbach[a,b], C. Tribet[c], N. Taulier[a]

[a]*Sorbonne Université, CNRS, INSERM, Laboratoire d'Imagerie Biomédicale, LIB, F-75006 Paris, France*
[b]*Laboratoire de Physique de l'École Normale Supérieure, ENS, Université PSL, CNRS, Sorbonne Université, Université Paris Cité, F-75005 Paris, France.*
[c]*Laboratoire de Chimie de l'École Normale Supérieure, ENS, Université PSL, CNRS, Sorbonne Université, Université Paris Cité, F-75005 Paris, France*
[d]*Avignon Université, Équipe Systèmes Amphiphiles bioactifs et Formulations Eco-compatibles, UPRI, 84000 Avignon, France*
[e]*PMMH ESPCI Université PSL, CNRS, Sorbonne Université, Université de Paris 75005 Paris France*

Abstract

In targeted therapy, vehicles deliver active ingredients to the area of interest. Ultrasound waves are used as an external stimulus to induce the release of the drugs enclosed [1, 2, 3]. Perfluorocarbon (PFC) oil droplets are carriers of choice because they are stable and biocompatible. The release of a drug carried by such systems is usually caused by the vaporization of the droplets induced by the ultrasound signal [3, 4, 5]. Here we present the release of hydrophilic and hydrophobic dye from three families of biocompatible droplets dispersed in saline solution. All droplets were made in microfluidic devices which ensures their monodispersity. The first type consists of micrometer droplets of oil (PFC or tributyl-o-acetyl citrate, ATBC) containing many nanometric droplets of water and a hydrophilic fluorescent dye. The second type are PFC droplets containing only a single micrometric droplet of water and a fluorescent dye. The third type consists of droplets of ATBC containing a hydrophobic dye. In all cases, the release of the sequestered molecules is induced by an ultrasonic wave, at a frequency of 1.1 MHz, and at pressures clearly lower than those which cause the acoustic droplet vaporization. Increasing the incident energy on the droplets increases the maximum achievable release, but does not affect the pressure at which the release begins. The release of markers from all droplets follow a diffusion model, from the droplet to the surrounding environment provided an energy barrier is overcome. Ultrasound causes the decrease of the energy barrier necessary for the markers to diffuse.

Keywords: Perfluorohexane, Acoustic delivery, Droplets, Double emulsions

---

1. Introduction

Targeted drug delivery has been studied as a solution to increase the efficacy of treatment while decreasing toxicity and side effects [6, 7, 8, 9]. It consists in encapsulating an active in an object (capsule, shell etc) and delivering it in a controlled way at the target site [10, 11]. The drug is protected from multiple physiological barriers which degrade it (such as stomach acidity) and a higher percentage reaches the target. At the site of interest, the particles can then accumulate passively (Enhanced Permeability and Retention effect [12, 13]) or actively [14]. When the particles reach the target site, they can be destabilized through an external stimulus to deliver their content abruptly [15] or to induce a diffusion of the drug from the particle to the surrounding environment [16]. Liposomes have been widely studied to serve such a function, and few have been commercialized (e.g. Doxil, Onivyde) [17]. A main disadvantage of liposomes is that they are leaky before reaching the target location[18]. Other encapsulation methods include polymeric nanoparticles, which are difficult to produce in high-throughput [19] or micelles which can only contains lipophilic drugs[20]. Another encapsulation method consists in using emulsions of perfluorocarbon (PFC) oils [5, 21, 22]. PFC's are biocompatible, immiscible with water or organic oils, and have the particular ability to undergo a phase change when stimulated with ultrasound [23]. Indeed, when treated with an acoustic pressure above a threshold, liquid PFC droplets become gaseous bubbles [24, 25, 26]. This process is called Acoustic Droplet Vaporization (ADV). Since PFC oils are hydrophobic and lipophobic they can act as a shell surrounding a water or oil core in which a drug can be solubilized. The phase change resulting from ADV is thought to be the mechanism responsible for the ultrasound-triggered delivery of actives from PFC emulsions [27, 28, 3]. The mechanism of delivery through acoustic stimulus is not well understood. However, it has recently been shown that ultrasound can be used to trigger a diffusion mechanism, without vaporization or thermal effects, when using non-perfluorocarbonated oils that do not have the ability to vaporize [16]. Here, we demonstrate that perfluoro-

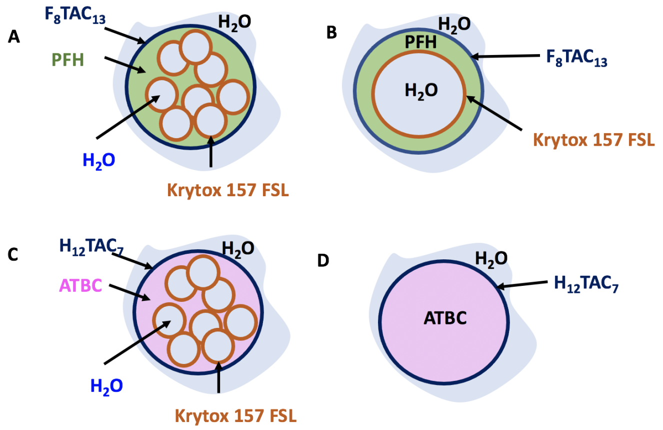

Figure 1 – Scheme of all droplet types used. A: Multi-core PFH double emulsions. B: Single-core PFH double emulsions. C: Multi-core ATBC emulsions. D: Plain ATBC emulsions. Droplets A-C are used to carry a hydrophilic cargo, droplet D is used to carry a hydrophobic cargo.

hexane (PFH) emulsions can release their content without ADV, at high acoustic frequency. The release pattern is compared to droplets made with tributyl-o-acetyl citrate (ATBC), a biocompatible oil that does not undergo ADV at the pressures used. We study the release of sodium fluorescein, a hydrophilic fluorescent probe, from three types of water core double emulsion droplets (fig.1):

- multiple water nanodroplets, in PFH, in water, referred to as multi-core PFH droplets,
- a single water microdroplet in PFH in water, referred to as single-core PFH droplets,
- and multiple water nanodroplets, in ATBC, in water, referred to as multi-core ATBC droplets.

We also study the release of Nile red, a hydrophobic fluorescent probe, from single emulsions of ATBC in water, referred to as plain ATBC droplets. Three different surfactants are used to stabilize the different interfaces. F_8TAC_{13}, which is a biocompatible fluorinated surfactant, stabilizes the PFH/external water interfaces in PFH based droplets (fig. 1). Commercial Krytox 157 FSL (for which the biocompatibility is still under investigation) is used to stabilize the internal Water core/PFH interfaces and the Water core/ATBC interface of multi-core ATBC droplets. $H_{12}TAC_7$, which is a biocompatible non-fluorinated surfactant, is used to stabilize the external ATBC/external water interfaces of ATBC droplets. An acoustic signal at a frequency of 1.1 MHz over an insonation time of approximately 2 minutes triggers the release of dyes without ADV, regardless of the type of oil (PFH or ATBC) used. The pressures used to trigger the release from all droplets are between 0.2 and 0.5 MPa, which are significantly lower than the ADV thresholds of the PFH droplets (1.8 MPa for multi-core PFH droplets and 2.2 MPa for single-core PFH droplets. Increasing the acoustic energy increases the maximum release achievable, but does not affect the pressure at which the release starts. The droplets all undergo the same release mechanism, which is a diffusion. We suggest that the release mechanism for single-core PFH droplets could also consist in the internal water droplet being pushed out of the PFH shell, and being destabilized in the surrounding water bulk due to a change in interfacial tension. Overall, we demonstrate the ability to release the hydrophilic and hydrophobic content of both PFC-based and non-PFC based systems without vaporization at low, clinically relevant pressures over short insonation times.

2. Materials and Methods

2.1. Materials

Unless otherwise stated, all chemicals were filtered with 0.2 µm pore size Acrodisc Syringe Filters (from Pall, France) and used without further purification. All aqueous solutions were made using Milli-Q IQ 7000 Type-1 water Purification System. PDMS Sylgard 184 was purchased from Neyco (France). Photoresist SU8 was purchased from Chimie Tech Services (France). Silicon wafers were obtained from BT Electronics (France). The MFCS–EZ, pressure controllers used to inject the fluids into the microfluidic chips and the flow units (sizes S and M) used to measure the flow rates were purchased from Fluigent (Le Kremin-Bicêtre, France). The 0.35 mm diameter biopsy puncher was bought from World Precision Instruments (UK), while the plasma cleaner was purchased from Harrick Scientific (NY, United States). Perfluorohexane and the fluorinated surfactant, Krytox FSL 157, were purchased respectively from ABCR GmbH (Germany) and Costenoble (Germany). The surfactants F_8TAC_{13} and $H_{12}TAC_7$ are homemade (details in Sections 3.2. and 3.3.) Nile red was purchased from Merck (France) and sodium fluorescein was obtained from VWR (France). Tributyl O-acetylcitrate, methanol and NaCl were obtained from Sigma Aldrich (France).

2.2. Synthesis of F_8TAC_{13} and $H_{12}TAC_7$ surfactants

F-TAC and H-TAC surfactants are amphiphilic molecules composed of two structural units (fig.2). One of the units is a water-soluble oligomer of Tris(hydroxymethyl) aminomethane (Tris) acrylamide units, which constitutes the polar head of the surfactant. Depending on the conditions carried out for their synthesis, it is possible to tune the average number of Tris-acrylamide units.

The second unit is a fluorinated tail (in the case of F-TAC) or hydrocarbonated tail (in the case of H-TAC) that acts as a fluorophilic or hydrophobic anchorage ensuring the stabilization of the PFC or ATBC droplet. The F-TAC used in the current study is made of a perfluoro-octyl tail endowed with thirteen Tris-acrylamide units (F_8TAC_{13}) (fig.3). The H-TAC used is made of a dodecane tail endowed with seven Tris-acrylamide units.

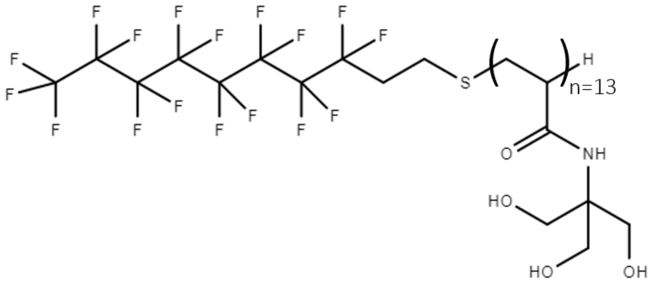

Figure 2 – Chemical structure of F_8TAC_{13} surfactant.

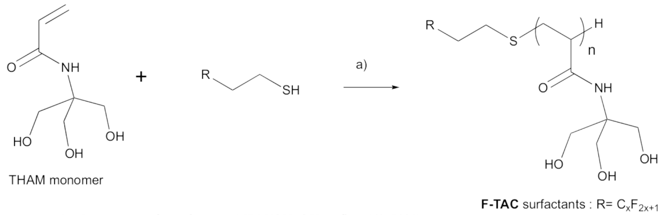

(a) *Reagents and conditions:* AIBN/CH_3OH, reflux (62-73%).

Figure 3 – Scheme of the synthesis of F-TAC (R = C8F17-, n = 13) or H-TAC (R = C12H25-, n = 7)

2.3. *Microfluidic devices for droplet production*

The droplets were generated in microfluidic devices using flow-focusing geometries (fig.4). We manufactured two types of chips. The first one, suitable for the production of plain ATBC single emulsions and multi-core double emulsion droplets (fig. 4A and B), uses a single flow-focusing junction. All channels are 20 µm deep, 100 µm wide, and the nozzle size is 20 µm.

The second type of chip was used for the production of single-core PFH droplets and is made of two flow-focusing junctions in series inside one chip, as shown in fig.4C. All channels are 50 µm deep and 100 µm wide, the nozzle sizes are 35 µm (first nozzle between sections 1-2-3 on fig.4C) and 70 µm (second nozzle between sections 3-4-5 on fig.4C). Both chips were first designed on AutoCAD. They were printed on a wafer using a two-photon polymerization printer, a Nanoscribe GT Photonic Professional device, with a negative-tone photoresist IP-S (Nanoscribe GmbH, Germany) and 25x objective, directly on silicon substrates after nitrogen plasma cleaning. To reduce printing time, a shell writing strategy was applied. It consists in fabricating a dense shell delimiting the structure, the inner part being only partly polymerized in the form of a scaffold. After developing in propylene glycol methyl ether acetate (PGMEA) for 30 min and isopropanol (5min), a batch polymerization is performed with UV-exposure. The microfluidic chips were made using polydimethylsiloxane (PDMS) and its curing agent at a ratio of 10:1 poured onto the wafer which served as a mold for the circuit. It was degassed in a vacuum then baked at 70°C for 2h. The

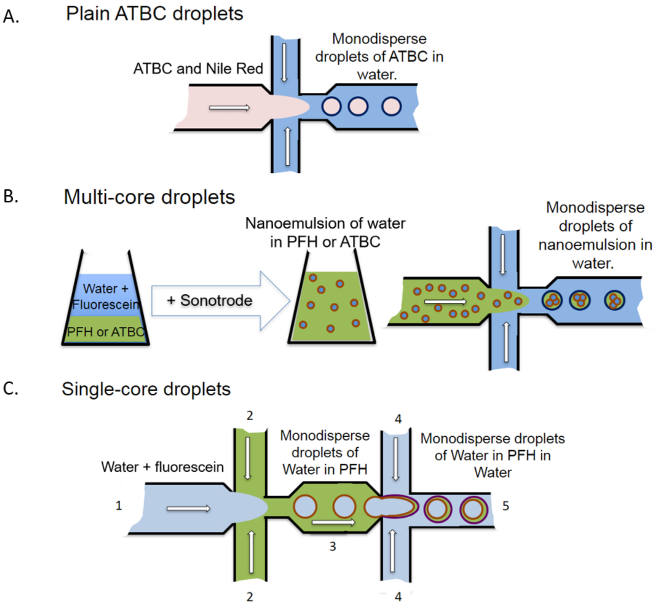

Figure 4 – A: Schematic representation of the flow-focusing junction used to produce plain ATBC single emulsion droplets. The ATBC dispersed (pink) phase arrives at the level of the nozzle and is pinched by the continuous phase to produce monodisperse droplets. The nozzle width is 40 µm. All channels are 20 µm deep and 100 µm wide. B: Schematic representation of the production steps of multi-core (PFH or ATBC) double emulsions. The core aqueous phase and the oil phase are sonicated to produce the primary nanoemulsion. C: Schematic representation of two-nozzle device made of two flow-focusing junctions (1-2-3 & 3-4-5) used to produce the single-core double emulsion. The channel between the two junctions (channel 3) is hydrophobic. The flow rates were adjusted to encapsulate exactly one water droplet in each double emulsion (Table.S.2 in Supplementary Information). All channels are 50 µm deep and 100 µm wide. The first nozzle (at junction 1-2-3) is 35 µm and the second one (at junction 3-4-5) is 70 µm.

inlets and outlets were punched with a 0.35 mm diameter biopsy puncher. The chips were cleaned with isopropanol and dried with nitrogen gas.

2.4. Surface treatment

2.4.1. Multi-core and plain droplets

The single flow-focusing chip used for single emulsions and multi-core droplets underwent a hydrophilic surface treatment. The circuit side of the chip and a microscope glass slide were both activated in an air plasma (18 W for 1 min). They were then put in contact to bond, and placed in the oven at 70°C for 30 min to strengthen the bonding. The bonded chip was cooled to room temperature and activated again in an air plasma for 1 min. Water was inserted inside the chip with Fluigent pressure controllers to make the circuit walls hydrophilic.

2.4.2. Single-core droplets

The double flow-focusing chip used to make single-core double emulsions was selectively treated. The section shown in green on fig.4C was kept hydrophobic as the PFH was the phase in contact with the channel walls in this region. To avoid the destabilization of the first emulsion it is therefore necessary to keep this area hydrophobic. The rest of the chip (in blue) was treated hydrophilic, because this is where water is in contact with the channel walls (1, 4, 5 on fig.4C). A flat PDMS layer was used as a substrate for the chip instead of a glass slide. Following the procedure developped by Bodin-Thomazo et al (2017) [29], the hydrophobic region was selectively patterned using a black permanent marker (Stabilo Superfine), to prevent its activation during the subsequent plasma treatment. A mirror line of this marker patterning was drawn on the PDMS layer substrate. The chip and the substrate were put in an air plasma (18 W for 1 min), after which they were aligned to fit the marker pattern. 2 minutes after the bonding of the chip, methanol was passed through using the pressure controllers at 20 mbar for 2 minutes to remove the marker. Water was subsequently passed through for 30 minutes.

2.5. Production of multi-core double emulsion droplets

The multi-core double emulsions consists of three phases (fig.1, top left and bottom left):

- The dispersed phase is made of water with 0.9%wt NaCl and 1%wt sodium fluorescein.
- The intermediate phase is made of PFH or ATBC and 5%wt of Krytox 157 FSL.
- The continuous phase is made of water and 0.1%wt of F_8TAC_{13} (when PFH is used in the intermediate phase) or $H_{12}TAC_7$ (when ATBC is used in the intermediate phase).

First, a primary nanoemulsion of normal saline (0.9%wt NaCl in water) and fluorescein, in oil was produced by sonicating 400µL of dispersed phase and 600 µL of intermediate phase (Branson Ultrasonics Sonifier horn at a frequency of 20 kHz, 30% of maximum amplitude for a pulse of 5 cycles). During sonication, the 1.8mL vial containing the fluids was immersed in an ice water bath to avoid thermal effects. A nanoemulsion made of normal saline and fluorescein surrounded by Krytox and dispersed in the oil was thus produced. In the next step the multi-core droplets were generated in the flow-focusing chip shown in fig.4B, with the primary nanoemulsion as the dispersed phase. The resulting multi-core droplets therefore consist of multiple aqueous nanodroplets inside a larger oil droplet, surrounded by water. The pressures and flow rates used to produce these emulsions are shown in Table S.1 in Supplementary Information.

2.5.1. Production of water single-core PFH droplets

Single-core double emulsion droplets consist of three phases:

- The dispersed phase is made of water with 0.9%wt NaCl and 1%wt sodium fluorescein.
- The intermediate phase is made of PFH and 5%wt of Krytox 157 FSL.
- The continuous phase is made of water and 0.1%wt of F_8TAC_{13}.

They were produced using the double flow-focusing junction device shown in fig.4C, where section 1 represents the channel where the dispersed phase enters; section 2 represents the channel where the intermediate phase enters; section 3 represents the channel in which the first emulsion of water in PFH is formed; section 4 represents the channel where the continuous phase enters; and section 5 represents the channel where the double emulsion of a single water droplet in PFH in water is formed. After the surface treatment, the different fluid phases were injected into the chip by applying a pressure of 20 mbar to the headspace of their respective inlets using the pressure controllers. The flow rates were adjusted to encapsulate exactly one water droplet in each double emulsion (shown in Table S.2 in Supplementary Information).

2.5.2. Production of plain tributyl o-acetylcitrate droplets

Plain ATBC single emulsions were made using a dispersed phase of ATBC and 0.025% weight Nile red. The continuous phase was made of water and 0.1%wt $H_{12}TAC_7$. The droplets were made using the same chip geometry as the multi-core double emulsion droplets (fig.4A), where the dispersed phase was pinched by the continuous phase at the nozzle to produce droplets. The pressures and flow rates used are shown in Table.S.1 in Supplementary Information.

2.5.3. Characterization of droplets

The size and polydispersity of the droplets were determined from a series of images taken with an ultra-fast camera (Model SC1, Edgertronic, USA) during their production. The collected recordings were analyzed with an in-house MATLAB program. The code uses a Circular Hough Transform (CHT) based algorithm for locating the droplets and then estimating their diameter along with the polydispersity index (PDI). Fig.S.1 presents an example of the MATLAB characterization of the produced single-core droplets. The aqueous volume fraction in the single-core double emulsion droplets is calculated by monitoring two parameters: the number of droplets generated per second, which can be captured via the high-speed camera, and the flow rate of each phase recorded from the flow unit of the pressure controller. The volume fraction is then predicted using an in-house MATLAB code.

The size and the polydispersity of nanosize droplets in the multi-core droplets were determined by dynamic light scattering using an ALV/CGS-3 platform based goniometer system (from ALV GmbH). The measurements were performed on emulsions diluted 1000 times, at room temperature, and scattering angles, θ, ranging from 60° to 130°, with a step of 10°. At each angle θ, the device provided the decay rate $\Gamma_\theta = q^2(k_B T/6\pi\eta R)$; where k_B is the Boltzmann constant, T is the temperature in K, η is the viscosity of the solvent, and $q(\theta) = 4\pi n sin(\theta/2)/\lambda$ is the magnitude of the scattering vector. The refractive index of the solvent is n = 1.33 and $\lambda = 633$ nm is the laser wavelength. A fit of the curve by the cumulant method thus made it possible to determine the hydrodynamic droplet mean radius R along with the polydispersity index (PDI) [30].

2.6. Interfacial tension

Three interfacial tensions between the aqueous and PFH phase were measured with an error of 2 mN/m using a Tracker tensiometer (Teclis, France) at 20 ℃. The tensiometer analyzes the shape of a pendant or rising drop in bulk, using the Young–Laplace equation to derive the interfacial tension. In the case where the measurement was taken between PFH and water with F_8TAC_{13}, or when it was taken between water and PFH with 5% Krytox, the pendant drop method was used [31]. The water drop volume was kept constant at 2 mm^3. We waited until the interfacial tension reached an equilibrium value to extract the interfacial tension value. In the case where the measurement was taken between PFH with 5% Krytox, and water with F_8TAC_{13}, another method was used. The bulk was PFH and 5% Krytox on the bottom, and water with F_8TAC at the top (because PFC is more dense than water the interface between the two was stable). A rising water droplet was formed with a curved 0.6 mm diameter needle on a Hamilton 700 series syringe, in the PFH and Krytox phase, therefore covered in Krytox, and creamed to the interface, where it went halfway into the water with F_8TAC_{13} phase. The droplet remained stable at the interface (fig. S.3 in SI Section 6.6) for a few minutes before collapsing. The interfacial tension at top interface of the droplet, which mimics the inner droplet of a single-core double emulsion droplet in dewetting conformation, was measured. As a control test, we measured the interfacial tension of a sessile air bubble in water: a value of 72 mN/m was measured.

2.7. Determination of ADV threshold

To determine the ADV threshold (P_{ADV}) of PFH droplets, we used the intersect method described by Aliabouzar et al, Osborn et al, and Fabiilli et al [5, 32, 33]. To summarize, the Fast Fourrier Transform of the acoustic signal was analyzed and the magnitude of the subharmonic peak at 0.5 MHz, which is indicative of ADV, was normalized by the pressure. This value was plotted against the acoustic pressure (fig.S.2, top graph). P_{ADV} was determined as the pressure at which the normalized magnitude starts to increase (2.1 MPa). As an alternative method, the probability of ADV occurring for each pressure was determined. Every time a subharmonic peak at 0.5 MHz was observed, it was counted as one event. The number of events out of 100 pulses (fig.S.2, bottom graph) was counted to obtain a probability. We found that the pressure value at which the probability, p, is $\frac{1}{2}$, matched the P_{ADV} value obtained with the intersect method. This probability method was then used to determine the P_{ADV} of multi-core PFH droplets and single-core PFH droplets, as it is more precise and can be fitted with a probabilistic model.

2.8. Delivery of fluorescent probe from droplets

2.8.1. Experimental set-up

[p]

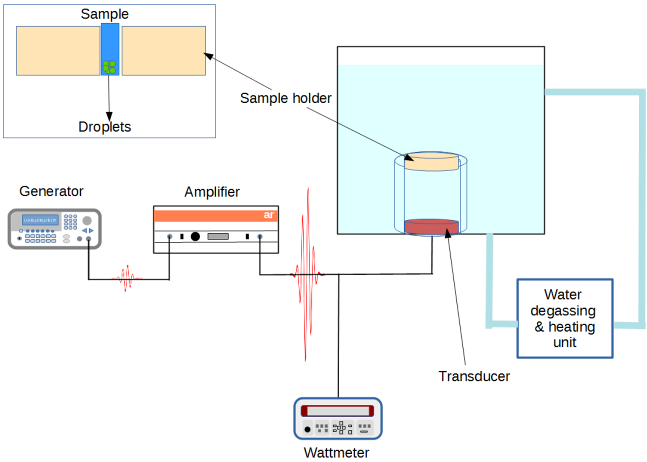

Figure 5 – Diagram of the experimental setup. The 1.1 MHz signal, delivered by the generator, is amplified and sent to the transducer. The resulting ultrasonic wave is focused on the bottom of the sample located in the center of the sample holder. The focal zone is an ellipsoid with volume 9 mm^3.

2.8.2. Preparation of the sample

To remove free fluorescent probe from the sample, the droplet solution was pipetted into tubes with membrane size 100 kDa MWCO (Pierce^{TM} Concentrator, PES, 0.5 mL, Thermo Scientific, UK) to perform filtration. The sample was centrifuged, at 12 000 g for 40 min and 4°C. The filtered solution was removed and replaced with new bulk solution. This filtration through centrifugation step was repeated 5 times to achieve complete removal (until the filtered solution no longer contained fluorescent probe detectable with the spectrofluorometer). For fluorescein release experiments, the sample was then prepared in 2 mL tubes (MC 200, Fisherbrand) containing 1 mL of normal saline (9 g NaCl/L of water) and 5 µL of droplet solution, taken from the bottom of the droplet sample tube where the droplets sedimented. For Nile red release experiments, the sample contained 1.5 µL of droplet solution, 200 µL of normal saline and 100 µL of ATBC. Since ATBC is less dense than water, it formed a layer above the water. Nile red from the droplets being hydrophobic, was released in the water but traveled to the oil layer.

2.8.3. Acoustic treatment of sample

The signal consisted of sine-wave bursts at fundamental frequency 1.1 MHz. We used duty cycles of 5% and 50% (meaning that the sample is insonified respectively 5% and 50% of the total time), and a pulse repetition frequency of 11 kHz. We used peak negative acoustic pressures varying from 0.2 MPa to 2.3 MPa. The total experiment time was 7 minutes, but the actual insonation time was either 0.35 or 3.5 minutes, and the temperature difference did not exceed 1.5°C. For every acoustically treated sample, 1 mL of normal saline was pipetted into the 2 mL centrifuge tube, the droplets were added and the sample tube was placed on the ultrasound set up for insonation. Two control samples were used at the beginning of each set of experiments. One control sample was used as a 100% release reference. The same volume of droplets solution was destabilized in 200µL of methanol then 800 µL of normal saline was added. The second control was a sample of 1 mL of normal saline and the same volume of droplet solution as for the other samples. The passive release was assessed over 7 minutes, with no acoustic treatment.

2.8.4. Detection of fluorescence to determine release percentage

The release was determined from the intensity of fluorescence of the probe detected in the supernatant of the sample. For experiments with fluorescein, 850 µL of supernatant was pipetted into a 1 mm thick optical path spectroscopy cuvette (Hellma). The cuvette was placed in a spectrofluorometer (Jasco Spectrofluorometer FP-8300, Germany). The fluorescence was analyzed with an excitation wavelength of 470 nm and emission at 513 nm. To detect Nile red, 70 µL of the top ATBC layer in the sample was taken and pipetted into a 100 µL, 1 mm thick optical path spectroscopy cuvette (Hellma). The excitation wavelength was 530 nm and the emission wavelength was 568 nm. The concentration released was obtained from standard curves for each fluorescent probe. The concentration release was compared to the initial concentration in the droplets to obtain a percentage.

2.8.5. Analysis of release data

For each sample, the pressure at which the experiment was performed was converted into an acoustic energy value. The acoustic energy at each pressure for each number of cycles was calculated as

$$E = \frac{n < P^2 >}{\rho_o c} \tag{1}$$

where $< P >$ is the average pressure integrated over one period, n is the number of cycles in one pulse, ρ_o is the density of water and c is the speed of sound in water. The percentage of release was normalized by R^3, where R is the radius of the droplet, and by the number of droplets in the focal zone, n_f (calculation shown in SI Section 18) The equation used to fit the data is

$$f = \beta(1 - e^{-\alpha E}) \tag{2}$$

where $f = \frac{C_B}{C_0 R^3 n_f}$. C_B is the concentration of probe molecules in the bulk, C_0 is the initial concentration in the droplets, R is the radius of the external droplet, n_f is the mean number of droplets in the focal zone, $\beta = \frac{\frac{4}{3}\pi}{V_B}$ is the coefficient of the fit, α is a constant, and E is the acoustic energy. The coefficient of the fit, β is 6.25×10^{-7} µm^{-3}. Details are given in Supplementary Information Section 6.3 about the calculation of the equation of the fit.

3. Results

3.1. ADV of multi-core and single-core PFH double emulsions

The P$_{ADV}$ of the multi-core and single-core double emulsion PFH droplets are respectively 2.2 MPa and 1.8 MPa (fig.6).

3.2. More efficient release from larger droplets

The pressures at which release starts for both types of PFH droplets are below their respective P$_{ADV}$ (Table. 1). The percentage of release from 30 µm droplets is higher than from 20µm droplets at all pressures. The pressures at which ATBC based droplets start to release their content and the maximum percentage of release are comparable to the ones for PFH based droplets of equal radius. Incorporating a hydrophilic dispersed phase in the core does does not have an effect on the pressure at which release start and reduces the maximum release percentage by 8%. Overall, 30 µm droplets release a higher percentage of their content than 20µm droplets at all pressures and for

	MC PFH					SC PFH				MC ATBC		Plain ATBC			
R (µm)	20			30		20		30		20		20		30	
Nb. cycles	5	20	50	5	50	5	50	5	50	5	50	5	50	5	50
P_{start} (MPa)	0.5	0.2	0.2	0.2	0.2	0.5	0.2	0.2	0.2	0.5	0.5	0.8	0.2	0.5	0.2
E (kW/cm^2)	0.04	0.03	0.07	0.01	0.07	0.01	0.07	0.04	0.42	0.11	0.07	0.04	0.07	0.04	0.07
Start %	2	2	4	2	4	11	18	16	6	6	18	5	2	6	2
Max. %	23	50	53	80	88	63	87	91	87	12	52	27	60	29	85

Table 1 – Table showing the pressures at which release starts (P_{start}), the number of cycles in the pulse of the pulse (Nb.cycles), the percentage of release achieved at the start pressure (start %), the corresponding energy calculated with eq. 1 (E), and the maximum release (max %) achieved for each radius (R) of multi-core PFH (MC PFH) for which $P_{ADV} = 2.2$ MPa, single-core PFH (SC PFH) for which $P_{ADV} = 1.8$ MPa, multi-core ATBC (MC ATBC) and plain ATBC droplets. The error of pressure measurement is 20% (which corresponds to the error of the hydrophone measurement). The error observed on percentage of release is 15%.

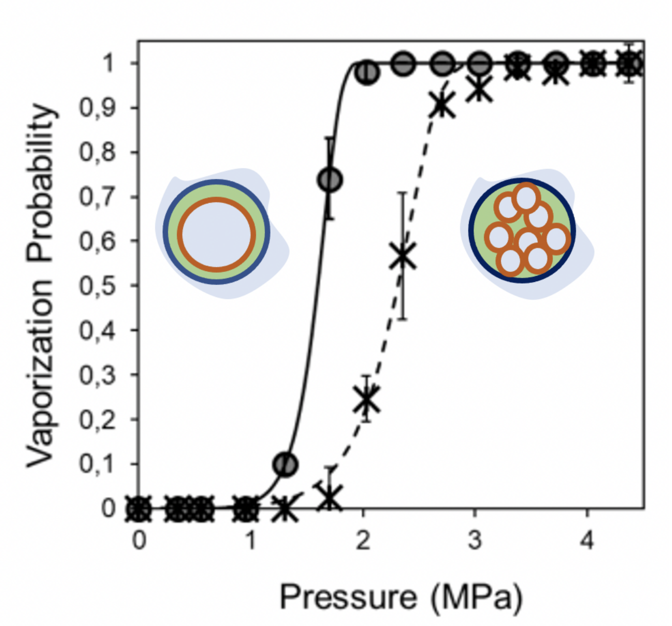

Figure 6 – Vaporization probability for water single-core (o) and multi-core (×) PFH droplets having a same radius of R = 20µm and containing the same water volume fraction (= 0.4). In the single-core emulsions (o) the internal radius of a single water drop is 14.5 µm. In multi-core emulsions (×) the water droplets have a radius of 0.22 µm.

all droplet types, and the pressure at which release begins is not significantly different.

3.3. Increasing the acoustic energy increases the release

ADV has been shown to occur during the first cycle of the first pulse of an acoustic signal, provided that the threshold pressure is achieved. Increasing the number of cycles, and thus the acoustic energy into the system (eq. 1) from 5-cycle pulses to 50-cycle pulses should not have any effect on the release, if the threshold pressure of ADV is reached.

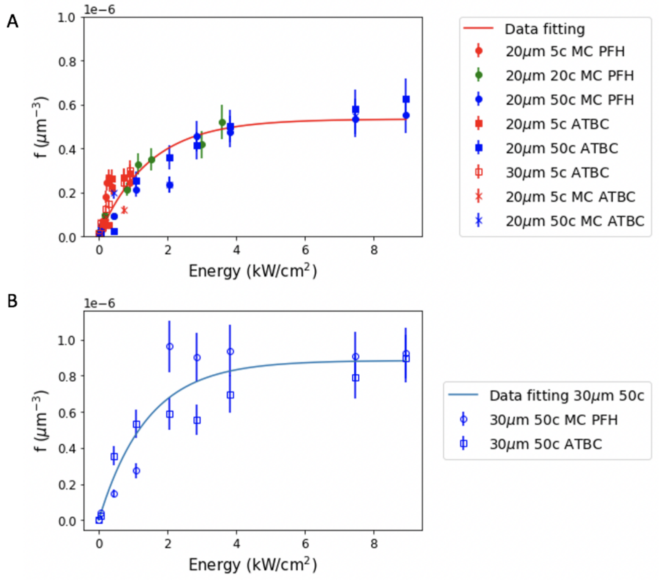

Figure 7 – A: Release of fluorescent probe from PFH and ATBC droplets. normalized by R^3 and n_f, where R is the radius and n_f is the number of droplets in the focal zone of the transducer, plotted against acoustic energy. The meaning of the symbols is summarized on the right part of the figure: The first digit specifies the radius of the droplet, the second the number of periods in the signal, MC indicates the multi-core droplets, then PFH or ATBC indicate the oil used to make the droplet. The data for the 20 µm radius droplets fitted with eq. 2 lead to $\beta = 5.33 \times 10^{-7}$ µm^{-3} ($\pm 6.05 \times 10^{-8}$) and $\alpha = 0.686$ ($\pm$ 0.006). B: Release from 30 µm multi-core PFH (MC PFH) shown as empty blue circles and plain ATBC (ATBC) droplets shown as empty blue squares, treated with 50-cycle pulses, fitted with eq. 1 with $\beta = 8.85 \times 10^{-7}$ µm^{-3} ($\pm 3.52 \times 10^{-8}$)and $\alpha = 0.71$ ($\pm$ 0.03).

The percentage of release (normalized by R^3 and n_f, with R the radius of the droplet and n the number of droplets in the focal zone) is plotted in fig. 7 as a function of the acoustic energy. We observe an increase in the release with increasing acoustic energy, thus confirming that there is no ADV. We observe that this behaviour occurs for both PFH droplets and ATBC droplets, thus suggesting the same mechanism of release.

3.4. More efficient release from single-core droplets compared to multi-core droplets

The release from single-core PFH droplets occurs more abruptly compared to multi-core droplets (comparison of data in fig. 7 and 8). Similarly to multi-core PFH droplets, about 50% of the release occurs from both 20 µm and 30 µm droplets before the ADV threshold.

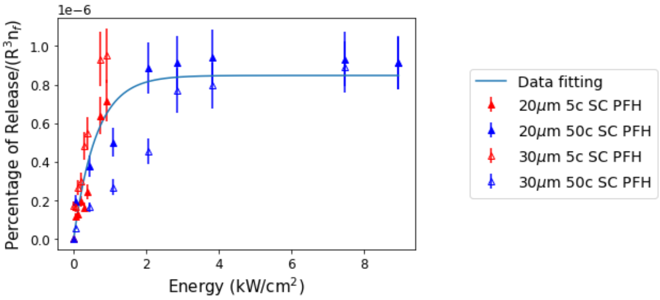

Figure 8 – Release of fluorescent probe from single-core PFH droplets, normalized by R^3 and n_f, where R is the radius and n_f is the number of droplets in the focal zone, plotted versus the acoustic energy. 20 µm radius droplets are plotted as filled triangles, 30 µm droplets are plotted as empty triangles, droplets treated with 5-cycle pulses are shown in red and droplets treated with 50-cycle pulses are shown in blue. $\beta = 8.47 \times 10^{-7}$ µm^{-3} ($\pm 5.38 \times 10^{-8}$) and $\alpha = 1.60$ ($\pm$ 0.03).

4. Discussion

Table. 1 shows that the release from ATBC and PFH droplets occurs below the ADV threshold measured for both PFH droplet types. On fig. 7 and 8, the fits of the data all give similar β values, which all correspond to the theoretical β value, thus suggesting that the release mechanism for all droplets is the same. It is well known that ATBC oil does not undergo ADV in the conditions used. The release mechanism of all droplets appears to be a diffusion, regardless of the type of oil used or core composition. On fig. 7B, in the case of 30 µm multi-core PFH and plain ATBC droplets treated with 50-cycle pulses, the release is higher than for the multi-core droplets on fig. 7A. The higher release could be explained by an inexact estimation of the number of droplets in the focal zone, n_f. It is possible that n_f, by which we normalize the percentage of release is higher than the one calculated. When calculating n_f, we assumed static conditions, therefore a constant number of droplets in the focal zone. However, the acoustic radiation force induces movement and recirculation of the droplets, which causes a higher number of droplets to arrive in the focal zone than the number calculated. This higher number of droplets would result in a collapse of the curve on fig. 7B, onto the fit curve in fig. 7A. Doing these experiments in a gel that stabilizes the droplets could confirm this hypothesis and will be the subject of future work. The α values for the release from multi-core and plain droplets (fig. 7 A and B) are comparable, but α for the release from single-core droplets is higher (fig. 8). The release is therefore more abrupt with single-core droplets. This could be explained by the smaller total surface area of the water core inside of the PFH droplet, compared to multi-core droplets. When a molecule leaves the water core, it is less likely to encounter an interface other than the outer one, whereas for multi-core droplets the multiple nanodroplets provide a large surface area that can be encountered by the molecule. This could cause the release from single-core droplets to diffuse more quickly into the bulk. Another explanation consists in a different mechanism, for both multi-core droplets and single-core droplets. It could occur through the inner droplet (or inner nanodroplets, in the case of multi-core droplets) leaving the PFH and solubilizing in the bulk. For the droplet to be destabilized, the interfacial tension has to be altered. Fig. 9 (left) shows a single-core droplet right after production, when the surfactant molecules have not yet fully assembled on the interfaces. Eventually, the inner droplet goes inside of the PFH, once the surfactants have assembled. We suggest that the ultrasound signal could induce a destabilization in the opposite way, thus causing the internal water droplet to leave the PFH. It has been shown that single-core droplets can be in dewetting conformations [34, 35], and either the internal droplet comes back into the PFC droplet, or it leaves and the content solubilizes in the bulk. Once the droplet is in a dewetting conformation (fig.9), above a certain percentage of inner droplet pushed out of the PFH droplet, the inner water droplet is destabilized into the bulk and the content is released. According to Wang et al [34], the stability of the system is achieved when:

$$\gamma_{AB} cos\theta_A + \gamma_A + \gamma_B cos(\theta_A + \theta_B) = 0 \qquad (3)$$

where γ_A is the interfacial tension between the PFH droplet and the water bulk, γ_B is the interfacial tension between the inner water droplet and the water bulk, and γ_{AB} is the interfacial tension between the inner water droplet and the PFH droplet, θ_A, θ_B and θ_{AB} are the corresponding angles shown in fig.9(left). The values of γ_A, γ_B and γ_{AB} were measured in static conditions to approximate their order of magnitude in the droplet.

The value of γ_B changes (as calculated by eq.3) according to the stage of engulfing of the core droplet, and depends on the angles, θ_A and θ_B and the other interfacial tensions. During dewetting, the F_8TAC_{13} surfactant that

Interface	Interfacial tension (mN/m)
γ_A	25
γ_B	16
γ_{AB}	18

Table 2 – Table showing the interfacial tensions measured experimentally at the interfaces of single core droplets. γ_A is the interfacial tension between the PFH droplet and the water bulk, γ_B is the interfacial tension between the inner water droplet and the water bulk, and γ_{AB} is the interfacial tension between the inner water droplet and the PFH droplet. The measurements were taken using a drop tensiometer (Teclis Scientific).

normally stabilizes the outer PFH/water interface adds onto the water/water interface that is created (fig. 9). A thin layer of PFH goes to this interface and the result is a bilayer of F_8TAC_{13} and Krytox, separated by a thin layer of PFH. When the inner water droplet moves toward the bulk, the thin layer of PFH that covers it is drained (similarly to a soap bubble). Once the inner droplet has left the PFH, it is destabilized and the content is released into the bulk. An example of changes in γ_B necessary to induce a dewetting is shown in a modelized movie in Supplementary information.

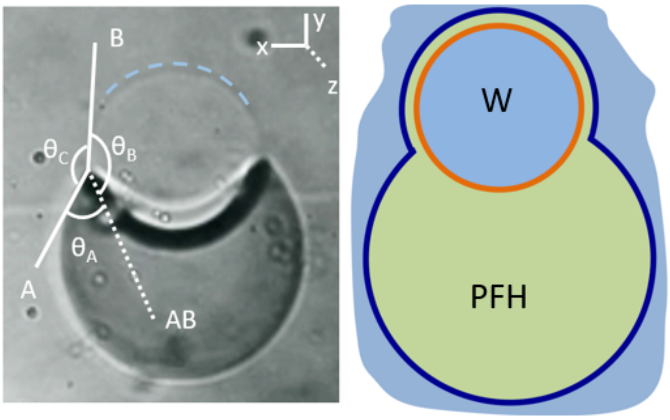

Figure 9 – Left: Image of 20 µm radius single-core PFH droplet in a microfluidic channel right after production, in a dewetting configuration. The angles and interfaces shown (in white) are used to calculate the stability of the system. The doted blue line is a guide to find the outer interface of the inner water droplet. Right: Scheme of the single-core PFH double emulsion droplet, with a layer of PFH present between the inner water phase (denoted W), and the bulk. The inner (smaller) water droplet which is in contact with the bulk is stabilized by Krytox at the interface inside the PFH droplet, and it is stabilized by a bilayer of surfactants (Krytox and F_8TAC_{13}) where it is in contact with the bulk (doted blue line on the left image, as a guide). The PFH droplet is stabilized by F_8TAC_{13}. Here, the surfactants have not yet assembled fully at the interface of the inner droplet. Once they do, the inner droplet goes inside of the PFH phase.

5. Conclusion

We studied the ultrasonic release of fluorescent molecules from droplets made of biocompatible oils. The droplets produced by microfluidics, are stabilized by surfactants and dispersed in water (fig. 1). The hydrophobic dye was sequestered in droplets of ATBC, while the hydrophilic one was either in many water nanodroplets or in one micro droplet, dispersed in the oil droplets of ATBC or PFH. A 1.1 MHz wave causes the release of the dyes at pressures significantly lower than those necessary to vaporize the droplets acoustically ($P_{ADV} \approx 2$MPa). Delivery starts at P $= 0.1 P_{ADV}$. A pressure of about 0.3 MPa releases about 30% of dye after an ultrasound exposure of only 2.3 min. We checked that the temperature increase due to the wave never exceeded 1.5 °C.

We find that a diffusive model can explain the release from all droplet types. In the case of a single droplet of water encapsulated in PFH, we also investigate another possible mechanism in which the water droplet is escaping from the droplet of oil due to the variations of the surface tensions induced by the ultrasound, whereas in the other cases it would rather be a question of the modification of the permeability of the monolayers present in the structures of droplets, and therefore here also of the indirect modification of the interfacial tensions. Despite some progress already accomplished in this area, [36, 37] we believe that the interaction between the variation of the interfacial tensions and the ultrasound signal requires a further theoretical effort.

6. Acknowledgments

We thank Dr. Jacques Fattaccioli for his precious help in setting up the microfluidic experiments and Jose Quintas for his technical support.

References

[1] K. Loskutova, D. Grishenkov, M. Ghorbani, Review on Acoustic Droplet Vaporization in Ultrasound Diagnostics and Therapeutics, BioMed Research International 2019 (2019) 1–20. `doi:10.1155/2019/9480193`.
URL `https://www.hindawi.com/journals/bmri/2019/9480193/`

[2] R. Melich, A. Zorgani, F. Padilla, C. Charcosset, Preparation of perfluorocarbon emulsions by premix membrane emulsification for Acoustic Droplet Vaporization (ADV) in biomedical applications, Biomedical Microdevices 22 (3) (2020) 62. `doi:10.1007/s10544-020-00504-5`.
URL `https://link.springer.com/10.1007/s10544-020-00504-5`

[3] M. L. Fabiilli, J. A. Lee, O. D. Kripfgans, P. L. Carson, J. B. Fowlkes, Delivery of Water-Soluble Drugs Using Acoustically Triggered Perfluorocarbon Double Emulsions, Pharmaceutical Research 27 (12) (2010) 2753–2765. `doi:10.1007/s11095-010-0277-5`.
URL `http://link.springer.com/10.1007/s11095-010-0277-5`

[4] K. Astafyeva, L. Somaglino, S. Desgranges, R. Berti, C. Patinote, D. Langevin, F. Lazeyras, R. Salomir, A. Polidori, C. Contino-Pépin, W. Urbach, N. Taulier, Perfluorocarbon nanodroplets stabilized by fluorinated surfactants: characterization and potentiality as theranostic agents, Journal of Materials Chemistry B 3 (14) (2015) 2892–2907. `doi:10.1039/C4TB01578A`.
URL `http://xlink.rsc.org/?DOI=C4TB01578A`

[5] J. Osborn, M. S. Anderson, M. Beddingfield, L. G. Zhang, K. Sarkar, Acoustic Droplet Vaporization of Perfluorocarbon Droplets in 3D-Printable Gelatin Methacrylate Scaffolds, Ultrasound in Medicine & Biology 47 (11) (2021) 3263–3274. `doi:10.1016/j.ultrasmedbio.2021.07.016`.
URL `https://linkinghub.elsevier.com/retrieve/pii/S0301562921003136`

[6] Z. Yuan, A. Demith, R. Stoffel, Z. Zhang, Y. C. Park, Light-activated doxorubicin-encapsulated perfluorocarbon nanodroplets for on-demand drug delivery in an in vitro angiogenesis model: Comparison between perfluoropentane and perfluorohexane, Colloids and Surfaces B: Biointerfaces 184 (2019) 110484. `doi:10.1016/j.colsurfb.2019.110484`.
URL `https://linkinghub.elsevier.com/retrieve/pii/S0927776519306289`

[7] G. A. Husseini, W. G. Pitt, Micelles and nanoparticles for ultrasonic drug and gene delivery, Advanced Drug Delivery Reviews 60 (10) (2008) 1137–1152. `doi:10.1016/j.addr.2008.03.008`.
URL `https://linkinghub.elsevier.com/retrieve/pii/S0169409X0800080X`

[8] R. J. Wilson, Y. Li, G. Yang, C.-X. Zhao, Nanoemulsions for drug delivery, Particuology 64 (2022) 85–97. `doi:10.1016/j.partic.2021.05.009`.
URL `https://linkinghub.elsevier.com/retrieve/pii/S1674200121001176`

[9] Y. H. Bae, K. Park, Targeted drug delivery to tumors: Myths, reality and possibility, Journal of Controlled Release 153 (3) (2011) 198–205. `doi:10.1016/j.jconrel.2011.06.001`.
URL `https://linkinghub.elsevier.com/retrieve/pii/S0168365911003877`

[10] A. Yildirim, N. T. Blum, A. P. Goodwin, Colloids, nanoparticles, and materials for imaging, delivery, ablation, and theranostics by focused ultrasound (FUS), Theranostics 9 (9) (2019) 2572–2594. `doi:10.7150/thno.32424`.
URL `http://www.thno.org/v09p2572.htm`

[11] S. Bhatia, Nanoparticles Types, Classification, Characterization, Fabrication Methods and Drug Delivery Applications, in: Natural Polymer Drug Delivery Systems, Springer International Publishing, Cham, 2016, pp. 33–93. `doi:10.1007/978-3-319-41129-3_2`.
URL `http://link.springer.com/10.1007/978-3-319-41129-3_2`

[12] D. Kalyane, N. Raval, R. Maheshwari, V. Tambe, K. Kalia, R. K. Tekade, Employment of enhanced permeability and retention effect (EPR): Nanoparticle-based precision tools for targeting of therapeutic and diagnostic agent in cancer, Materials Science and Engineering: C 98 (2019) 1252–1276. `doi:10.1016/j.msec.2019.01.066`.
URL `https://linkinghub.elsevier.com/retrieve/pii/S0928493118326304`

[13] M. A. Subhan, S. S. K. Yalamarty, N. Filipczak, F. Parveen, V. P. Torchilin, Recent Advances in Tumor Targeting via EPR Effect for Cancer Treatment, Journal of Personalized Medicine 11 (6) (2021) 571. `doi:10.3390/jpm11060571`.
URL `https://www.mdpi.com/2075-4426/11/6/571`

[14] R. Bazak, M. Houri, S. El Achy, S. Kamel, T. Refaat, Cancer active targeting by nanoparticles: a comprehensive review of literature, Journal of Cancer Research and Clinical Oncology 141 (5) (2015) 769–784. `doi:10.1007/s00432-014-1767-3`.

[15] N. Muhamad, T. Plengsuriyakarn, K. Na-Bangchang, Application of active targeting nanoparticle delivery system for chemotherapeutic drugs and traditional/herbal medicines in cancer therapy: a systematic review, International Journal of Nanomedicine Volume 13 (2018) 3921–3935. `doi:10.2147/IJN.S165210`.

[16] N. Al Rifai, S. Desgranges, D. Le Guillou-Buffello, A. Giron, W. Urbach, M. Nassereddine, J. Charara, C. Contino-Pépin, N. Taulier, Ultrasound-triggered delivery of paclitaxel encapsulated in an emulsion at low acoustic pressures, Journal of Materials Chemistry B 8 (8) (2020) 1640–1648. `doi:10.1039/C9TB02493J`.
URL `http://xlink.rsc.org/?DOI=C9TB02493J`

[17] J. VanOsdol, K. Ektate, S. Ramasamy, D. Maples, W. Collins, J. Malayer, A. Ranjan, Sequential HIFU heating and nanobubble encapsulation provide efficient drug penetration from stealth and temperature sensitive liposomes in colon cancer, Journal of Controlled Release 247 (2017) 55–63. `doi:10.1016/j.jconrel.2016.12.033`.
URL `https://linkinghub.elsevier.com/retrieve/pii/S0168365916312780`

[18] M. T. Manzari, Y. Shamay, H. Kiguchi, N. Rosen, M. Scaltriti, D. A. Heller, Targeted drug delivery strategies for precision medicines, Nature Reviews Materials 6 (4) (2021) 351–370. `doi:10.1038/s41578-020-00269-6`.
URL `http://www.nature.com/articles/s41578-020-00269-6`

[19] M. L. Adams, A. Lavasanifar, G. S. Kwon, Amphiphilic block copolymers for drug delivery, Journal of Pharmaceutical Sciences 92 (7) (2003) 1343–1355. `doi:https://doi.org/10.1002/jps.10397`.
URL `https://www.sciencedirect.com/science/article/pii/S0022354916312849`

[20] M. Yokoyama, Clinical Applications of Polymeric Micelle Carrier Systems in Chemotherapy and Image Diagnosis of Solid Tumors, Journal of Experimental & Clinical Medicine 3 (4) (2011) 151–158. `doi:10.1016/j.jecm.2011.06.002`.
URL `https://linkinghub.elsevier.com/retrieve/pii/S1878331711000878`

[21] C. J. Brambila, J. Lux, R. F. Mattrey, D. Boyd, M. A. Borden, C. de Gracia Lux, Bubble Inflation Using Phase-Change Perfluorocarbon Nanodroplets as a Strategy for Enhanced Ultrasound Imaging and Therapy, Langmuir 36 (11) (2020) 2954–2965. `doi:10.1021/acs.langmuir.9b03647`.
URL `https://pubs.acs.org/doi/10.1021/acs.langmuir.9b03647`

[22] P. G. Durham, P. A. Dayton, Applications of sub-micron low-boiling point phase change contrast agents for ultrasound imaging and therapy, Current Opinion in Colloid & Interface Science 56 (2021) 101498. `doi:10.1016/j.cocis.2021.101498`.
URL `https://linkinghub.elsevier.com/retrieve/pii/S1359029421000820`

[23] M. Gao, C. Liang, X. Song, Q. Chen, Q. Jin, C. Wang, Z. Liu, Erythrocyte-Membrane-Enveloped Perfluorocarbon as Nanoscale Artificial Red Blood Cells to Relieve Tumor Hypoxia and Enhance Cancer Radiotherapy, Adv. Mater. (2017) 7.

[24] O. Shpak, M. Verweij, H. J. Vos, N. de Jong, D. Lohse, M. Versluis, Acoustic droplet vaporization is initiated by superharmonic focusing, Proceedings of the National Academy of Sciences 111 (5) (2014) 1697–1702. `doi:10.1073/pnas.1312171111`.
URL `http://www.pnas.org/lookup/doi/10.1073/pnas.1312171111`

[25] M. Aliabouzar, O. D. Kripfgans, W. Y. Wang, B. M. Baker, J. Brian Fowlkes, M. L. Fabiilli, Stable and transient bubble formation in acoustically-responsive scaffolds by acoustic droplet vaporization: theory and application in sequential release, Ultrasonics Sonochemistry 72 (2021) 105430. `doi:10.1016/j.ultsonch.2020.105430`.
URL `https://linkinghub.elsevier.com/retrieve/pii/S135041772031734X`

[26] R. Guo, N. Xu, Y. Liu, G. Ling, J. Yu, P. Zhang, Functional ultrasound-triggered phase-shift perfluorocarbon nanodroplets for cancer therapy, Ultrasound in Medicine & Biology 47 (8) (2021) 2064–2079. `doi:10.1016/j.ultrasmedbio.2021.04.003`.
URL `https://linkinghub.elsevier.com/retrieve/pii/`

S0301562921001824

[27] M. P. Krafft, J. G. Riess, Therapeutic oxygen delivery by perfluorocarbon-based colloids, Advances in Colloid and Interface Science 294 (2021) 102407. `doi:https://doi.org/10.1016/j.cis.2021.102407`.
URL `https://www.sciencedirect.com/science/article/pii/S0001868621000488`

[28] N. Rapoport, Phase-shift, stimuli-responsive perfluorocarbon nanodroplets for drug delivery to cancer: Phase-shift perfluorocarbon nanoemulsions, Wiley Interdisciplinary Reviews: Nanomedicine and Nanobiotechnology 4 (5) (2012) 492–510. `doi:10.1002/wnan.1176`.
URL `https://onlinelibrary.wiley.com/doi/10.1002/wnan.1176`

[29] N. Bodin-Thomazo, F. Malloggi, P. Guenoun, Marker patterning: a spatially resolved method for tuning the wettability of PDMS, RSC Adv. 7 (73) (2017) 46514–46519. `doi:10.1039/C7RA05654K`.
URL `http://xlink.rsc.org/?DOI=C7RA05654K`

[30] A. G. Mailer, P. S. Clegg, P. N. Pusey, Particle sizing by dynamic light scattering: non-linear cumulant analysis, Journal of Physics: Condensed Matter 27 (14) (2015) 145102. `doi:10.1088/0953-8984/27/14/145102`.
URL `https://iopscience.iop.org/article/10.1088/0953-8984/27/14/145102`

[31] J. D. Berry, M. J. Neeson, R. R. Dagastine, D. Y. Chan, R. F. Tabor, Measurement of surface and interfacial tension using pendant drop tensiometry, Journal of Colloid and Interface Science 454 (2015) 226–237. `doi:10.1016/j.jcis.2015.05.012`.

[32] M. Aliabouzar, K. N. Kumar, K. Sarkar, Effects of droplet size and perfluorocarbon boiling point on the frequency dependence of acoustic vaporization threshold, The Journal of the Acoustical Society of America 145 (2) (2019) 1105–1116. `doi:10.1121/1.5091781`.
URL `http://asa.scitation.org/doi/10.1121/1.5091781`

[33] M. Fabiilli, K. Haworth, N. Fakhri, O. Kripfgans, P. Carson, J. Fowlkes, The role of inertial cavitation in acoustic droplet vaporization, IEEE Transactions on Ultrasonics, Ferroelectrics and Frequency Control 56 (5) (2009) 1006–1017. `doi:10.1109/TUFFC.2009.1132`.
URL `http://ieeexplore.ieee.org/document/4976285/`

[34] J. Wang, Y. Li, X. Wang, J. Wang, H. Tian, P. Zhao, Y. Tian, Y. Gu, L. Wang, C. Wang, Droplet Microfluidics for the Production of Microparticles and Nanoparticles, Micromachines 8 (1) (2017) 22. `doi:10.3390/mi8010022`.

[35] Z. Kang, P. Zhu, T. Kong, L. Wang, A Dewetting Model for Double-Emulsion Droplets (2016) 8.

[36] B. Krasovitski, V. Frenkel, S. Shoham, E. Kimmel, Intramembrane cavitation as a unifying mechanism for ultrasound-induced bioeffects, Proceedings of the National Academy of Sciences 108 (8) (2011) 3258–3263. `doi:10.1073/pnas.1015771108`.
URL `https://pnas.org/doi/full/10.1073/pnas.1015771108`

[37] F. El Hajj, P. F. J. Fuchs, W. Urbach, M. Nassereddine, S. Hamieh, N. Taulier, Molecular Study of Ultrasound-Triggered Release of Fluorescein from Liposomes, Langmuir 37 (13) (2021) 3868–3881. `doi:10.1021/acs.langmuir.0c03444`.

Supplementary Information

6.1. Matlab analysis of droplets

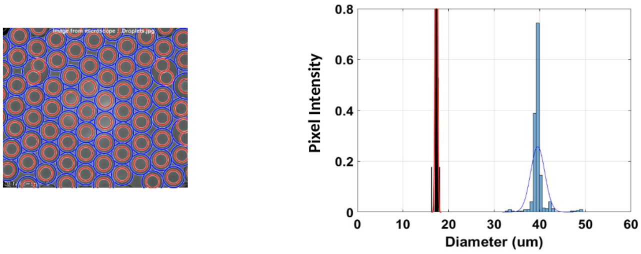

Figure S.1 – Characterization of single-core double emulsion droplets with the aqueous ratio (V_{H_2O}/V_{PFH}) = 0.6). The red circles delimit the water core and the blue circles the outer surface of the droplets. The measurements carried out on 75 droplets and fitted by a Gaussian distribution led to the following results: the droplet diameter d = 40.6 µm and the polydispersity, $PDI = (\sigma \div \mu)^2 \sim 3 \times 10^{-3}$, where σ and µ are respectively the standard deviation and the mean value. The water diameter dw = 18.2 µm and (PDI $\sim 6 \times 10^{-4}$).

6.2. ADV threshold measurement

6.3. Calculation of the equation of the fit

The amount of probe leaving the droplets and the number of probe molecules arriving in the bulk are denoted as:

$$-\frac{dN_D}{dE} = \frac{dN_B}{dE} \tag{4}$$

The release energy barrier (Eb) is reduced as the acoustic energy increases. Assuming the release is a purely diffusive process over Eb, the variation can be written:

$$\frac{dN_D}{dE} = -a(C_D - C_B) \tag{5}$$

where C_D is the concentration of probe in the droplets, and C_B is the concentration of probe in the bulk. Since $N = CV$,

$$V_D\frac{dC_D}{dE} = -a(C_D - C_B) \tag{6}$$

$$V_B\frac{dC_B}{dE} = a(C_D - C_B) \tag{7}$$

Where V_B is the volume of the bulk and V_D is the volume of all droplets in the focal zone n_f,

$$V_D = \frac{4}{3}\pi R^3 n_f \tag{8}$$

We can write

$$\frac{d(C_D - C_B)}{dE} = -a(C_D - C_B)(\frac{1}{V_D} + \frac{1}{V_B}) \tag{9}$$

We set

$$\alpha = a(\frac{1}{V_D} + \frac{1}{V_B}) \tag{10}$$

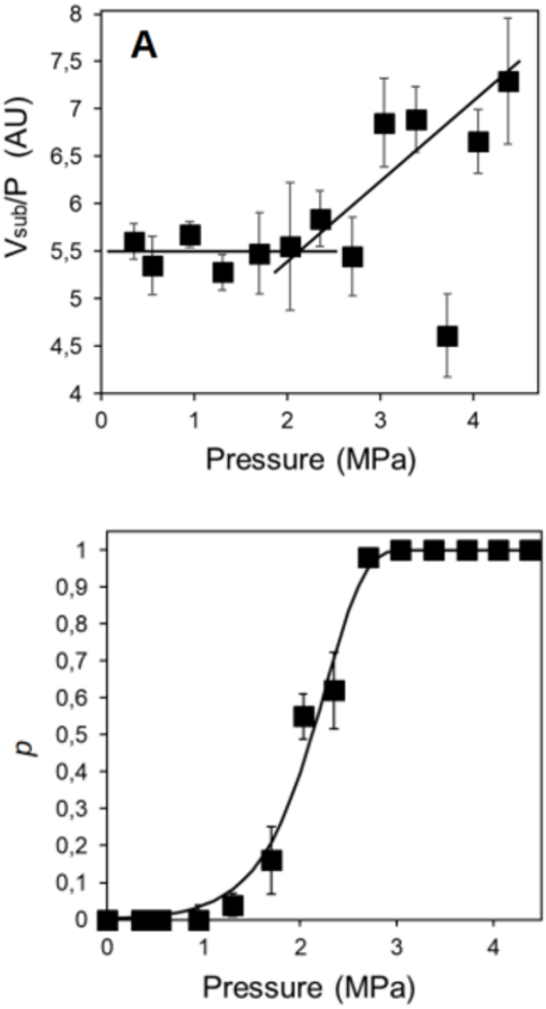

Figure S.2 – Top: Normalized sub harmonic component peak voltage amplitude of the scattered response of a suspension of PFH droplets (r = 20 µm, $\phi = 5 \times 10^{-4}$) as a function of applied acoustic pressure (MPa). The two lines intersect give P = 2.1 ± 0.3 MPa. Bottom: Probability of ADV in PFH droplets of radius of 20 µm, at a droplet volume fraction of $\phi = 5 \times 10^{-4}$, as a function of the applied acoustic pressure P. From this figure we derived that P = 2.12 ± 0.03 MPa at p = $\frac{1}{2}$, which corresponds to the ADV threshold obtained with the intersect method. The solid line being a probability fit (more details cite Article Nicolas).

So,

$$\frac{d\Delta C}{dE} = -\alpha \Delta C \tag{11}$$

$$\Delta C = \Delta C(E = 0)e^{-\alpha E} \tag{12}$$

where $C(E = 0)$ is the initial concentration, when the energy is 0. We note $C(E = 0) = C_0$. Since $N_D + N_B = N_{Total}$, which is a constant, we have

$$V_D C_D + V_B C_B = V_D C_0 \tag{13}$$

Through simplification we get

$$C_B = \frac{V_D}{V_D + V_B} C_0 (1 - e^{-\alpha E}) \tag{14}$$

V_D is negligible compared to V_B so,

$$\frac{C_B}{C_0} = \frac{\frac{4}{3}\pi R^3 n_f}{V_B}(1 - e^{-\alpha E}) \tag{15}$$

$$\frac{C_B}{C_0 R^3 n_f} = \frac{\frac{4}{3}\pi}{V_B}(1 - e^{-\alpha E}) \tag{16}$$

We set $\beta = \frac{\frac{4}{3}\pi}{V_B}$

$$\frac{C_B}{C_0 R^3 n_f} = \beta(1 - e^{-\alpha E}) \tag{17}$$

6.4. Calculation of number of droplets in acoustic beam

The acoustic beam has an ellipse shape with volume 9 mm^3, as shown in eq.18.

$$\frac{4}{3}\pi \times 4 \times 0.75^2 = 9\, mm^3 \tag{18}$$

The sample tubes used during the experiments have a conic bottom in which the droplets sediment. The height of the 5µL droplets solution in the tube is

$$h = \frac{5}{\frac{1}{3}\pi \times 5^2} = 0.19\, mm \tag{19}$$

The volume of droplets in the acoustic beam is therefore

$$V_{drops} = \frac{4}{3}\pi \times (0.19) \times (0.75)^2 = 0.4477 mm^3 \tag{20}$$

which is $4.477 \times 10^8 \mu m^3$. The volume of a 20µm radius droplet is

$$\frac{4}{3}\pi \times (20)^3 = 33510 \mu m^3 \tag{21}$$

The number of droplets in the acoustic beam is therefore 149209, as shown in eq.22.

$$\frac{4.4477 \times 10^8}{33510} = 149209 \tag{22}$$

6.5. Tables showing the pressures and flow rates for droplet production

		P (mbar)	Q (µL/min)
20µm	Φ_d	180	N/A
	Φ_c	450	8
30µm	Φ_d	150	N/A
	Φ_c	200	2.5

Table S.1 – Table showing the pressures (mbar), denoted P and flow rates (µL/min), denoted Q of the dispersed phase (denoted Φ_d) and continuous phase (denoted Φ_c) to produce 20µm and 30 µm radius plain ATBC, and multi-core PFH and ATBC droplets using the flow-focusing chip shown in fig.4 using Fluigent pressure controllers and flow unit size M. The flow rate for the dispersed phase was not recorded, since it contains either fluorescein or Nile red which tend to plug the flow units.

		P (mbar)	Q (µL/min)
20µm	Φ_{d1}	60	N/A
	Φ_{d2}	50	1.0-1.5
	Φ_c	80	2.0-2.5
30µm	Φ_{d1}	65	N/A
	Φ_{d2}	50	0.9-1.3
	Φ_c	75	2.0-2.5

Table S.2 – Table showing the pressures (mbar), denoted P and flow rates (µL/min), denoted Q of the aqueous dispersed phase (denoted Φ_{d1}), the PFH dispersed phase (denoted Φ_{d2}) and the continuous phase (denoted Φ_c) to produce 20µm and 30 µm radius single-core droplets using the flow-focusing chip shown in fig.4C using Fluigent pressure controllers and flow unit sizes S (for Φ_{d2}) and M (for Φ_c). The flow rate for the aqueous dispersed phase was not recorded, since it contains fluorescein which tends to plug the flow units.

6.6. Interfacial tension measurement of two-surfactants interface

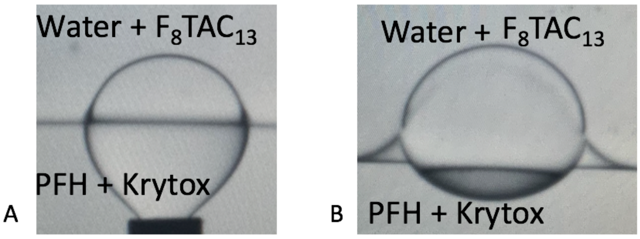

Figure S.3 – A: Microscopic image taken using Teclis tracker tensiometer of a rising water droplet produced with a curved 0.6 mm diameter needle on a Hamilton 700 series syringe. B: Droplet stabilized between PFH with Krytox phase, and water with F_8TAC_{13} phase. The interfacial tension of the top part of the droplet, that mimics the inner droplet of a single-core double emulsion droplet in dewetting conformation, was measured. The two interfaces, seen on the sides of the droplet are likely separated by a layer of PFH, which eventually thins out thus causing a destabilization of the droplet.

3.3 Bypassing alcohol evaporation in nanodroplets produced in microfluidics using the Ouzo effect

Perfluorocarbon oil nanoemulsions are used to encapsulate actives in the context of targeted drug delivery stimulated by ultrasound [88, 89, 69]. However, nanoemulsions that are made using common batch methods have high size dispersity [34]. Producing them using the Ouzo effect in a microfluidic micromixer allows for monodisperse populations of droplets [90]. A problem that can occur is that this method requires the use of an alcohol which can stay in the droplet sample post-production. Alcohol has been shown to cause leaky vasculature and affect drug delivery efficiency. A common method to remove the remaining alcohol is evaporation. In the case of perfluorocarbon oils that are commonly used in drug delivery systems, the evaporation of the alcohol cannot be achieved due to their low boiling points. Here we propose a method consisting of a centrifugation followed by a freeze-drying step to remove the alcohol from the emulsion after production, with no effect on size and improved dispersity. The combination of centrifugation and lyophilisation results in complete removal of ethanol from the droplet sample.

Bypassing alcohol evaporation in nanodroplets produced in microfluidics using the Ouzo effect

C. Thimonier[a,b,c], W.Urbach[a,b], M.Martin[a,b], S.Desgranges[d], J. Laurent[e], C. Contino-Pépin[d], C. Tribet[c], N. Taulier[a]

[a] *Sorbonne Université, CNRS, INSERM, Laboratoire d'Imagerie Biomédicale, LIB, F-75006 Paris, France*
[b] *Laboratoire de Physique de l'École Normale Supérieure, ENS, Université PSL, CNRS, Sorbonne Université, Université de Paris, F-75005 Paris, France.*
[c] *Laboratoire de Chimie de l'École Normale Supérieure, ENS, Université PSL, CNRS, Sorbonne Université, Université de Paris, F-75005 Paris, France*
[d] *Avignon Université, Équipe Systèmes Amphiphiles bioactifs et Formulations Eco-compatibles, UPRI, 84000 Avignon, France*
[e] *PMMH ESPCI Université PSL, CNRS, Sorbonne Université, Université de Paris 75005 Paris France*

Abstract

Perfluorocarbon oil nanoemulsions are used to encapsulate actives in the context of targeted drug delivery stimulated by ultrasound. However, nanoemulsions that are made using common batch methods have high size dispersity. Producing them using the Ouzo effect in a microfluidic micromixer allows for monodisperse populations of droplets, with adjustment of diameter between 200 nm and 600 nm. However, thorough removal of the solvent (alcohol) used in the method can be difficult. Minor residual quantities of alcohol in droplets has been shown to cause leaky vasculature and affect drug delivery efficiency. A common method to remove alcohol is evaporation. Due to a small difference between the boiling points of common alcohols and perfluorocarbon oils that are used in drug delivery systems, the evaporation method is unfortunately of poor efficiency. This article proposes a method consisting of a centrifugation step followed by a freeze-drying step to remove the alcohol from a perfluorocarbon:water emulsion produced via the Ouzo effect in a microfluidic micromixer. Light scattering was used to assess the absence of effect on size and dispersity. Measurements of the density of droplet dispersions enabled to determine the percentage of residual alcohol at each step of the preparation. We show that combining centrifugation and lyophilisation results in complete removal of ethanol from the droplets.

Keywords: Ouzo effect, Perfluorocarbon, Droplets, Nanoemulsion, Microfluidic

1. Introduction

Emulsions have been widely studied as a way to encapsulate active compounds, typically for drug delivery applications [1, 2, 3]. In this context, droplets made of perfluorocarbon (PFC) oil are promising candidates. When stimulated with an ultrasound trigger, PFC oils of low boiling point undergo a phase change from liquid to gas, which allows the content of the droplet to be released in a controlled manner [1, 4, 5]. In targeted therapy using ultrasound, it is desired that the pressure applied causes droplet vaporization (to release the active ingredient) but must not cause the implosion (cavitation) of the bubbles thus formed, because this leads to unwanted side effects such as bleeding. To control this phenomenon, monodisperse droplets must be used. In addition, droplets having a diameter in the range of 200 nm to 600 nm can be targeted to tumors site through the Enhanced Permeability and Retention (EPR) effect [6, 7], which is characteristic of the vasculature surrounding solid tumors. That is why the size of the emulsions is of critical importance[8, 9, 10]. Cellular processes responsible for eliminating nanoparticles such as phagocytosis and endocytosis are also sensitive to size [11]. Therefore, it is essential to control the size and dispersity of oil droplets used for targeted drug delivery. Common batch techniques such as emulsion polymerization or emulsion-solvent evaporation have the great disadvantage of producing polydisperse populations [12]. Tigher control on the size and dispersity of droplets is achieved using microfluidic devices. Microfluidics allow for the production of monodisperse droplets through the regulation of flow rates, channel dimensions, surface chemistry and production regime [12, 13]. These parameters have been optimized for micrometric droplets but making nanometric droplets remains a challenge. This is because the size of the droplets that are produced greatly depends on the size of the microfluidic motifs. Making nanometric motifs using 3D printing or photolithography requires a higher resolution than the ones commonly available. Therefore, methods have been researched to produce monodisperse nanometric droplets in microfluidic devices while skirting the issue of nanometric motif printing.

A method used to reduce the diameter of emulsion droplets is the "Ouzo" effect. It consists in nucleating oil droplets by pouring into a large volume of aqueous phase a homogeneous solution of the oil in a water-miscible solvent[14]. This method combined with mechanical mixing results in emulsions with low size dispersity [15, 16].

The combination of the "Ouzo" effect and mechanical mixing in a microfluidic device using perfluorocarbon oil has been shown by Song et al [2019] to be an effective method to produce monodisperse perfluorocarbon nanodroplets. A difference with conventional implementation of the "Ouzo" effect is that perfluorinated oils are not fully miscible with hydrogenated alcohols, but form a nanoemulsion in the alcohol phase. Song et al [2019] performed in vitro cytotoxicity assays to verify that the populations of droplets did not affect the viability of HeLa cells. The result showed no significant cytotoxicity when using a concentration of droplets of less than 3 μL/mL. However, at higher concentrations, the authors observed a decrease in cell viability. This may be due to traces of alcohol retained during the formation of drops and which could diffuse from the drops to the cells and affect their viability or functionality. Alcohol can alter cell membrane structure and protein composition, and have a fluidizing action on the membrane [17, 18]. Moreover, ethanol can cause leaky vasculature and alter the efficacy of drug delivery [19, 20]. In the case where the EPR effect is used as a tumor targeting method, this effect of alcohol on the healthy vasculature could therefore compromise the targeting by making healthy blood vessels leaky. It is therefore necessary to check the possible presence of alcohol following the production of nanodrops by the Ouzo effect and to optimize its removal.

The common method to remove the alcohol is evaporation [11, 21]. However, PFC oils conveniently used for drug delivery often have a lower boiling temperature than alcohol. Evaporation of both the oil and the alcohol is therefore inevitable. Here we propose another method based on a centrifugation step followed by lyophilisation to remove ethanol from PFC droplets. Using PFC with different boiling points, we estimated the fraction of alcohol present in droplets (by density measurements) and assessed the preservation of monodispersity (by light scattering measurements). Removal of alcohol-containing supernatant after centrifugation decreases the ethanol concentration in the droplets making it possible to implement a conventional lyophilization procedure. Lyophilization then allows for more extensive removal of both water and alcohol. We show that the dried droplets can be stored for months, then be re-suspended at the desired concentration, with only minimal change in diameter.

2. Materials and Methods

2.1. Materials

All of the solutions used inside the microfluidic devices are filtered with 0.2 µm Acrodisc Syringe Filters (Pall, France). The water used is ultra-pure water 18 MΩ (Milli-Q IQ 7000 Type-1 water Purification System). Perfluoropentane (PFP), perfluorohexane (PFH) and perfluorooctyl bromide (PFOB) were obtained from ABCR (Germany). F_8TAC_{13} is synthesized at Université d'Avignon (France). Zonyl FSO was purchased from Sigma-Aldrich. The solutions are prepared in 1.8 mL vials (VWR, France) that are compatible with the microfluidic set-up.

2.2. Surfactants

Two surfactants were used to compare the efficency of the removal of ethanol on different formulations. Zonyl FSO is a commercial fluorosurfactant and F_8TAC_{13} is a homemade fluorosurfactant.

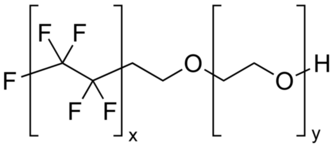

Figure 1: Chemical structure of Zonyl FSO surfactant.

F-TAC surfactants are amphiphilic molecules composed of two structural units (fig. 2). One of the units is a water-soluble oligomer of Tris(hydroxymethyl) aminomethane (Tris) units, which constitutes the polar head of the surfactant. Depending on the conditions carried out for their synthesis, it is possible to tune the average number of Tris units.

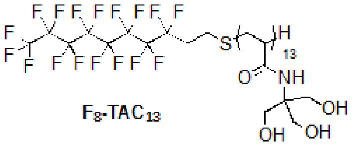

Figure 2: Chemical structure of F_8TAC_{13} surfactant.

The second unit is a fluorinated tail that acts as a fluorophilic anchorage ensuring the stabilization of the PFC droplet. The F-TAC used in the current study is made of a perfluoro-octyl tail endowed with thirteen Tris units (F_8TAC_{13}). According to the concentration of starting reactants and conditions carried out for their synthesis, it is possible to tune their final size, i.e. the average number of Tris units of the polar head also called DPn (for average degree of polymerization).

2.3. Chip Fabrication

The microfluidic circuits were designed in the lab using AutoCAD, inspired by the geometry used by Song et al [2019]. They were printed on wafers and these molds served to make the microfluidic chips (fig.3). The wafers were made using high resolution laser lithography with a two-photon polymerization printer, a Nanoscribe GT Photonic Professional device. The microfluidic chips were made using polydimethylsiloxane (PDMS) Sylgard 184, bought from Neyco, France. The PDMS gel and its curing agent were used at a ratio of 10:1 and poured onto the wafer which served as a mold for the circuit. It was degassed in vacuum then baked at 70°C for 2h. The inlets and outlets are punched with a 0.35 mm diameter biopsy puncher (World Precision Instruments, USA). The chip is cleaned with isopropanol and dried with nitrogen gas, and bonded to a glass slide. The circuit side of the chip and a microscope glass slide are both activated in an air plasma (18W for 1 min) (Harrick Scientific, NY, United States). They are then put in contact to bond, and they are placed in the oven at 70°C for 30 min. The bonded chip is activated in an air plasma for 1 min and water is inserted inside the chip to make the circuit walls hydrophilic.

2.4. Microfluidic set-up

The fluids are contained in 1.8 mL solution-filled vials screwed onto a 4-channel tube rack. The fluids are injected into the microfluidic chips with pressure controllers from Fluigent (MFCS –EZ, Le Kremlin Bicêtre, France), and the flow rates are recorded with flow units from Fluigent, sizes S (for the aqueous phase) and M (for the oil/alcohol phase). The software used to control the pressures of the fluids injected is All-in-One (AiO) (Fluigent). The experimental platform consists of an inverted microscope (Leica DM IRB). A temperature plate (PE 120 Peltier System, Linkam) is used to control the temperature of the chip to avoid evaporation of the PFC phase during production.

2.5. Droplet production

Three PFC oils were tested. PFP, which has a boiling point of 29°C, PFH which has a boiling point of 56°C and PFOB which has a boiling point of 142°C. The primary nanoemulsion was made using a volume ratio of 2:98 of PFC:ethanol respectively. The emulsion was vortexed for 5 minutes. This solution was injected into the chip through the dedicated inlet (see fig.2.3), and the aqueous phase made of water and 0.1%weight surfactant was injected into the other. The flow rates were stabilized at 8 μL/min and kept at a ratio of 1:1. The droplets were collected in a 1.8 mL vial in water and stored at 4°C before the subsequent steps.

2.6. Density measurements

The densimeter used was from Anton Paar, France. The density was measured by using 1 mL of droplet dispersion. The density of emulsions was measured at 20.000°C +/- 0.001°C.

2.7. Size measurements

The size and the polydispersity of nano size droplets were determined by dynamic light scattering using an ALV/ CGS-3 platform based goniometer system (from ALV GmbH). The measurements were performed at room temperature, and scattering angles, θ, ranging from 90° to 130°, with a step of 10°. At each angle θ, the device provided the decay rate $\Gamma_\theta = q^2(k_BT/6\pi\eta R)$; where k_B is the Boltzmann constant, T is the temperature in K, η is the viscosity of the solvent, and $q(\theta) = 4\pi n sin(\Theta/2)/\lambda$ is the magnitude of the scattering vector. The refractive index of water is n = 1.33 and λ = 633 nm is the laser wavelength and θ is the scattering angle. A fit of the curve by the cumulant method made it possible to determine the hydrodynamic droplet mean radius R along with the polydispersity index (PDI)[22, 23, 24].

2.8. Centrifugation and lyophilization

The emulsion of droplets was transferred into 2 mL centrifuge tubes to centrifuge at 6000g for 40 min at 4°C to avoid evaporation of the PFC oil. The supernatant was removed and replaced with water. Trehalose from Merck was added at a concentration of 50mg/mL to the sample to protect the droplets during lyophilization. The samples were kept at -80°C for 30 minutes, and then lyophilized at -50°C and 0.884 mbar overnight.

3. Results and Discussion

3.1. Density of the dispersion of droplet

We assessed the presence of ethanol by measurements of the density of the samples, ρ_{sol}. Without ethanol density obeys eq.1:

$$\rho_{\mathrm{sol}} = 0.98\rho_{\mathrm{aq}} + 0.02\rho_{\mathrm{pfc}} \tag{1}$$

where ρ_{aq} is the density of the water and surfactant solution, and ρ_{pfc} is the density of the PFC oil.

Densities of the produced dispersions (collected from the microfluidic device) was significantly lower than the values calculated by Eq. 1, which indicated the presence of ethanol. Centrifugation followed by lyophilisation (and reconstitution into the same final volume of water which has been adjusted by weighting samples) resulted in a density which was comparable to the calculated density of the droplet solution without ethanol. Of note, Trehalose (50 mg/mL) present at the lyophilisation step was washed out by

i) reconstitution of samples by addition of 1 mL water to lyophilisates,

ii) incubation for 30 min to sediment the droplets (followed by 30 sec centrifugation),

iii) removal of the supernatant and complementation with 1 mL of water.

The total weight of reconstituted samples (Table SI in SI) enabled to calculate the final volume fraction of PFC. The relative difference between calculated and measured densities of samples after this purification process was lower than 0.2%, suggesting a high efficiency of ethanol removal. This method was performed on PFH droplets made with our homemade surfactant F_8TAC_{13}, as well as droplets formulated with a commercial surfactant, Zonyl FSO.

The density of the sample made with PFP was lower than the calculated one. This is likely due to evaporation of the PFP that may occur even at room temperature (23 °C).

3.2. Size and stability of the droplets

The size of the droplet population was measured immediately after droplet production in the microfluidic device, after lyophilisation, and one month after production. The dried samples were kept in the fridge at 4 °C to minimize

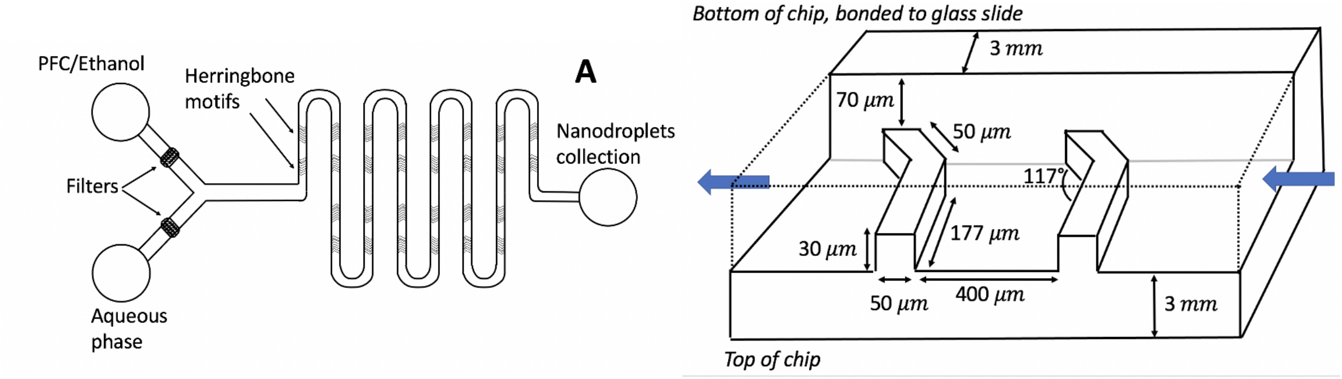

Figure 3: A: Scheme of circuit of microfluidic chip with staggerred herringbone architecture used to produce nanoemulsion with the Ouzo effect. The inlets for the oil/alcohol phase and for the aqueous phase are shown, as well as the outlet from which the nanodroplets are collected. The filters in the chip allow for the filtration of 10μm PDMS impurities, which can occur during the insertion of the microfluidic tubes. B: Scheme of herringbone architecture inside the chip.

	PFP + F_8TAC_{13}	PFH + F_8TAC_{13}	PFH + Zonyl	PFOB + F_8TAC_{13}
After production	0.966 ± 0.004	0.957 ± 0.005	0.959 ± 0.006	0.965 ± 0.005
After removal	1.008 ± 0.007	1.012 ± 0.002	1.012 ± 0.004	1.017 ± 0.009
Using eq.(1)	1.011	1.012	1.013	1.017

Table 1: Table presenting the measured and calculated densities (g/cm^3) of PFP, PFH and PFOB droplets made with F_8TAC_{13} or Zonyl as the surfactant, following production in the microfluidic device and removal of ethanol through centrifugation and lyophilization.

evaporation of PFC. The correlograms obtained at different angles were fitted by the second order cumulant, to calculate average diameters. The diameter, d, of droplets shown in Table 2 is the average at varying scattering angles with its standard error. The polydispersity index (PDI) as determined by the second order cumulant enables to calculate a standard deviation of the diameter in the population of droplets, as $\sigma = \sqrt{\text{PDI}} \times d$, where d is the average diameter of the droplets. Representative values of sigma are shown in Table. 2, which were consistent with a fairly monodisperse population. The size and polydispersity were not significantly changed after resuspension one month after lyophilisation (fig.4).

4. Conclusion

Centrifugation followed by freeze-drying remove the remaining ethanol from droplets made using the Ouzo effect. This method is particularly useful for low boiling point perfluorocarbon droplets, which are often used in targeted delivery with ultrasound [25]. The sample can be kept for months after freeze-drying, and resuspended in water at the desired concentration with only minimal change in size and dispersity. The maximum variation observed between the population of droplets before and after

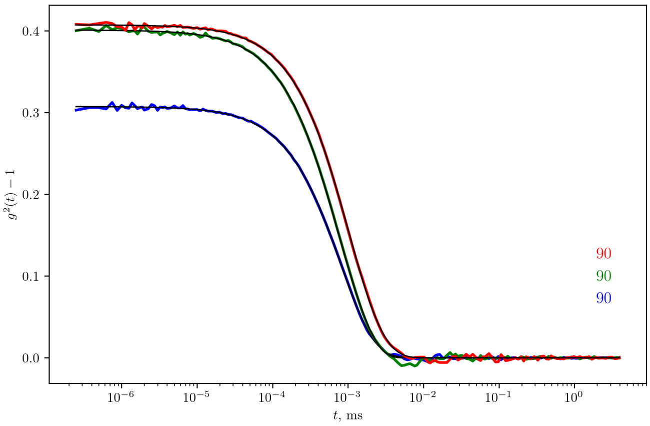

Figure 4: Cumulant curves of PFH + F_8TAC_{13} droplet dispersion taken at angle 90° showing the monodispersity right after production in the microfluidic device (blue), right after lyophilization and resuspension (green) and after one month (red).

	PFP + F_8TAC_{13}	PFH+ F_8TAC_{13}	PFH + Zonyl	PFOB + F_8TAC_{13}
After production	215.8 ± 4.9	232.6 ± 4.0	259.1 ± 4.2	322.4 ± 5.2
After removal	242.3 ± 1.9	226.4 ± 0.8	213.3 ± 4.3	343.9 ± 9.5
After one month	259.2 ± 6.5	231.8 ± 1.3	228.5 ± 4.7	324.2 ± 3.8

Table 2: Table presenting the measured diameters (nm) of PFP, PFH and PFOB droplets samples made with F_8TAC_{13} or Zonyl as the surfactant, following production in the microfluidic device and following resuspension with 1 mL of water after removal of ethanol through centrifugation and lyophilization. The size was also measured one month after lyophilisation. The PDI after removal are: ≤ 0.1

lyophilization is 45 nm change diameter and the polydispersity index is not changed. The diameter of the droplets can be varied during production by changing the flow rates and flow rate ratio as shown by Song et al [15]. The diameters of monodisperse droplets obtained range from 200 nm to 600 nm. These droplets therefore fit the size requirements for use with the EPR effect. The monodispersity of these emulsions allows for repeatable and controlled experiments. The composition of the droplets is now known, which is necessary for subsequent *in vitro* or *in vivo* experiments. The alcohol-free perfluorocarbon nanodroplets obtained could then be used for targeted drug delivery with ultrasound as the stimulus.

Conflicts of Interest

There is no conflict of interest to declare.

Acknowledgments

This work was supported by the PhD scholarship of C. Thimonier funded by ITMO Cancer - Aviesan. We thank Jacques Fattaccioli for his help with the installation of the microfluidic experiments. We thank Jose Quintas for his help with the technical support.

References

[1] R. J. Wilson, Y. Li, G. Yang, C.-X. Zhao, Nanoemulsions for drug delivery, Particuology 64 (2022) 85–97. `doi:10.1016/j.partic.2021.05.009`.

[2] D. Sheng, L. Deng, P. Li, Z. Wang, Q. Zhang, Perfluorocarbon Nanodroplets with Deep Tumor Penetration and Controlled Drug Delivery for Ultrasound/Fluorescence Imaging Guided Breast Cancer Therapy, ACS Biomaterials Science & Engineering 7 (2) (2021) 605–616. `doi:10.1021/acsbiomaterials.0c01333`.

[3] N. Rapoport, Drug-Loaded Perfluorocarbon Nanodroplets for Ultrasound-Mediated Drug Delivery, in: J.-M. Escoffre, A. Bouakaz (Eds.), Therapeutic Ultrasound, Vol. 880, Springer International Publishing, Cham, 2016, pp. 221–241, series Title: Advances in Experimental Medicine and Biology. `doi:10.1007/978-3-319-22536-4_13`.

[4] X. Dong, X. Lu, K. Kingston, E. Brewer, B. A. Juliar, O. D. Kripfgans, J. B. Fowlkes, R. T. Franceschi, A. J. Putnam, Z. Liu, M. L. Fabiilli, Controlled delivery of basic fibroblast growth factor (bFGF) using acoustic droplet vaporization stimulates endothelial network formation, Acta Biomaterialia 97 (2019) 409–419. `doi:10.1016/j.actbio.2019.08.016`.

[5] J. Osborn, M. S. Anderson, M. Beddingfield, L. G. Zhang, K. Sarkar, Acoustic Droplet Vaporization of Perfluorocarbon Droplets in 3D-Printable Gelatin Methacrylate Scaffolds, Ultrasound in Medicine & Biology 47 (11) (2021) 3263–3274. `doi:10.1016/j.ultrasmedbio.2021.07.016`.

[6] D. Kalyane, N. Raval, R. Maheshwari, V. Tambe, K. Kalia, R. K. Tekade, Employment of enhanced permeability and retention effect (EPR): Nanoparticle-based precision tools for targeting of therapeutic and diagnostic agent in cancer, Materials Science and Engineering: C 98 (2019) 1252–1276. `doi:10.1016/j.msec.2019.01.066`.

[7] A. Tahmasbi Rad, C.-W. Chen, W. Aresh, Y. Xia, P.-S. Lai, M.-P. Nieh, Combinational Effects of Active Targeting, Shape, and Enhanced Permeability and Retention for Cancer Theranostic Nanocarriers, ACS Applied Materials & Interfaces 11 (11) (2019) 10505–10519. `doi:10.1021/acsami.8b21609`.

[8] M. A. Subhan, S. S. K. Yalamarty, N. Filipczak, F. Parveen, V. P. Torchilin, Recent Advances in Tumor Targeting via EPR Effect for Cancer Treatment, Journal of Personalized Medicine 11 (6) (2021) 571.

[9] F. Yuan, M. Dellian, D. Fukumura, M. Leunig, D. A. Berk, V. P. Torchilin, R. K. Jain, Vascular Permeability in a Human Tumor Xenograft: Molecular Size Dependence and Cutoff Size, Cancer Research 55 (17) (1995) 3752–3756, publisher: American Association for Cancer Research.

[10] V. P. Torchilin, Targeted pharmaceutical nanocarriers for cancer therapy and imaging, The AAPS Journal 9 (2) (2007) E128–E147. `doi:10.1208/aapsj0902015`.

[11] E. Lepeltier, C. Bourgaux, P. Couvreur, Nanoprecipitation and the “Ouzo effect”: Application to drug delivery devices, Advanced Drug Delivery Reviews 71 (2014) 86–97. `doi:10.1016/j.addr.2013.12.009`.

[12] J. Wang, Y. Li, X. Wang, J. Wang, H. Tian, P. Zhao, Y. Tian, Y. Gu, L. Wang, C. Wang, Droplet Microfluidics for the Production of Microparticles and Nanoparticles, Micromachines 8 (1) (2017) 22. `doi:10.3390/mi8010022`.

[13] M. Joanicot, A. Ajdari, Droplet Control for Microfluidics, Science 309 (5736) (2005) 887–888. `doi:10.1126/science.1112615`.

[14] F. Ganachaud, J. L. Katz, Nanoparticles and Nanocapsules Created Using the Ouzo Effect: Spontaneous Emulsification as an Alternative to Ultrasonic and High-Shear Devices, ChemPhysChem 6 (2) (2005) 209–216. `doi:10.1002/cphc.200400527`.

[15] R. Song, C. Peng, X. Xu, R. Zou, S. Yao, Facile fabrication of uniform nanoscale perfluorocarbon droplets as ultrasound contrast agents 23 (1) (2019) 12. `doi:10.1007/s10404-018-2172-z`.

[16] X. Zhang, Z. Lu, H. Tan, L. Bao, Y. He, C. Sun, D. Lohse, Formation of surface nanodroplets under controlled flow conditions, Proceedings of the National Academy of Sciences 112 (30) (2015) 9253–9257. `doi:10.1073/pnas.1506071112`.

[17] G. Y. Sun, A. Y. Sun, Ethanol and Membrane Lipids, Alcoholism: Clinical and Experimental Research 9 (2) (1985) 164–180. `doi:10.1111/j.1530-0277.1985.tb05543.x`.

[18] E. Pilch, W. Musiał, Liposomes with an Ethanol Fraction as an Application for Drug Delivery, International Journal of Molecular Sciences 19 (12) (2018) 3806.

[19] S. Karimzadeh, B. Safaei, T.-C. Jen, Prediction effect of ethanol

molecules on doxorubicin drug delivery using single-walled carbon nanotube carrier through POPC cell membrane, Journal of Molecular Liquids 330 (2021) 115698. `doi:10.1016/j.molliq.2021.115698`.

[20] T. Hirsch, A. Koerber, F. Jacobsen, J. Dissemond, H.-U. Steinau, S. Gatermann, S. Al-Benna, M. Kesting, H.-M. Seipp, L. Steinstraesser, Evaluation of Toxic Side Effects of Clinically Used Skin Antiseptics In Vitro, Journal of Surgical Research 164 (2) (2010) 344–350. `doi:10.1016/j.jss.2009.04.029`.

[21] C. Goubault, F. Sciortino, O. Mongin, U. Jarry, M. Bostoën, H. Jakobczyk, A. Burel, S. Dutertre, M.-B. Troadec, M. L. Kahn, S. Chevance, F. Gauffre, The Ouzo effect: A tool to elaborate high-payload nanocapsules, Journal of Controlled Release 324 (2020) 430–439. `doi:10.1016/j.jconrel.2020.05.023`.

[22] A. G. Mailer, P. S. Clegg, P. N. Pusey, Particle sizing by dynamic light scattering: non-linear cumulant analysis, Journal of Physics: Condensed Matter 27 (14) (2015) 145102. `doi:10.1088/0953-8984/27/14/145102`.

[23] J. C. Brown, P. N. Pusey, R. Dietz, Photon correlation study of polydisperse samples of polystyrene in cyclohexane, The Journal of Chemical Physics 62 (3) (1975) 1136–1144. `doi:10.1063/1.430557`.

[24] D. E. Koppel, Analysis of Macromolecular Polydispersity in Intensity Correlation Spectroscopy: The Method of Cumulants, The Journal of Chemical Physics 57 (11) (1972) 4814–4820. `doi:10.1063/1.1678153`.

[25] N. Al Rifai, S. Desgranges, D. Le Guillou-Buffello, A. Giron, W. Urbach, M. Nassereddine, J. Charara, C. Contino-Pépin, N. Taulier, Ultrasound-triggered delivery of paclitaxel encapsulated in an emulsion at low acoustic pressures, Journal of Materials Chemistry B 8 (8) (2020) 1640–1648. `doi:10.1039/C9TB02493J`.

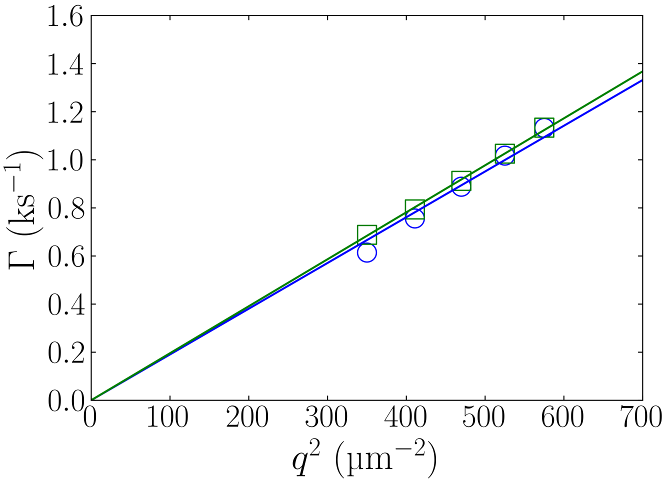

Figure 5: Graph showing the cumulative analysis of PFH droplets made with F_8TAC_{13} as the surfactant, before (blue circle) and after (green box) lyophilisation. The lines are the linear fits of the data, whose slope gives the droplet diameter.

5. Supplementary Information

	Before lyoph. (g)	After lyoph. (g)
PFH+F_8TAC_{13}	0.9566	1.0328
PFH+Zonyl	0.9583	1.0322
PFOB+F_8TAC_{13}	0.9635	1.0386
PFP+F_8TAC_{13}	0.94684	1.0256

Table S.1: Masses of droplet samples weighed right after production and right after resuspension with 1 mL of water following lyophilisation. The scale used has an uncertainty of 0.0001g.

Chapter 4

Perspectives

4.1 Reduction of size of emulsions

For the particles to be able to travel in the body without clogging the blood vessels, and to avoid uptake by the liver, the particles have to be on the order of 100's of nanometers. Therefore, the first perspective is clearly to reduce the size of the droplets, to have physiological relevance. However, the issue of encapsulation of actives remains a difficult one with PFC droplets. Since the actives cannot be dissolved in the PFC, they have to be dissolved in a water or oil core. To the best of our knowledge, monodisperse nanometric W/PFC/W or O/PFC/W droplets have not been successfully produced. Producing such systems therefore remains a challenge and an active area of research.

4.2 Photo-responsive water multi-core double emulsions as delivery vehicles

As shown in this thesis, the mechanisms of release that do not involve thermal effects are not well understood yet. The only externally stimulated drug delivery system that is currently close to clinical approval is Thermodox, and involves heat-activated lipomosomal technology. It is therefore interesting to also investigate thermal release of molecules from our droplet systems.
Light can be used as an external stimulus onto NPs for targeted drug delivery. Gold nanoparticles (AuNPs) can be used as sources of heat when triggered with light, through the thermoplasmonic effect [91, 92]. Introducing AuNPs inside of the droplet, and using light to increase the local temperature can therefore cause a phase change of a low boiling point PFC (e.g. PFP or PFH). This can cause the destabilization of the droplet, causing the release

of its content. As a preliminary proof of concept, we demonstrated that the evaporation of the PFH layer in W/PFH/W emulsions can be triggered by thermoplasmonic excitation of gold NPs (AuNPs) encapsulated in the aqueous core. These experiments were done with Lucas Sixdenier, PhD student with Emmanuelle Marie in Laboratoire P.A.S.T.E.U.R. in the Department of Chemistry at ENS. Description of materials used in these experiments can be found in Appendix section 6.1. 40 μm diameter water multi-core droplets were made using 50 nm AuNPs (NanoComposix (EconixTM, 5 mg/mL in water) in the primary nanoemulsion. The volume ratio of this W/O emulsion was 40/60 and the size of the water droplets was typically 500 nm. Aside from the addition of these AuNPs, the structure of the multi-core droplet remained the same: the water nanodroplets (containing the AuNPs) were dispersed in PFH stabilized by Krytox, surrounded by water and stabilized by F_8TAC_{13}. The multi-core configuration was preferred to a single-core double emulsion in order to maximize the contact between the volatile oil and the AuNPs-loaded water phase, and consequently the probability of oil evaporation upon light irradiation. The multi-core double emulsion was dispersed in a polymer gel solution (poloxamer 407 at 30 wt% in water) to immobilize the oil droplets and was thermalized at 30 °C. When a 532-nm laser beam (15 mW, 10-µm diameter) was focused on an individual oil droplet, a gas bubble appeared in less than 500 ms in the droplet core, suggesting that the raise of temperature induced by thermoplasmonic excitation of encapsulated AuNPs has triggered the local evaporation of the oil phase. After a few seconds of laser irradiation, the droplet was totally disrupted. This illustrative experiment is a first step towards the formation of light-responsive delivery systems based on the combination of AuNPs and liquid shells made of volatile fluorinated oils. Using a laser as targeted drug delivery stimulus is therefore promising with our double emulsion systems. Overall, there is the possibility to release either a hydrophilic or hydrophobic drug, using either ultrasound or laser as stimuli, which represents great variety and possibility for targeted drug delivery.

4.3 Delivery in a gel

To assess the delivery in static conditions, and thus be able to observe the delivery process in real time, the use of a gel as the medium for delivery is the next logical step. Similarly to the gel used in the section above, this gel could be used to trap the droplets and stop their movement, without inducing a deformation or mechanical stress which could create unwanted release. This type of experiments would also allow to confirm some hypotheses that

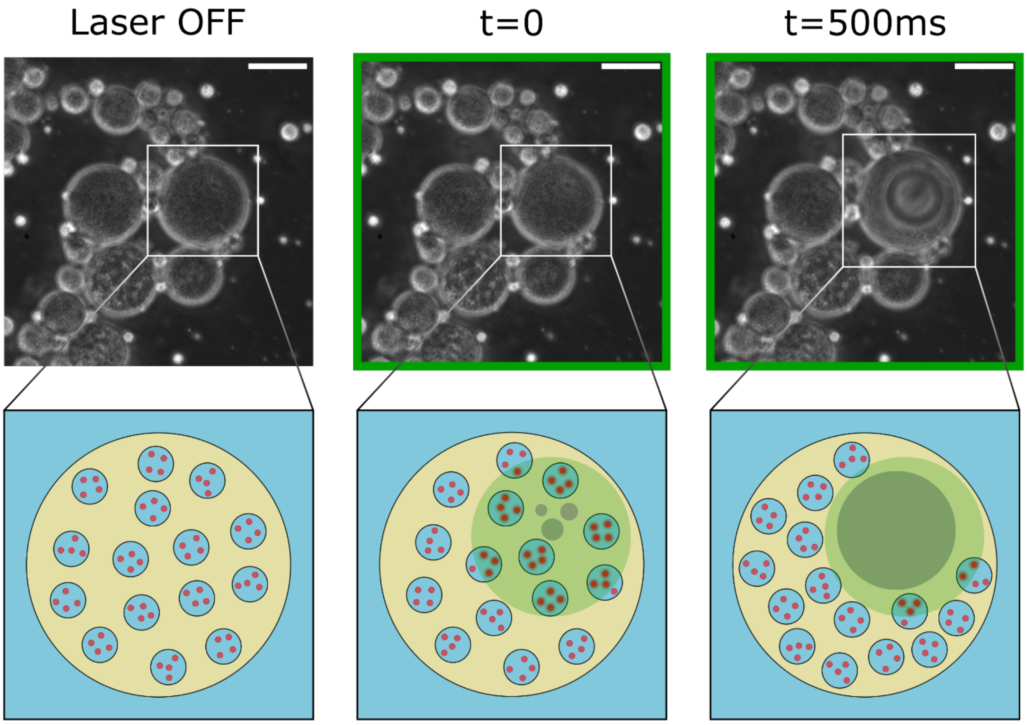

Figure 4.2.1 – *Light-triggered destabilization of a multi-core W/O/W double emulsion, consisting in AuNPs-loaded nanometric water droplets dispersed in micrometric oil droplets made of PFH. The focalization of a 532-nm laser beam (green disk) on a multi-core droplet induces a raise of temperature that locally triggers the evaporation of the oil phase. A gas bubble (grey disk) rapidly grows within the droplet, resulting in its disruption in a few seconds. Scale bar in the micrographs = 15 µm.*

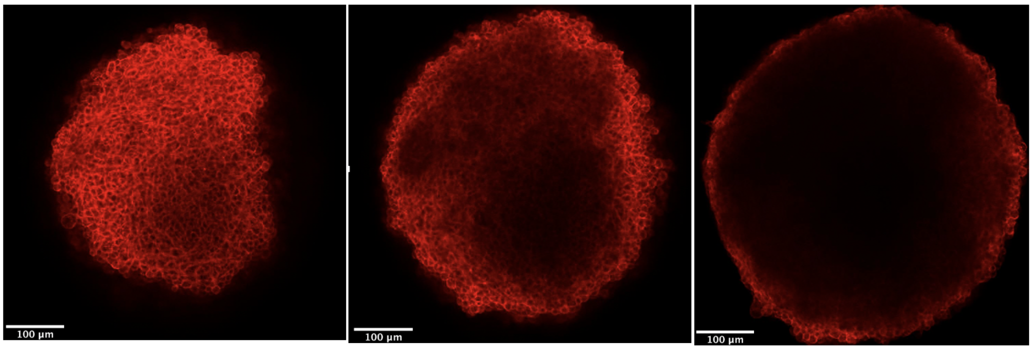

Figure 4.4.1 – *Z-stack images taken under confocal microscope, of 600 µm diameter spheroid, after staining with DAPI to stain the nucleus of cells.*

we made about the effect of the movement of droplets due to the acoustic radiation, and its effect on the delivery (in Chapter 3.2).

4.4 Delivery of actives in organ-on-chip systems

The delivery mechanisms, parameters and efficiencies shown in this thesis are well suited for biomedical applications. These vectors could be used as ultrasound- or light-responsive targeted delivery systems to carry drugs to tumors or inflammation sites to achieve spatio-temporally controlled treatment. While *in vivo* experiments are still the norm to demonstrate the possibility and efficacy of treatment, the three R's principle which emerged in the 50's calls for a more ethical use of animals through Refinement, Reduction, and Replacement of animal models [93]. In this context, synthetic alternative systems are emerging in microfluidic devices. The idea of these on-chip systems is to replicate some human physiological functions, tissues, or diseases. These systems provide more ethical, cheaper, higher throughput, more repeatable experiments and have the major advantage of allowing observation in real-time under a microscope. In such a context, I made various types of tumor spheroids, which are spherical, 3-dimensional cultures of cells (fig. 4.4.1), during my thesis (Section 6.2) and inserted them in a chip, to mimic a tumor-on-chip system. It consisted of a tumor spheroid located in the center of a microfluidic chamber (fig. 6.3.1), under perfusion of medium for 24h.

The future of this project is to move on to a chip which could reproduce a much more complex and complete system, in the form of an organ-on-chip (OOC). Such systems have been the subject of active research, and the technology and optimization have tremendously improved over the last few years. Since 2019, some groups of scientists, industrials, stakeholders and the FDA have come together to establish a standardization of the fabrication and quality of OOCs, to use them as viable alternatives for animal models [94]. This is why in the last couple of years, the industrialization of OOC's has increased and companies are commercializing them more and more (e.g. Emulate, Mimetas or Elvesys to name a few). They can reproduce a multitude of organs and tissues, such as kidney, gut, tumors, or the blood-brain-barrier. Due to these major recent advancements, the perspective in the context of our project would be to study the release in an OOC. The delivery systems used in this thesis could be used to carry a drug on an OOC, and while the viability of the organoid could be studied, the delivery mechanism could be observed in real time with the use of an ultra-fast camera. This would open new possibilities of study ranging from the actual observation of the mechanism of destabilization of the emulsions in the vicinity of biological material, to the mechanical local effects on tissue or cells, in a controlled, easily modifiable, observable and highly repeatable environment.

Chapter 5

Conclusion

The first objective of this thesis was to produce stable monodisperse emulsions for the delivery of encapsulated molecules using ultrasound. Tied to this objective was the necessity to understand the phenomenon of ADV during the vaporization of PFH single and double emulsion droplets. We produced various types of emulsion droplets:

- plain micrometric PFH droplets,
- plain nanometric PFP, PFH and PFOB droplets,
- plain micrometric ATBc droplets,
- water micrometric multi-core PFH double emulsion droplets,
- water micrometric multi-core ATBC double emulsion droplets,
- water micrometric single-core PFH double emulsion droplets,

PFCs oil were chosen because, they are biocompatible, innert, immiscible in water or other oils, and can be vaporized with ultrasound. PFH particularly has a boiling point of 56°C which makes it easier to form stable droplets in the lab at room temperature compared to lower boiling point PFC's (e.g. PFP at 29°C). The vaporization mechanism was understood in single and double PFH emulsion systems. The effect of the water core structure of the double emulsions, as well as the effect of the internal water volume fraction on the vaporization mechanism was studied. The vaporization was measured as the probability to vaporize at least 50% of the droplet sample. We showed that:

We first developed a statistical model that allows to derive the ADV pressure threshold at $p = 0.5$ for a single droplet from curves describing the probability p to observe a vaporization event in a solution of n droplets, We observed that the value of ADV pressure threshold for one droplet, $P_{0.5}^{(1)}$, decreases as the radius of the plain PFH droplets increases,

The values of $P_{0.5}^{(1)}$ can be reduced by encapsulating a micrometric water droplet inside the PFH droplets, while the encapsulation of many nanometric water droplets does not induce a modification in $P_{0.5}^{(1)}$ compared to plain droplets,

We show that this behavior is not due to superharmonic focusing or homogeneous nucleation.

The observed behavior can be explained by heterogeneous nucleation on the soft surface of emulsions. Indeed the probability to obtain a critical nucleus (i.e. a nucleus leading to vaporization with a probability $p = 0.5$) increases with an increasing concave external surface S_{ext} (*i.e.* of the droplet radius R). In the case of PFH droplets containing water, the critical nucleus can appear either on the external surface or on the internal surface (i.e. the surface of the water droplets of radius R_w). Our results suggest that the critical nucleus appears on the internal surface instead of the external one when the water droplet radius is on the micrometric size (10.5 µm).

We then performed controlled delivery experiments using the double emulsion droplets detailed above, and single emulsions of tributyl-o-acetylcitrate (ATBC) oil, stabilized by a biocompatible surfactant ($H_{12}TAC_7$). ATBC was chosen because it is biocompatible, has low water solubility, and a wide variety of hydrophobic molecules can be dissolved in it. These various types of droplets allowed us to study the controlled delivery by ultrasound of both hydrophilic (fluorescein sodium) and hydrophobic (Nile red) molecules. High frequency (1.1MHz) low pressures (0.3-2.3 MPa peak negative pressure) and short insonation time (less than 3.5 minutes) were used to deliver the probes. We showed that:

- The delivery of both probes begins well below the vaporization threshold, regardless of the diameter, structure of the core or oil composition of the droplets,

The start of release pressures are well below the ADV threshold of PFH droplets, therefore ADV is not required to release the content of all droplets used,

- Increasing the pulse length by a factor 10 increases the percentage of release, but not the release efficacy,

- We suggest that the release mechanism is a diffusion, similarly to the results obtained by Nour Al Rifai in oil nanodroplets[58].

Chapter 6

Appendices

6.1 Light-induced release materials and methods

6.1.1 Gold nanoparticles

Gold nanoparticles (AuNPs) with a diameter of 50 nm and coated with 40 kDa poly(vinyl pyrrolidone) were purchased from NanoComposix (EconixTM, 5 mg/mL in water). Prior to use, the AuNPs solution was sonicated with a Sonics Vibra-Cell VCX 750 equipped with a 3 mm microtip for 2 min at 225 W.

6.1.2 Emulsions

To facilitate their observation and laser excitation, the emulsion droplets were immobilized in a gel matrix. The double emulsion was mixed with a P407 poloxamer solution (Kolliphor©, Sigma Aldrich) at 30-40 wt% (in a 1/5 volume ratio) prior to microscope imaging.

6.1.3 Microscope imaging

Phase contrast imaging was performed with a LEICA DM IRE2 microscope equipped with a long-focal ×63 air objective. Images were acquired with a Retina 6000 Q-imaging camera and processed with Micro-Manager 1.4 software (Image J).

6.1.4 Laser excitation

The plasmonic excitation of AuNPs was achieved with a 532-nm diode laser with a nominal power of 40 mW (DJ532-40 DPSS model from Thorlabs) that was mounted on the side port of the microscope. The laser was controlled with a TED200C Thermoelectric Temperature Controller and a LDC210C Laser Diode Controller (from Thorlabs).

6.2 Tumor-on-chip

6.2.1 Spheroid production of B16F10 (Murine skin melanoma) and CT26 (Murine colon carcinoma) cells

The medium used for B16F10 cells and CT26 is Dulbecco's Modified Eagle Medium high Glucose (Merck), supplemented with 5 mL fetal calf serum and 50 mL of Amphotericin B. 4 mL of trypsin EDTA are unfrozen in the 37°C water bath for 30 minutes. Under a biological hood, 2 mL are pipetted in the cell culture box and spread all around by slowly moving the box while keeping it horizontal. The 2 mL of trypsin is taken out by removing it from the corner opposite to the surface on which the cells have adhered, and thrown away. The last 2 mL of fresh trypsin are added to the cell culture box and the box is left in the incubator (37°C and 5% CO2) for 3-5min (or until the cells have detached). 28 mL of fresh complete medium are added to a 50 mL Falcon tube. The cells with the trypsin are also added to the Falcon tube. It is centrifuged at 1000 g for 3 min. Then, the medium is taken out of the tube and the cell pellet is left at the bottom. 1mL of complete medium is added to the cells and vortexed. 90 µL of complete medium and 10 µL of the cell solution from the Falcon tube are added to a 2 mL vial. 10 µL of this solution is added onto a clean Malassez grid to count the cells. The average number of cells per square is then multiplied by 1 million to obtain the total number of cells in the 1 mL solution in the Falcon tube.

6.2.2 4T1 (Murine mammary carcinoma)

The protocol for 4T1 cells consists of the same steps as the one for B16F10 cells, except that the 2D cells medium base is Roswell Park Memorial Institute (RPMI) 1640 Glutamax (Gibco) instead of DMEM High Glucose (Gibco).

6.2.3 Spheroid medium preparation

The spheroid medium is the same as the one used for 2D culture (DMEM high glucose) but supplied with 0.25%v/v methylcellulose (Merck). For a 50 mL Falcon tube of the spheroid medium, 45.8 mL of 2D cells medium and 4.2 mL of methylcellulose are needed. Since this is a very viscous solution, it needs to be taken with a pipette tip that has been cut 5 mm from the tip, otherwise it does not get sucked in. The pipette needs to be set to a maximum of 500 µL otherwise, the methylcellulose will fill the pipette handle.

6.2.4 Spheroid formation

Each well of the plate contains 100 µL of cell solution. The target concentration therefore needs to be adjusted. To get 1000 cells per well, a concentration of 10 000 cells/mL is needed. In this case, 12 mL of medium and 40 µL of 2D cell solution (so that there is enough for clean pipetting) are needed. For 500 cells per well, 12 mL of spheroids medium and 20 µL of 2D cells solution are required. These quantities can be calculated for every cell concentration needed. The 96-well plate is then centrifuged at 600 g for 3 min and incubated at 37°C and 5% CO2 (fig. 6.2.1). For all types of cells, the mediums are changed every 72h. A 200 µL pipette is used to take out 70 µL of medium from each spheroid well. This medium is taken from the side of the well, so as to avoid disturbing the spheroid.

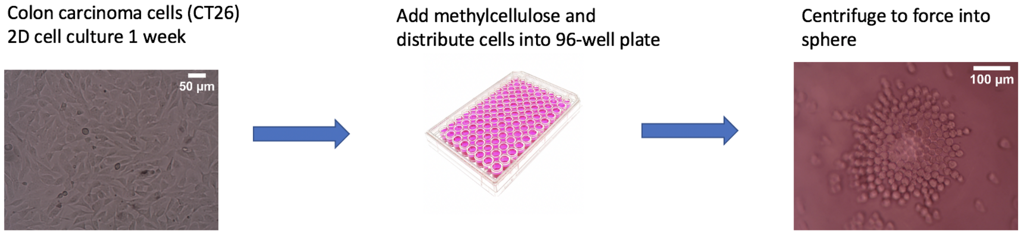
Colon carcinoma cells (CT26)
2D cell culture 1 week

Add methylcellulose and
distribute cells into 96-well plate

Centrifuge to force into
sphere

Figure 6.2.1 – *Spheroids are produced by first making a classic 2D cell culture, then taking these cells and inserting them into a 96-well plate at the desired concentration, with spheroid medium, and centrifuging to force them into a spherical conformation, before incubating them.*

6.2.5 Spheroid analysis

10 spheroids are chosen at hour 0 (right after centrifugation). The selected spheroids are at least two wells apart from each other in every direction and the ones that already have a spherical shape right after centrifugation

are prioritized. The number of the spheroid is written on the lid of the box, in the area corresponding to the well. The spheroids are imaged under the microscope every 24h with the software ToupView (fig. 6.2.5 shows a spheroid at 24h). The size is calculated using imageJ (based on the scale from a 1 mm ruler). Their circularity coefficient is measured using image J.

6.2.6 Size and cell viability analysis

Since spheroids are dense aggregates of cells, the gas exchange and nutrient supply between the core and the surrounding environment is a limiting factor above a certain size (fig. 6.2.2). According to the literature, around 70-80% of the cells in a spheroid are alive, and 20-30% are in either undergoing apoptosis (the cell programs its own death) or necrosis (death induced by external factors) [95, 96].

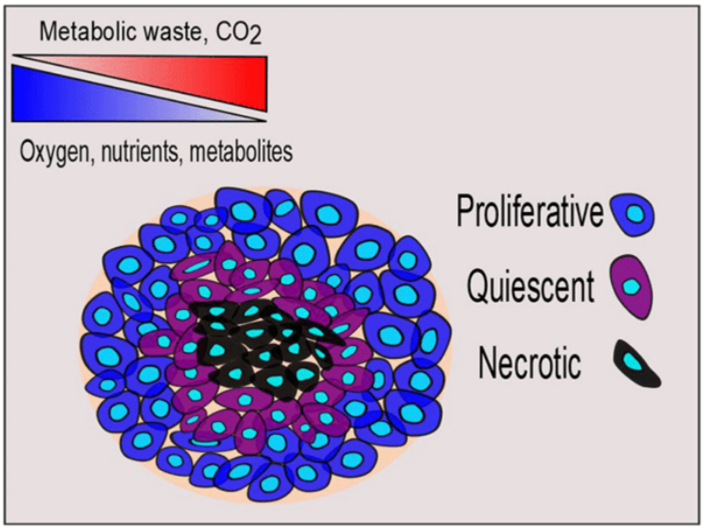

Figure 6.2.2 –
Scheme of cell viability in a spheroid. The gradients of gas and nutrients induce the necrosis of cells at the center. [97]

To compare the viability of cells composing the spheroids with that in the literature, we performed flow cytometry. Briefly, the cells are stained with a dye that marks a specific stage of viability (live, necrosed, early apoptosis etc), and the cell suspension is passed through a column, where a laser light arrives onto the cells to excite the fluorescent markers and fluorescence will be emitted from the stained cells (fig. 6.2.3). through this, we confirmed the composition of spheroids made with CT26 cells. The results show percentages of viability comparable to those in the literature (fig. 6.2.4).

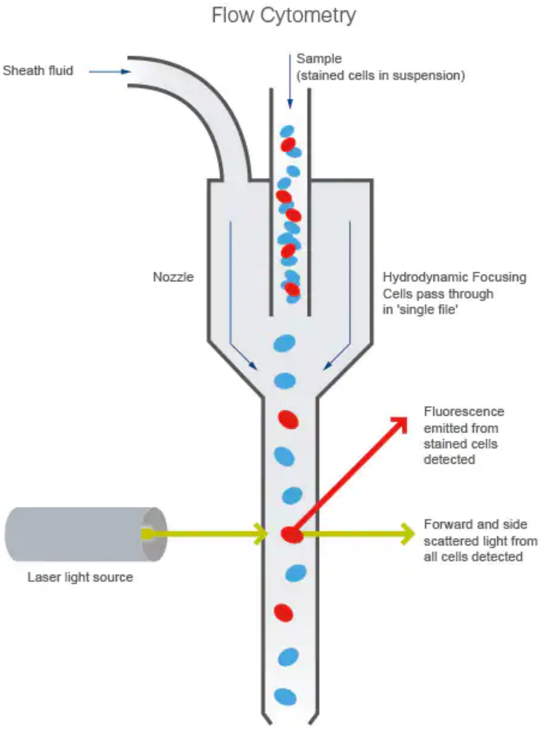

Figure 6.2.3 – Scheme of principle of flow cytometry. [2]

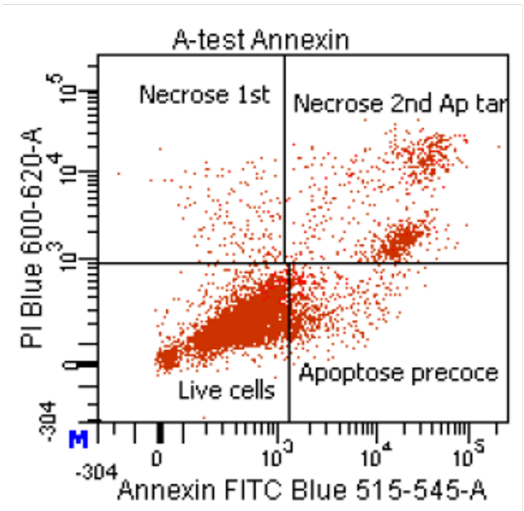

Figure 6.2.4 – *Flow cytometry analysis of spheroid cells viability. Annexin V stains for early apoptosis (bottom right quadrant), DiOC(3)6 stains for live cells (bottom left quadrant), and propidium iodide stains for necrotic cells (stages 1 and 2, in upper left and right quadrants). The results indicate that 84% of the cells are alive, 6.6% of the cells are in early apoptosis, and 9.5% of the cells are in either stage 1 or 2 of necrosis.*

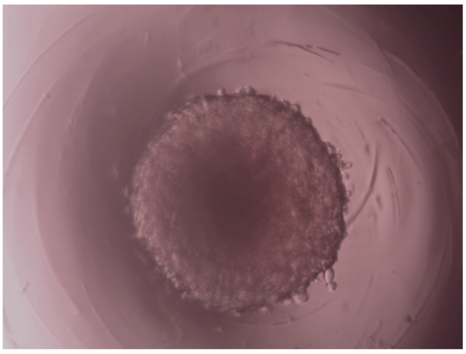

Figure 6.2.5 – [Microscopic image of 486 µm diameter spheroid at 24h after production, objective x10.

The size of spheroids seeded with varying numbers of cells was studied to assess the growth pattern depending on the initial number of cells (fig. 6.2.6). We see that the growth pattern is the same for spheroids initially seeded with 250 or 500 cells, however, there is a jump at 96h observed for spheroids seeded with 1000 cells. This could be due to the change of medium that occurs right before (at 72h), which has an effect on the next data point (96h). 1000-cells spheroids are larger so the amount of nutrients from the medium might not be enough to sustain optimal growth, and it needs to be changed more frequently to provide more nutrients.

6.3 Tumor-on-chip fabrication

The tumor-on-chip design is based on the one by [98]. It was designed with AutoCAD and printed using a Nanoscribe by Justine Laurent from PMMH Laboratory. The design consists of a top part and a bottom part (fig. 6.3.1). In the bottom part of the chip, there is a central chamber, and in the middle there is a tumor spheroid-containing compartment that is 500 μm in diameter and 500 μm deep. This central chamber is connected on one side to a channel that mimics the lymphatic vessel. The border between the chamber and the lymphatic channel is composed of 100 μm x 100 μm pillars, each separated by 100 μm. The top part of the chip consists of a channel that is perpendicular to the interstitial chamber. This mimics a capillary which would provides the nutrients. The semi circles on the sides are to insert a semi porous membrane that separates the top and the bottom part which serves to replicate the fenestrae of the vessels.

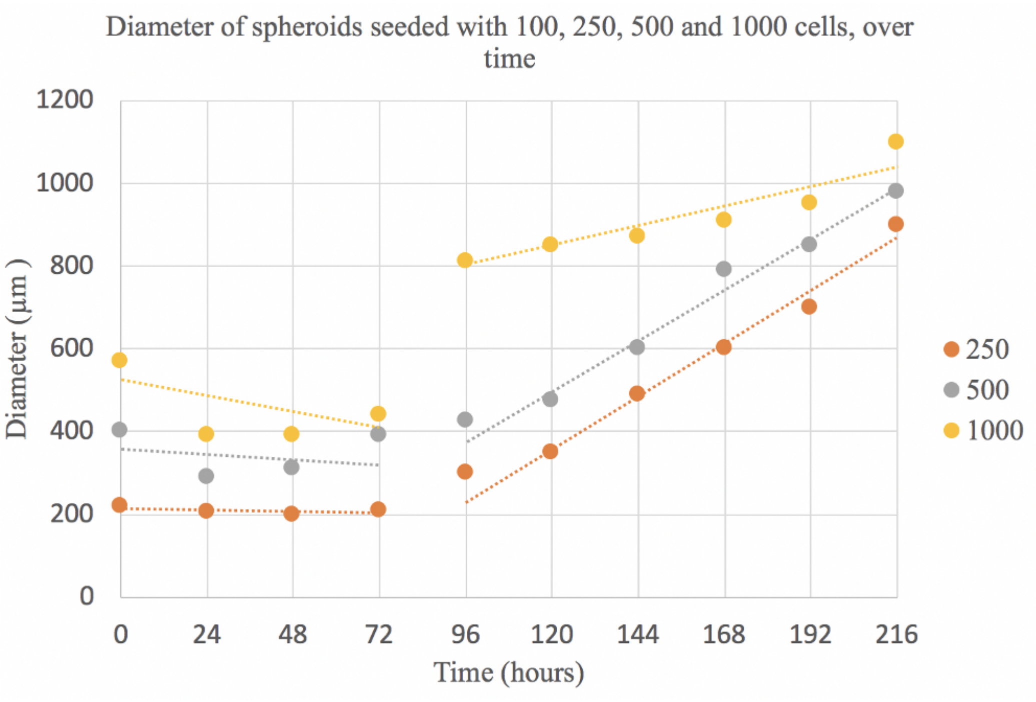

Figure 6.2.6 – Graph showing the size of spheroids seeded with 100, 250, 500 or 1000 cells, every 24h, until 216h after production.

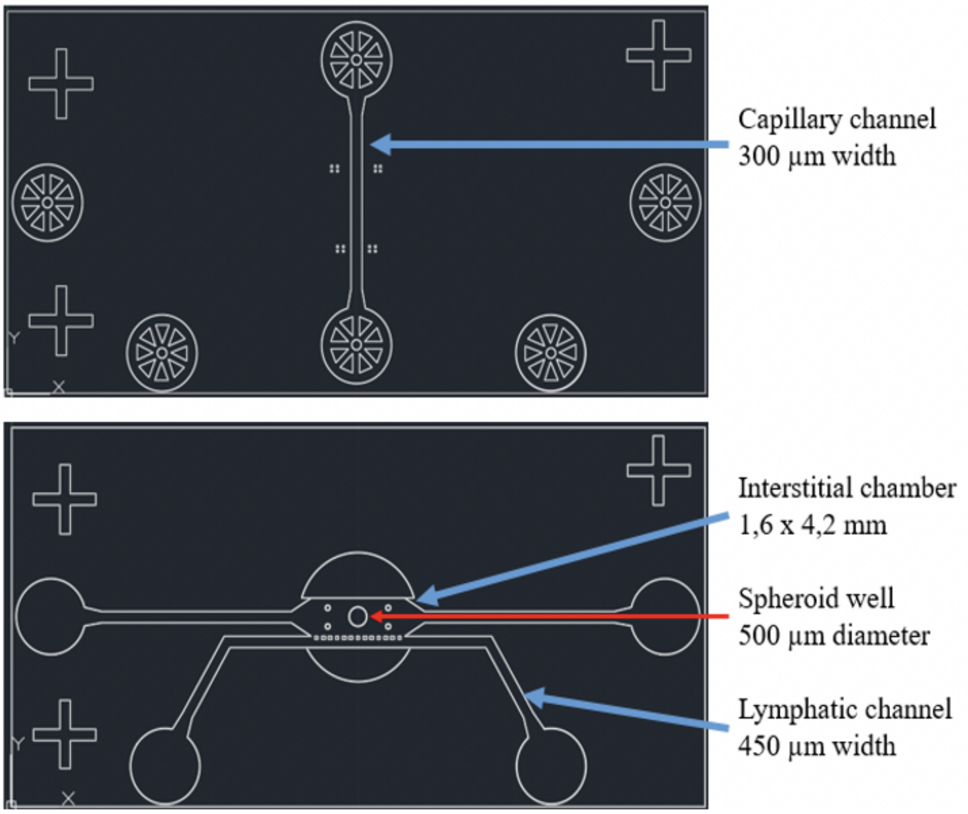

Figure 6.3.1 – *AutoCAD scheme of tumor on chip system, with top and bottom compartments.*

6.3.1 Spheroid insertion into the chip

The spheroids chosen for insertion are taken at 48h after the culture started and have to fit two criteria. Firstly, they must have a circularity coefficient above 0.5. Secondly, they must still be growing, meaning that their diameter must be increasing at 48h. These two criteria are checked using image J by measuring their size. When the spheroid that will be inserted is chosen, a 1000 µL pipette is used to take 90 µL of medium out of the well very slowly. This size of pipette tip allows the spheroid to be sucked in without damaging it. The spheroid can usually be seen in the pipette tip. Otherwise, the well is checked under the microscope to see if it is still in the well. Once the spheroid is in the pipette tip, it is removed by pushing it slowly into the outlet of the microfluidic chip. The reason to choose the outlet is because if the outlet is damaged during the insertion, it will impact the experiment less than if an inlet is damaged. The spheroid is then directed with appropriate flows inside the chip, using Fluigent pressure controllers, so that it reaches the tumor compartment, in the middle of the chip. Once the spheroid arrives in the center, the flows are stopped. A 1L lab glass bottle (with a standard thread GL-45) containing 200 mL of spheroid medium is mounted upside down on a holder, and a microfluidic tube is inserted in a hole in the waterproof lid (from Fluigent, Bottle-cap series). The end of the tube has a metallic adaptor (same as the ones used for all the other microfluidic experiments in the Materials and methods section 2), and it is plugged into the inlet of the chip. By gravity, the medium slowly perfuses the chip continuously. The outside of the chip, the tubing and the bottle are cleaned with ethanol, and the system is left in the incubator at 37°C and 5% CO2. Using this method, the spheroid keep growing inside the chip for 24h.

6.4 Résumé en Français

Un médicament administré sous une forme galénique traditionnelle se heurte à de multiples barrières physiologiques qui peuvent limiter son efficacité et même l'empêcher d'atteindre sa cible. Souvent seule une petite partie des médicaments atteint la zone malade, le reste se perd dans l'organisme. Par conséquent au lieu d'exercer sa fonction thérapeutique de manière ciblée, le médicament peut produire des effets toxiques imprévus, et une activité thérapeutique faible. Pour palier à cet état de choses et améliorer des traitements thérapeutiques une nouvelle approche consiste à développer des nano médicaments composés d'un principe actif (molécule qui va agir sur la zone malade) et d'un véhicule (ou vecteur). Son rôle est d'encapsuler et de véhiculer efficacement ce principe actif vers sa cible- un gène, une protéine, une cellule, un organe - sans endommager les cellules voisines, saines, limitant ainsi les effets secondaires néfastes. Ces systèmes permettent donc d'augmenter l'activité thérapeutique et de réduire la toxicité de nombreux médicaments, réduisant ainsi certains effets secondaires désagréables

6.4.1 Vecteurs synthétiques

Leur développement obéit à des exigences strictes concernant le matériau, sa taille, et ses propriétés. Un vecteur efficace doit

- Être biocompatible ;
- Fournir un environnement dans lequel le principe actif peut être solubilisé;
- Être invisible à l'organisme et ne pas perçu comme un corps étranger afin de pouvoir circuler suffisamment longtemps pour atteindre la zone ciblée, tout en contournant les phénomènes de résistance et les défenses ;
- Une fois sur la zone malade le mécanisme de libération doit être contrôlable spatialement et temporellement;
- Être éliminé rapidement dès que le principe actif est délivré.

Exemples de vecteurs synthétiques

Les liposomes sont des vecteurs des principes actifs les plus connus et les plus commercialisés. Le plus souvent il s'agit de gouttes aqueuses entourées d'une bicouche phospholipidique. Ils peuvent encapsuler des principes actifs hydrophobes dans leur bicouche lipidique, ou hydrophiles dans le cœur aqueux. Les principaux inconvénients des liposomes sont leur manque de stabilité et d'étanchéité par conséquent une partie du médicament est perdue avant même d'avoir atteint le site ciblé. Enfin, pour qu'ils puissent échapper au système immunitaire on décore leur surface avec des polymères tels que le que le polyéthylène glycol ce qui peut entraîner des effets indésirables Ainsi des cas de réactions allergiques ont été constatées chez des personnes ayant reçu un vaccin à base d'ARNm, et quelques rares chocs anaphylactiques. Le premier système liposomal approuvé par la FDA fut le Doxil. Il s'agit d'un agent chimio thérapeutique, doxorubicine, encapsulée dans des liposomes. Lorsqu'elle n'est pas encapsulée la doxorubicine présente une cardiotoxicité élevée, ce qui peut provoquer une cardiomyopathie. Cet effet secondaire majeur a été réduit avec le Doxil.

Les particules polymériques sont des candidates intéressantes pour l'administration des principes actifs car elles sont solubles dans l'eau, stables dans le temps et permettent le déclanchement de la libération par des stimuli tels que la chaleur ou la lumière. Leur principal inconvénient est qu'elles peuvent laisser des résidus dans le corps qui peuvent provoquer des effets indésirables (par exemple, augmenter le pH local, ou une inflammation).

Les émulsions sont des systèmes d'administration de médicaments attractifs en raison de leur polyvalence. Ces systèmes sont constitués de fluides immiscibles. L'un est dispersé dans l'autre sous forme de gouttelettes stabilisées par une monocouche des tensioactifs. Selon le fluide formant la gouttelette, un principe actif hydrophile ou hydrophobe peut y être encapsulé.

6.4.2 Emulsions perfluorocarbonées

Les huiles perfluorocarbonées (PFC) ont été étudiées comme vecteurs de médicaments. De nombreuses ont été approuvées par la FDA, donc biocompatibles. Les PFC sont des fluides clairs, ce qui permet l'observation du principe encapsulé (cellules ou médicament fluorescent par exemple). Elles sont inertes et non miscibles avec la plupart des solutions aqueuses et des huiles organiques. Une gouttelette hydrophile ou hydrophobe doit donc être ajoutée aux goutes de PFC afin d'y solubiliser les principes actifs à encapsuler. L'encapsulation des médicaments nécessite donc l'utilisation d'émulsions doubles. Les vecteurs de principes actifs (PA) hydrophiles sont constitués de gouttelette(s) d'eau dispersée(s) dans la goutte du PFC le tout dispersé dans de l'eau. Tandis que les vecteurs des PA hydrophobes sont constitués de gouttelette(s) d'huile dispersées dans du PFC le tout dispersé dans de l'eau. Incorporer un noyau d'eau ou d'huile dans les gouttelettes de PFC provoque une augmentation de leur diamètre qui atteint des dimensions micrométriques. Actuellement, le seul moyen pour transporter des actifs avec des gouttelettes nanométriques de PFC consiste à les piéger dans l'enveloppe des gouttelettes, ce qui permet d'encapsuler uniquement de très petites quantités.

6.4.3 Vaporisation acoustique des gouttes PFC

Une caractéristique particulièrement intéressante du PFC pour l'administration ciblée de médicaments est la possibilité d'induire sa vaporisation par ultrasons. Les ultrasons sont utilisés en toute sécurité dans les hôpitaux depuis des années (e.g. pour les échographies). Ce stimulus externe non invasif permet un contrôle spatial (précision millimétrique) et temporel. Le phénomène de changement de phase est appelé dans la littérature scientifique Acoustic Droplet Vaporisation ou ADV. L'ADV est utilisé pour diverses applications biomédicales telles que l'imagerie et le relargage ciblé de médicaments. Une fois que la goute enfermant le PFC transite de l'état liquide à l'état gazeux, son contenu est libéré et peut diffuser dans son environnement local. Les effets des ultrasons sur le relargage de médicaments furent classés en deux catégories principales : thermique et non-thermique. L'effet thermique implique la présence d'un matériau thermosensible qui subit un changement de conformation ou de phase et permet la libération du médicament encapsulé. Cependant, il existe certaines limites associées à l'utilisation du mécanisme thermique. La fonctionnalité des cellules est altérée à des températures supérieures à 37°C, et elles ne survivent pas audessus de 43°C. Par conséquent selon les normes de la FDA, le changement de température induit doit être inférieur à 6°C et la durée de traitement doit être la plus courte possible. L'effet athermique implique la cavitation. On appelle cavitation stable (ou non inertielle) l'oscillation du volume des bulles à la fréquence de l'onde acoustique. La cavitation stable peut être utilisée pour augmenter la pénétration d'un médicament dans les cellules en ouvrant localement la membrane cellulaire. On obtient une cavitation inertielle à des pressions acoustiques plus élevées, lorsque l'amplitude des oscillations des bulles augmente et entraîne leur l'effondrement. Cet effondrement est un processus violent qui provoque une augmentation importante de la pression et de la température, ce qui peut indure des effets délétères sur les cellules environnantes.

Le processus d'ADV et les paramètres qui l'affectent sont encore des sujets de discussion. Les principaux domaines d'étude concernent la compréhension

- de la diminution de la pression de seuil d'ADV avec l'augmentation du rayon des gouttelettes;
- de l'endroit ou la transition liquide-gaz, survient initialement.

6.4.4 Etudes et résultats

Etude I: Evidence d'une nucléation hétérogène comme mécanisme de vaporisation des gouttes PFC

Cette thèse propose une explication de ce phénomène. Nous avons étudié le seuil de pression acoustique auquel la vaporisation du perfluorohexane liquide (PFH) se produit pour trois systèmes de gouttes produits par microfluidique et donc parfaitement monodisperses :

- Gouttelettes de PFH micromértriques,
- Gouttelettes micrométriques de PFH contenant de nombreuses gouttelettes d'eau nanométriques,
- Gouttelettes micrométriques constituées d'une couronne PFH encapsulant chacune une seule goutte d'eau, micrométrique également.

La probabilité pour observer un événement de vaporisation a été mesurée en fonction de la pression provoquée par des impulsions acoustiques à une fréquence de 1,1 MHz et d'amplitude de pression inférieure à 5 MPa. Nos expériences ont été réalisées sur des solutions de gouttelettes, nous avons donc développé un modèle statistique pour extrapoler, à partir de nos courbes expérimentales, le seuil de pression ADV dans le cas où une seule goutte est insonifiée. Nous avons constaté que la valeur de ce seuil de pression ADV diminue avec l'augmentation du rayon des gouttelettes de PFH pleines. Cette valeur était réduite lorsque les gouttelettes de PFH encapsulaient une gouttelette d'eau micrométrique, tandis que l'encapsulation de nombreuses gouttelettes nanométriques d'eau n'a pas modifié ce seuil. Nous avons montré que ce comportement n'est pas dû à une focalisation subharmonique de la puissance ultrasonore par la goutte ni à une nucléation homogène. Les résultats obtenus peuvent être interprétés par une nucléation hétérogène : la bulle de vapeur apparierait sur une des nombreuses interfaces présentes dans les goutes composites. Lorsque les gouttelettes de PFH contiennent de l'eau, le noyau de nucléation conduisant à la vaporisation peut apparaître soit sur la surface interne de tensioactif entourant la goutte de PFH, soit sur la surface des gouttelettes d'eau encapsulées dans cette goute. Les résultats présentés dans cette thèse suggèrent que la vaporisation est due à un noyau de vapeur apparaissant sur la surface lorsque le rayon des gouttelettes d'eau est micrométrique, mais sur la surface externe pour les gouttelettes d'eau nanométriques. Signalons toutefois que le modèle classique de nucléation hétérogène n'est pas adapté pour prédire nos données car il est basé sur l'hypothèse que la surface, sur laquelle le noyau de vaporisation apparaît, est rigide, tandis que la surface des films entourant les gouttes étudiées est flexible.

Etude II: Relargage sans ADV, par mécanisme diffusif

Cette thèse montre ensuite que l'ADV n'est pas nécessaire pour libérer des molécules séquestrées dans des gouttelettes de PFH. Cette libération apparait pour des pressions significativement inférieures. Nous avons étudié la libération de contenu soit hydrophile soit hydrophobe à partir de trois familles de gouttelettes biocompatibles dispersées dans une solution saline. Toutes les gouttelettes ont été produites dans les dispositifs microfluidique ce qui assure leur monodispersité. Dans tous les cas, la libération des molécules séquestrées apparait à des pressions nettement inférieures à celles qui provoquent la vaporisation acoustique des gouttelettes.

- Le premier type est constitué de gouttelettes micrométriques d'huile (PFH ou citrate de tributyl-o-acétyle (ATBC) contenant des nano-gouttelettes d'eau. Un colorant fluorescent hydrophile y est solubilisé;
- Le deuxième type est constitué des gouttes de PFH contenant une seule gouttelette d'eau micrométrique solubilisant un colorant fluorescent hydrophile;
- Le troisième type consiste en des nano-gouttelettes d'ATBC contenant un colorant hydrophobe.

Nous avons constaté que l'augmentation de l'énergie acoustique incidente sur les gouttes augmente la quantité libérée, mais n'affecte pas la pression à laquelle la libération commence. La libération de marqueurs fluorescents fut modélisée par une diffusion de la goutte vers le milieu environnant du marqueur.

Etude III: Production de nanogouttes par effet Ouzo sans résidu d'alcool

La dernière partie de cette thèse décrit une méthode utilisée pour produire des nano-gouttelettes de PFC monodisperses, sans résidus d'alcool en utilisant l'effet Ouzo. Les méthodes classiques de production d'émulsions utilisent de l'énergie pour casser les gouttes afin de réduire leur taille. Les rayons obtenus avec ces méthodes sont très variables. Une méthode alternative utilisée dans cette thèse permettant de produire des nano-émulsions monodisperses est basée sur l'effet Ouzo. Il s'agit d'un mécanisme de production d'émulsion spontanée qui ne nécessite pas d'énergie ni de tensioactif pour obtenir des gouttelettes. On observe ce phénomène avec diverses boissons alcoolisées telles que l'Ouzo, le Pastis ou le Raki. Il consiste en un système ternaire constitué d'une huile (ou autre soluté), un solvant (par exemple de l'alcool) et d'eau. On forme d'abord une nanoemulsion primaire constituée d'une faible quantité d'huile dispersée dans un solvant miscible à l'eau (tel qu'un alcool). Lorsque l'eau est ajoutée au-delà d'un certain seuil à cette émulsion, les gouttelettes d'huile se séparent du solvant. Le produit final est une émulsion d'huile dans de l'eau. Les tailles obtenues varient de 100 nm à 1 µm et l'émulsion peut être stable pendant des mois. La taille et la stabilité de l'émulsion produite peuvent être modifiées en changeant les proportions et solubilités des trois composants. Leur fabrication par effet Ouzo combiné avec la microfluidique permet d'obtenir des populations monodisperses de gouttelettes, en contrôlant leur rayon selon les besoins entre 200 nm et 600 nm. Cependant, une élimination suffisante du solvant (alcool) utilisé dans la méthode peut être difficile. Or de petites quantités résiduelles d'alcool dans les gouttelettes provoquent une fluidification des membranes cellulaires et affectent ainsi l'efficacité de l'administration des médicaments. Une méthode commune pour éliminer l'alcool est l'évaporation. Mais en raison d'une petite différence entre les points d'ébullition des alcools courants et des huiles perfluorocarbonées qui sont utilisées dans les systèmes d'administration de médicaments, la méthode d'évaporation est d'une faible efficacité. Nous avons mis au point une méthode pour éliminer les traces d'alcool qui comprend une étape de centrifugation suivie d'une étape de lyophilisation.

Conclusion et perspectives

En conclusion, cette thèse est une étude des mécanismes impliqués dans la libération d'actifs hydrophiles et hydrophobes depuis des systèmes de gouttelettes d'émulsion polyvalents, pour une utilisation dans des applications biomédicales. Les travaux montrent:

- un modèle statistique qui permet de dériver la pression ADV seuil pour une seule goutte (à partir de courbes décrivant la probabilité d'observer un événement de vaporisation dans une solution d'un nombre n de gouttelettes);
- que les valeurs du seuil de pression ADV diminuent à mesure que le rayon des gouttelettes de PFH augmente;
- les valeurs de seuil ADV peuvent être réduites en encapsulant une goutte d'eau micrométrique à l'intérieur des gouttelettes PFH, tandis que

l'encapsulation de nombreuses gouttes nanométriques n'induit pas de modification par rapport aux gouttelettes simples;

- que ce comportement n'est pas dû à une focalisation superharmonique ou nucléation homogène. Le comportement observé peut s'expliquer par une nucléation hétérogène.

Nous avons ensuite montré que:

- le relargage de colorants hydrophile ou hydrophobe depuis des gouttelettes de PFH commence bien en dessous du seuil de vaporisation, quel que soit le diamètre, la structure du noyau ou la composition de l'huile des gouttelettes;
- les pressions de début de relargage sont bien inférieures au seuil ADV des gouttelettes de PFH, par conséquent l'ADV n'est pas nécessaire pour libérer le contenu de toutes les gouttelettes utilisées. Nous suggérons que le mécanisme de libération est une diffusion.

Afin de continuer l'étude du mécanisme de relargage, ces émulsions pourraient être emprisonnées dans un gel afin de limiter leur mouvement durant l'insonification et d'observer en temps réel ce mécanisme, dans un système microfluidique par exemple. Alors que les expériences in vivo sont encore la norme pour démontrer la possibilité et l'efficacité d'un traitement, le principe des trois R apparu dans les années 1950 appelle à une utilisation plus éthique des animaux. Dans ce contexte, l'alternative synthétique est un système sur puce microfluidique qui permet de reproduire certaines fonctions physiologiques humaines, saines ou pathologiques. En plus de l'aspect éthique, ces systèmes appelés organes sur puce (OOC) ont l'avantage majeur de permettre l'observation en temps réel sous un microscope. Les émulsions utilisées dans cette thèse pourraient donc transporter un médicament sur un OOC, afin d'étudier le relargage d'un principe actif au voisinage d'une tumeur ou d'un site d'inflammation. Ceci ouvrirait de nouvelles possibilités d'étude allant de l'observation proprement dite du mécanisme de déstabilisation des émulsions, aux effets mécaniques locaux sur les tissus ou les cellules, de manière contrôlée, dans un environnement facilement modifiable, observable et hautement reproductible.

Enfin, ces systèmes d'émulsions pourraient être utilisés avec d'autre stimuli que les ultrasons. Par exemple, incorporer des nanoparticules d'or dans le coeur des gouttelettes permettrait un relargage déclanché par la lumière. En effet, ce stimulus crée une augmentation de la température des nanoparticules d'or par effet thermoplasmonique, ce qui peut vaporiser le PFC, donc déstabiliser la goutte et induire un relargage du contenu. La versatilité des ces vecteurs offre donc un éventail de directions de recherches futures.

Bibliography

[1] Baghbani, F. & Moztarzadeh, F. Bypassing multidrug resistant ovarian cancer using ultrasound responsive doxorubicin/curcumin co-deliver alginate nanodroplets. *Colloids and Surfaces B: Biointerfaces* **153**, 132–140 (2017).

[2] Introduction to flow cytometry. URL `https://www.abcam.com/protocols/introduction-to-flow-cytometry`.

[3] Waks, A. G. & Winer, E. P. Breast Cancer Treatment: A Review. *JAMA* **321**, 288 (2019).

[4] Dickens, E. & Ahmed, S. Principles of cancer treatment by chemotherapy. *Surgery (Oxford)* **36**, 134–138 (2018).

[5] Bae, Y. H. & Park, K. Targeted drug delivery to tumors: Myths, reality and possibility. *Journal of Controlled Release* **153**, 198–205 (2011).

[6] Tewabe, A., Abate, A., Tamrie, M., Seyfu, A. & Abdela Siraj, E. Targeted Drug Delivery — From Magic Bullet to Nanomedicine: Principles, Challenges, and Future Perspectives. *Journal of Multidisciplinary Healthcare* **Volume 14**, 1711–1724 (2021).

[7] Shah, A., Aftab, S., Nisar, J., Ashiq, M. N. & Iftikhar, F. J. Nanocarriers for targeted drug delivery. *Journal of Drug Delivery Science and Technology* **62**, 102426 (2021).

[8] Park, H., Otte, A. & Park, K. Evolution of drug delivery systems: From 1950 to 2020 and beyond. *Journal of Controlled Release* **342**, 53–65 (2022).

[9] Greish, K., Nehoff, H., Parayath, N., Domanovitch, L. & Taurin, S. Nanomedicine for drug targeting: strategies beyond the enhanced permeability and retention effect. *International Journal of Nanomedicine* 2539 (2014).

[10] Abu-Thabit, N. Y. & Makhlouf, A. S. H. Historical development of drug delivery systems: From conventional macroscale to controlled, targeted, and responsive nanoscale systems. In *Stimuli Responsive Polymeric Nanocarriers for Drug Delivery Applications, Volume 1*, 3–41 (Elsevier, 2018).

[11] Bhatia, S. Nanoparticles Types, Classification, Characterization, Fabrication Methods and Drug Delivery Applications. In *Natural Polymer Drug Delivery Systems*, 33–93 (Springer International Publishing, Cham, 2016).

[12] Gaumet, M., Vargas, A., Gurny, R. & Delie, F. Nanoparticles for drug delivery: The need for precision in reporting particle size parameters. *European Journal of Pharmaceutics and Biopharmaceutics* **69**, 1–9 (2008).

[13] Lepeltier, E., Bourgaux, C. & Couvreur, P. Nanoprecipitation and the "Ouzo effect": Application to drug delivery devices. *Advanced Drug Delivery Reviews* **71**, 86–97 (2014).

[14] Yadav, D. & Dewangan, H. K. PEGYLATION: an important approach for novel drug delivery system. *Journal of Biomaterials Science, Polymer Edition* **32**, 266–280 (2021).

[15] Swierczewska, M., Lee, K. C. & Lee, S. What is the future of PEGylated therapies? *Expert Opinion on Emerging Drugs* **20**, 531–536 (2015).

[16] Kong, Y. W. & Dreaden, E. C. PEG: Will It Come Back to You? Polyethelyne Glycol Immunogenicity, COVID Vaccines, and the Case for New PEG Derivatives and Alternatives. *Frontiers in Bioengineering and Biotechnology* **10**, 879988 (2022).

[17] Hashimoto, Y., Uehara, Y., Abu Lila, A. S., Ishida, T. & Kiwada, H. Activation of TLR9 by incorporated pDNA within PEG-coated lipoplex enhances anti-PEG IgM production. *Gene Therapy* **21**, 593–598 (2014).

[18] Lammers, T., Kiessling, F., Hennink, W. E. & Storm, G. Drug targeting to tumors: Principles, pitfalls and (pre-) clinical progress. *Journal of Controlled Release* **161**, 175–187 (2012).

[19] Jatzkewitz, H. Über den Einbau physiologisch wirksamer Substanzen in ein kollodiales Blutplasma-Ersatzmittel. *Hoppe-Seyler´s Zeitschrift für physiologische Chemie* **297**, 149–156 (1954).

[20] Jatzkewitz, H. An ein kolloidales Blutplasma-Ersatzmittel (Polyvinylpyrrolidon) gebundenes Peptamin (Glycyl-L-leucyl-mezcalin) als neuartige Depotform für biologisch aktive primäre Amine (Mezcalin). *Zeitschrift für Naturforschung B* **10**, 27–31 (1955).

[21] Öztürk Atar, K., Eroğlu, H. & Çalış, S. Novel advances in targeted drug delivery. *Journal of Drug Targeting* **26**, 633–642 (2018).

[22] Lammari, N. *et al.* Encapsulation methods of active molecules for drug delivery. In *Drug Delivery Devices and Therapeutic Systems*, 289–306 (Elsevier, 2021).

[23] Goubault, C. *et al.* The Ouzo effect: A tool to elaborate high-payload nanocapsules. *Journal of Controlled Release* **324**, 430–439 (2020).

[24] Rideau, E., Dimova, R., Schwille, P., Wurm, F. R. & Landfester, K. Liposomes and polymersomes: a comparative review towards cell mimicking. *Chemical Society Reviews* **47**, 8572–8610 (2018).

[25] Kataoka, K. *et al.* Doxorubicin-loaded poly(ethylene glycol)–poly(b-benzyl-L- aspartate) copolymer micelles: their pharmaceutical characteristics and biological significance. *Journal of Controlled Release* 11 (2000).

[26] Lee, S.-W. *et al.* An Open-Label, Randomized, Parallel, Phase II Trial to Evaluate the Efficacy and Safety of a Cremophor-Free Polymeric Micelle Formulation of Paclitaxel as First-Line Treatment for Ovarian Cancer: A Korean Gynecologic Oncology Group Study (KGOG-3021). *Cancer Research and Treatment* **50**, 195–203 (2018).

[27] Burt, H. M. Development of copolymers of poly(DL-lactide) and methoxypolyethylene glycol as micellar carriers of paclitaxel. *Colloids and surfaces.* **16**. Place: [Amsterdam ; New York] : Publisher: Elsevier Science.

[28] Zhang, X.-y. & Zhang, P.-y. Polymersomes in Nanomedicine - A Review. *Current Nanoscience* **13**, 124–129 (2017).

[29] Mitchell, M. J. *et al.* Engineering precision nanoparticles for drug delivery. *Nature Reviews Drug Discovery* **20**, 101–124 (2021).

[30] Palmerston Mendes, L., Pan, J. & Torchilin, V. Dendrimers as Nanocarriers for Nucleic Acid and Drug Delivery in Cancer Therapy. *Molecules* **22**, 1401 (2017).

[31] Kannan, R. M., Nance, E., Kannan, S. & Tomalia, D. A. Emerging concepts in dendrimer-based nanomedicine: from design principles to clinical applications. *Journal of Internal Medicine* **276**, 579–617 (2014).

[32] Anselmo, A. C. & Mitragotri, S. Nanoparticles in the clinic: An update. *Bioengineering & Translational Medicine* **4** (2019).

[33] Yazdian Kashani, S., Afzalian, A., Shirinichi, F. & Keshavarz Moraveji, M. Microfluidics for core–shell drug carrier particles – a review. *RSC Advances* **11**, 229–249 (2021).

[34] Wilson, R. J., Li, Y., Yang, G. & Zhao, C.-X. Nanoemulsions for drug delivery. *Particuology* **64**, 85–97 (2022).

[35] Taylor, P. Ostwald ripening in emulsions 57 (1998).

[36] *An Overview of Surfactant Science and Technology*, chap. 1, 1–28 (John Wiley and Sons, Ltd, 2005). `https://onlinelibrary.wiley.com/doi/pdf/10.1002/047174607X.ch1`.

[37] Gupta, A., Eral, H. B., Hatton, T. A. & Doyle, P. S. Nanoemulsions: formation, properties and applications. *Soft Matter* **12**, 2826–2841 (2016).

[38] Botet, R. The "ouzo effect", recent developments and application to therapeutic drug carrying. *Journal of Physics: Conference Series* **352**, 012047 (2012).

[39] Vitale, S. A. & Katz, J. L. Liquid droplet dispersions formed by homogeneous liquid-liquid nucleation: The ouzo effect. *Langmuir* **19**, 4105–4110 (2003).

[40] Clausell-Tormos, J. *et al.* Droplet-Based Microfluidic Platforms for the Encapsulation and Screening of Mammalian Cells and Multicellular Organisms. *Chemistry & Biology* **15**, 427–437 (2008).

[41] Casadevall i Solvas, X. & deMello, A. Droplet microfluidics: recent developments and future applications. *Chem. Commun.* **47**, 1936–1942 (2011).

[42] Lowe, K. C., Davey, M. R. & Power, J. Perfluorochemicals: their applications and benefits to cell culture. *Trends in Biotechnology* **16**, 272–277 (1998).

[43] Dias, A., Freire, M., Coutinho, J. & Marrucho, I. Solubility of oxygen in liquid perfluorocarbons. *Fluid Phase Equilibria* **222-223**, 325–330 (2004).

[44] Kaisers, U., Kelly, K. & Busch, T. Liquid ventilation. *British Journal of Anaesthesia* **91**, 143–151 (2003).

[45] Weis, C. M., Wolfson, M. R. & Shaffer, T. H. Liquid-assisted Ventilation: Physiology and Clinica Application. *Annals of Medicine* **29**, 509–517 (1997).

[46] Nelson, D. L. Pulmonary Drug Delivery via Reverse Perfluorocarbon Emulsions: A Novel Method for Bacterial Respiratory Infections and Acute Respiratory Failure 177.

[47] Astafyeva, K. *et al.* Perfluorocarbon nanodroplets stabilized by fluorinated surfactants: characterization and potentiality as theranostic agents. *Journal of Materials Chemistry B* **3**, 2892–2907 (2015).

[48] Zarif, L., Riess, J. G., Pucci, B. & Pavia, A. A. Biocompatibility of Alkyl and Perfluoroalkyl Telomeric Surfactants Derived from Tham. *Biomaterials, Artificial Cells and Immobilization Biotechnology* **21**, 597–608 (1993).

[49] Zhong, Q. *et al.* Polymeric perfluorocarbon nanoemulsions are ultrasound-activated wireless drug infusion catheters. *Biomaterials* **206**, 73–86 (2019).

[50] Couture, O. *et al. In vivo* targeted delivery of large payloads with an ultrasound clinical scanner: Ultrasound delivery of large payload on clinical scanners. *Medical Physics* **39**, 5229–5237 (2012).

[51] Delaney, L. J., Isguven, S., Eisenbrey, J. R., Hickok, N. J. & Forsberg, F. Making waves: how ultrasound-targeted drug delivery is changing pharmaceutical approaches. *Materials Advances* 10.1039.D1MA01197A (2022).

[52] Nyborg, W. L. Biological effects of ultrasound: Development of safety guidelines. Part II: General review. *Ultrasound in Medicine & Biology* **27**, 301–333 (2001).

[53] Weinstein, J. N., Magin, R. L., Yatvin, M. B. & Zaharko, D. S. Liposomes and Local Hyperthermia: Selective Delivery of Methotrexate to Heated Tumors. *Science, New Series* **204**, 188–191 (1979).

[54] Husseini, G. A. & Pitt, W. G. Micelles and nanoparticles for ultrasonic drug and gene delivery. *Advanced Drug Delivery Reviews* **60**, 1137–1152 (2008).

[55] Peruzzi, G., Sinibaldi, G., Silvani, G., Ruocco, G. & Casciola, C. M. Perspectives on cavitation enhanced endothelial layer permeability. *Colloids and Surfaces B: Biointerfaces* **168**, 83–93 (2018).

[56] Fabiilli, M. L., Lee, J. A., Kripfgans, O. D., Carson, P. L. & Fowlkes, J. B. Delivery of Water-Soluble Drugs Using Acoustically Triggered Perfluorocarbon Double Emulsions. *Pharmaceutical Research* **27**, 2753–2765 (2010).

[57] Ahmadi, A. *et al.* Recent advances in ultrasound-triggered drug delivery through lipid-based nanomaterials. *Drug Discovery Today* **25**, 2182–2200 (2020).

[58] Al Rifai, N. *et al.* Ultrasound-triggered delivery of paclitaxel encapsulated in an emulsion at low acoustic pressures. *Journal of Materials Chemistry B* **8**, 1640–1648 (2020).

[59] Guo, R. *et al.* Functional ultrasound-triggered phase-shift perfluorocarbon nanodroplets for cancer therapy. *Ultrasound in Medicine & Biology* **47**, 2064–2079 (2021).

[60] Tremblay-Darveau, C. *et al.* 3-D Perfusion Imaging Using Principal Curvature Detection Rendering. *IEEE Transactions on Ultrasonics, Ferroelectrics, and Frequency Control* **65**, 2286–2295 (2018).

[61] Rojas, J. D. & Dayton, P. A. Vaporization Detection Imaging: A Technique for Imaging Low-Boiling-Point Phase-Change Contrast Agents with a High Depth of Penetration and Contrast-to-Tissue Ratio. *Ultrasound in Medicine & Biology* **45**, 192–207 (2019).

[62] Lin, S. *et al.* Optically and acoustically triggerable sub-micron phase-change contrast agents for enhanced photoacoustic and ultrasound imaging. *Photoacoustics* **6**, 26–36 (2017).

[63] Ho, Y.-J. & Yeh, C.-K. Concurrent anti-vascular therapy and chemotherapy in solid tumors using drug-loaded acoustic nanodroplet vaporization. *Acta Biomaterialia* **49**, 472–485 (2017).

[64] Melich, R., Zorgani, A., Padilla, F. & Charcosset, C. Preparation of perfluorocarbon emulsions by premix membrane emulsification for Acoustic

Droplet Vaporization (ADV) in biomedical applications. *Biomedical Microdevices* **22**, 62 (2020).

[65] Shpak, O. *et al.* Acoustic droplet vaporization is initiated by superharmonic focusing. *Proceedings of the National Academy of Sciences* **111**, 1697–1702 (2014).

[66] Li, D. S., Kripfgans, O. D., Fabiilli, M. L., Brian Fowlkes, J. & Bull, J. L. Initial nucleation site formation due to acoustic droplet vaporization. *Applied Physics Letters* **104**, 063703 (2014).

[67] Kripfgans, O. D., Fabiilli, M. L., Carson, P. L. & Fowlkes, J. B. On the acoustic vaporization of micrometer-sized droplets. *The Journal of the Acoustical Society of America* **116**, 272–281 (2004).

[68] Frost, D. L. Initiation of explosive boiling of a droplet with a shock wave. *Experiments in Fluids* **8**, 121–128 (1989).

[69] Loskutova, K., Grishenkov, D. & Ghorbani, M. Review on Acoustic Droplet Vaporization in Ultrasound Diagnostics and Therapeutics. *BioMed Research International* **2019**, 1–20 (2019).

[70] Boissenot, T. Ultrasound-triggered drug delivery for cancer treatment using drug delivery systems: From theoretical considerations to practical applications 64.

[71] Olvera, D. & Monaghan, M. G. Electroactive material-based biosensors for detection and drug delivery. *Advanced Drug Delivery Reviews* **170**, 396–424 (2021).

[72] Apfel, R. E. & Holland, C. K. Gauging the likelihood of cavitation from short-pulse, low-duty cycle diagnostic ultrasound. *Ultrasound in Medicine & Biology* **17**, 179–185 (1991).

[73] Szymczyk, K. Behaviour of the fluorocarbon surfactants in the monolayer at the water–air interface and in the bulk phase. *Journal of Fluorine Chemistry* **150**, 109–116 (2013).

[74] Yobas, L., Martens, S., Ong, W.-L. & Ranganathan, N. High-performance flow-focusing geometry for spontaneous generation of monodispersed droplets. *Lab on a Chip* **6**, 1073 (2006).

[75] Anna, S. L., Bontoux, N. & Stone, H. A. Formation of dispersions using “flow focusing” in microchannels. *Applied Physics Letters* **82**, 364–366 (2003).

[76] Mfcs series, microfluidic flow control system. URL `https://www.fluigent.com/research/instruments/pressure-flow-controllers/mfcs-series/`.

[77] Xiong, L., Chen, P. & Zhou, Q. Adhesion promotion between PDMS and glass by oxygen plasma pre-treatment. *Journal of Adhesion Science and Technology* **28**, 1046–1054 (2014).

[78] Bodin-Thomazo, N., Malloggi, F. & Guenoun, P. Marker patterning: a spatially resolved method for tuning the wettability of PDMS. *RSC Adv.* **7**, 46514–46519 (2017).

[79] Nunes, J. K., Tsai, S. S. H., Wan, J. & Stone, H. A. Dripping and jetting in microfluidic multiphase flows applied to particle and fibre synthesis. *Journal of Physics D: Applied Physics* **46**, 114002 (2013).

[80] Baroud, C. N., Gallaire, F. & Dangla, R. Dynamics of microfluidic droplets. *Lab on a Chip* **10**, 2032 (2010).

[81] Song, R., Peng, C., Xu, X., Zou, R. & Yao, S. Facile fabrication of uniform nanoscale perfluorocarbon droplets as ultrasound contrast agents **23**, 12.

[82] Mailer, A. G., Clegg, P. S. & Pusey, P. N. Particle sizing by dynamic light scattering: non-linear cumulant analysis. *Journal of Physics: Condensed Matter* **27**, 145102 (2015).

[83] Brown, J. C., Pusey, P. N. & Dietz, R. Photon correlation study of polydisperse samples of polystyrene in cyclohexane. *The Journal of Chemical Physics* **62**, 1136–1144 (1975).

[84] Koppel, D. E. Analysis of Macromolecular Polydispersity in Intensity Correlation Spectroscopy: The Method of Cumulants. *The Journal of Chemical Physics* **57**, 4814–4820 (1972).

[85] Morris, P., Hurrell, A., Shaw, A., Zhang, E. & Beard, P. A Fabry–Pérot fiber-optic ultrasonic hydrophone for the simultaneous measurement of temperature and acoustic pressure. *The Journal of the Acoustical Society of America* **125**, 3611–3622 (2009).

[86] Beard, P., Hurrell, A. & Mills, T. Characterization of a polymer film optical fiber hydrophone for use in the range 1 to 20 MHz: A comparison with PVDF needle and membrane hydrophones. *IEEE Transactions on Ultrasonics, Ferroelectrics and Frequency Control* **47**, 256–264 (2000).

[87] Meltzer, R. S. Food and Drug Administration ultrasound device regulation: The output display standard, the "mechanical index," and ultrasound safety. *Journal of the American Society of Echocardiography* **9**, 216–220 (1996).

[88] Durham, P. G. & Dayton, P. A. Applications of sub-micron low-boiling point phase change contrast agents for ultrasound imaging and therapy. *Current Opinion in Colloid & Interface Science* **56**, 101498 (2021).

[89] Lea-Banks, H. & Hynynen, K. Sub-millimetre precision of drug delivery in the brain from ultrasound-triggered nanodroplets. *Journal of Controlled Release* **338**, 731–741 (2021).

[90] Song, R., Peng, C., Xu, X., Zou, R. & Yao, S. Facile fabrication of uniform nanoscale perfluorocarbon droplets as ultrasound contrast agents **23**, 12 (2019).

[91] Baffou, G., Cichos, F. & Quidant, R. Applications and challenges of thermoplasmonics. *Nature Materials* **19**, 946–958 (2020).

[92] Mancini, A. *et al.* Thermoplasmonic Effect of Surface-Enhanced Infrared Absorption in Vertical Nanoantenna Arrays. *The Journal of Physical Chemistry C* **122**, 13072–13081 (2018).

[93] Crespi-Abril, A.-C. & Rubilar, T. Moving forward in the ethical consideration of invertebrates in experimentation: Beyond the Three R's Principle. *Revista de Biología Tropical* **69**, S346–S357 (2021).

[94] Piergiovanni, M., Leite, S. B., Corvi, R. & Whelan, M. Standardisation needs for organ on chip devices. *Lab on a Chip* **21**, 2857–2868 (2021).

[95] Anada, T., Fukuda, J., Sai, Y. & Suzuki, O. An oxygen-permeable spheroid culture system for the prevention of central hypoxia and necrosis of spheroids. *Biomaterials* **33**, 8430–8441 (2012).

[96] Barisam, M., Saidi, M., Kashaninejad, N. & Nguyen, N.-T. Prediction of Necrotic Core and Hypoxic Zone of Multicellular Spheroids in a Microbioreactor with a U-Shaped Barrier. *Micromachines* **9**, 94 (2018).

[97] Acland, M. *et al.* Mass Spectrometry Analyses of Multicellular Tumor Spheroids. *PROTEOMICS - Clinical Applications* **12**, 1700124 (2018).

[98] Kwak, B., Ozcelikkale, A., Shin, C. S., Park, K. & Han, B. Simulation of complex transport of nanoparticles around a tumor using tumor-microenvironment-on-chip. *Journal of Controlled Release* **194**, 157–167 (2014).